IOWA STATE UNIVERSITY
Digital Repository

1971

An optical mixing spectroscopic study of interfacial fluctuations

Frederick John Dechow
Iowa State University

Recommended Citation

www.manaraa.com

72-5193

DECHOW, Frederick John, 1945-
 AN OPTICAL MIXING SPECTROSCOPIC STUDY OF
 INTERFACIAL FLUCTUATIONS.

 Iowa State University, Ph.D., 1971
 Chemistry, physical

University Microfilms, A XEROX Company, Ann Arbor, Michigan

An optical mixing spectroscopic study

of interfacial fluctuations

by

Frederick John Dechow

A Dissertation Submitted to the

Graduate Faculty in Partial Fulfillment of

The Requirements for the Degree of

DOCTOR OF PHILOSOPHY

Major Subject: Physical Chemistry

Approved:

Signature was redacted for privacy.

In Charge of Major Work

Signature was redacted for privacy.

For the Major Department

Signature was redacted for privacy.

For the Graduate College

Iowa State University
Ames, Iowa

1971

PLEASE NOTE:

Some Pages have indistinct
print. Filmed as received.

TABLE OF CONTENTS

DEDICATION

In the name of the best that is in me, in recognition on the best in them, I dedicate this thesis to my work and to a special woman. I love them both very much.

1

INTRODUCTION

"... omne oleo tranquilari, et ob id urinantes ore spargere

quoniam mitiget naturam asperam lucemque deportet"(1).

With these words Pliny the Elder made the first record of the

wave damping properties of oil spread on water. No attempt to quantify

this phenomenon was recorded until Benjamin Franklin (2), who reached

the conclusion that the oil mainly affected the damping of waves with

small wavelength.

Lord Kelvin (3) showed that the properties of small surface waves

(capillary waves or ripples) are determined primarily by the surface

tension, in contrast to long waves where gravity is the main force

returning the surface to its equilibrium position.

Levich (4, 5) was the first to develop the theory of capillary

ripples relating the wavelength and damping characteristics in terms of

fundamental surface properties. Whereas Levich formulated the

boundary conditions on thermodynamic considerations, Wieghardt (6) and

Dorrestein (7) based their solution to this problem on hydrodynamic

boundary conditions. Goodrich (8, 9) studied the problem using a four

parameter model to describe interfacial effects. Mann (10) and Hansen

and Mann (11) studied the dependence of the velocity of propagation of

ripples on film or medium viscoelastic properties. They thought of the

surface tension γ as a function of the local surface concentration Γ of

surfactant as well as the time rate of change of Γ at a particular point

on the interface. They used this expression for the surface to write a model for interfacial effects containing a surface viscosity and a surface elastic coefficient. Van den Tempel and van de Riet (12) followed with a theoretical presentation which included a discussion of the problems associated with linearization and an approach to extension of the theory to non-linear terms.

The experimental confirmation of this Levich-type of theoretical approach was made available by the electromechanical technique developed by Mann and Hansen (13). The results of Mann and Hansen (14), Lucassen and Hansen (15) and Bendure and Hansen (16) clearly indicate that such theories are conceptually sound and that they may be used in conjunction with ripple experiments at small but still practicable wavelengths to provide accurate quantitative surface chemical information. This experimental method has been further improved by Mann and Ahmad (17). However, this method is still limited by the response of the receiving probe to frequencies below 1000 Hz. To obtain information at higher frequencies another detection system had to be developed.

This thesis proposes the use of an optical beat spectroscopic technique to examine at higher frequencies the viscoelastic properties of interfaces.

This technique is an outgrowth of the difficulty in realizing the required sensitivity for optically measuring density fluctuations in mediums. Einstein (18) noted that if one allows monochromatic light of

wave vector $\underline{k}_0$ to be incident on a transparent medium and observes the

scattering in a direction specified by $\underline{k}_s$, the wave vector of the scattered

light, then the fluctuations responsible for this scattering have a wave

vector $\underline{k}_r$ given by

$$\underline{k}_r = \underline{k}_s - \underline{k}_0 ,$$

which is essentially a Bragg "reflection."

Brillouin (19) and Mandel'shtam (20) used the dispersion relation-

ship, the relationship between the wave vector $\underline{k}_r$ and the wave frequency

ω_r' , for sound waves in order to obtain the spectrum of the scattered

light, that is, the time dependence of the sound waves. Thus in addition

to producing a Bragg reflection, the sound wave "diffraction grating"

also causes a Doppler shift because of its motion. If monochromatic

light of frequency ω_0 passes through a continuous medium, then the

light scattered at an angle θ from the incident direction consists of two

lines (the Brillouin peaks) split symmetrically above and below ω_0 by an

amount

$$\omega_r' = 2\omega_0 \left(\frac{v_s}{c_m}\right) \sin \left(\frac{\theta}{2}\right) ,$$

where v_s is the phase velocity of the sound in the scattering medium and

c_m is the velocity of light in the scattering medium.

The frequency shift can be seen to be proportional to (v_s/c_m)

which is of the order 10^{-5}. This factor makes extremely high resolu-

tion a prerequisite for observation of this effect. Despite this

condition, Gross (21) reported experimental results which verified the

angular dependence of the splitting and its variation with the frequency

of the incident light.

Leontovich (22) pointed out that if the sound waves obey the

Navier-Stokes equation, then they are damped and the Brillouin peaks

must be broadened by an amount depending on the attenuation of the

scattered phonons. However, at that time the magnitude of the

attenuation could only be approximated by extrapolation of low frequency

results. Even with the advent of the laser and the use of the highest

resolving power Fabry-Perot etalons, the measurement of the attenuation

is impossible.

To fully illustrate this point, consider the following example (23):

For typical sound velocities in liquids ($v_s \approx 1.5 \times 10^5$ cm/sec), the

maximum fractional Brillouin shift is approximately $(\omega_r' /\omega_o) \approx 10^{-5}$;

with a He-Ne laser source (λ_{air} = 6328Å) this corresponds to a splitting

of $(\omega_r' /2\pi) \approx 7000$ Mc/sec. The attenuation of such sound waves may

produce a line broadening of about $(\omega_r'' /\omega_o) \approx 10^{-8}$ - 10^{-6}, where ω_r'' is

the half-width at half-height. However, extending the light scattering

data down to an upper limit of conventional ultrasonic experiments

requires going to scattering angles where $(\omega_r' /\omega_o) \approx 5 \times 10^{-7}$ and

$(\omega_r'' /\omega_o) \approx 10^{-11}$ - 10^{-9}. A study of such splittings and line widths would

demand the ability to resolve details as fine as 10^{-12} of the incident

frequency. That is, out of an optical frequency of approximately

5×10^{12} cps, one must detect spectral features on the scale of cycles per second!

In 1961, Forrester (24) pointed out that optical mixing is a direct analog of the mixing of AC electrical signals in radio receivers. The objective then is to translate the desired spectral information from the high optical frequency ω_0, where a specified resolvable width may be difficult to achieve, down to a lower frequency ω_1, where the necessary width may be easily attained. The two types of translation processes, homodyne and heterodyne spectroscopy, for the radio region are also possible for the optical region. An excellent analysis of both methods of optical mixing spectroscopy is contained in the thesis of Lastovka (23).

Homodyne or self-beat spectroscopy is the result of only the signal falling on a non-linear element--a photodetector surface. The mixing takes place between the various spectral components of the signal itself because of the non-linear current versus optical electric field characteristic of the photoelectric effect. The result is that the photo-current spectrum contains a modified version of the spectral information that was originally present in the optical signal. This information is now centered around $\omega = 0$ rather than around the optical frequency $\omega = \omega_0$.

With the heterodyne or superheterodyne spectrometer, the light whose spectrum is to be analyzed is mixed with an intense monochromatic beam called the local oscillator on the photodetector surface. By a proper choice of the frequency of the local oscillator, the optical signal

spectrum can be shifted down to any desired frequency; the "mixer" output appears as an AC component in the photocurrent with a spectrum centered about the difference frequency between the local oscillator and the optical signal.

The homodyne method has been used to study the variation of the dielectric constant with density and non-hydrostatic strain (25), the thermodynamic entropy fluctuations at constant pressure (26), the variation in relative concentrations in a binary mixture (27), localized fluid flow measurements (28), and the ripplons at the interface of two fluids (29). The homodyne method has the serious disadvantage that one loses the information associated with the Doppler shift.

The heterodyne method retains this information, but less work has been done with it (30, 31, 32, 33) because of the difficulty in aligning the optics and in obtaining a reasonable mixing efficiency. It is the purpose of this thesis to develop a technique that eliminates these difficulties and to apply that technique to characterize the viscoelastic properties of interfacial ripplons at frequencies above 1000 Hz.

THEORY

To understand photon-ripplon interactions and their measurement by heterodyne spectroscopy, one is required to have a basic knowledge of hydrodynamic theory, light scattering theory and signal correlation theory. To insure that this is accomplished, the basic theory of these areas as applied to the work of this thesis will be explained.

A. Hydrodynamic Theory

This thesis is concerned with that portion of hydrodynamic theory pertinent to the capillary wave motion at an interface. There have recently appeared a number of review articles (34, 35, 36) that dealt with the theory of capillary ripples on interfaces and membranes. One should refer to them for a more detailed presentation.

Ripplons, as indicated by Katyl and Ingard (30), are the quasi-particles characterizing the capillary ripples on an interface. Mann (35) has pointed out that this characterization is valid since the ripple fluid dynamical field equations can be quantized. This quantization has been accomplished by Mann (University of Hawaii, personal communication in 1970) with the ripplons traveling with a momentum $\hbar \underline{k}_r$ and having an energy $\hbar \omega_r$, where $\underline{k}_r$ is the ripplon wave number associated with the ripple wave number $\underline{k}$ and ω_r is the ripplon frequency associated with the ripple frequency ω. Thus one can consider the ripple field interaction with the electromagnetic field from either the quantum interaction or the

classical wave interaction viewpoint. This thesis will proceed from the classical wave viewpoint.

The classical theory of capillary wave motion on an interface is based upon a linearized Navier-Stokes equation with solution required to satisfy normal and tangential stress boundary conditions at the interface. The linearized Navier-Stokes equation,

$$\rho \frac{d\underline{v}}{dt} = -\nabla \underline{P} + \mu \nabla^2 \underline{v} + \rho \underline{g} \tag{1}$$

where ρ = density of the fluid;

$\underline{v}$ = vector particle velocity;

$\underline{P}$ = hydrostatic pressure;

μ = viscosity of fluid; and

$\underline{g}$ = gravitational force vector,

follows from the non-linear Navier-Stokes equation if the wave amplitude is small compared to the wavelength and gravity is the only volume force exerted on the fluid (37). The resolution of surface forces includes the fact that the velocity components at the interface can be regarded as continuous (Eq. 2) and the balance of the normal (Eq. 3) and the tangential (Eq. 4) stress components at the interface (38).

$$(v_x)_{z \to o-} = (v_x')_{z \to o+} \tag{2a}$$

$$(v_z)_{z \to o-} = (v_z')_{z \to o+} \tag{2b}$$

$$\left(-\triangle P + 2\mu \frac{\partial v_z}{\partial z} \right)_{z \to o^-} - \left(-\triangle P' + 2\mu' \frac{\partial v_z'}{\partial z} \right)_{z \to o^+} = \gamma \frac{\partial^2 \zeta}{\partial x^2} \tag{3}$$

$$\mu \left(\frac{\partial v_z}{\partial x} + \frac{\partial v_x}{\partial z} \right)_{z \to 0^-} - \mu' \left(\frac{\partial v_z'}{\partial x} + \frac{\partial v_x'}{\partial z} \right)_{z \to 0^+} = \hat{E} \frac{\partial^2 \zeta}{\partial x^2} \tag{4}$$

where $\zeta = \int (v_z)_{z \to 0^+} \, dt$ and $\xi = \int (v_x)_{z \to 0^+} \, dt$ are the normal and

tangential displacements of the surface, respectively. In these

equations γ is the interfacial tension and $\hat{E}$ is the elastic modulus

modeled by

$$\hat{E} = \frac{k_e - i\omega \hat{k}_v}{\hat{D}} \, ,$$

where k_e is the sum of the surface dilational and shear elastic coefficients

(k^s and e^s) and $\hat{k}_v$ is a sum of surface dilational and shear viscosity

coefficients (ζ^s and η^s). $\hat{D}$ represents the diffusional transport of sur-

factant molecules on the surface and between the surface and the bulk

phases. An excellent discussion (39) of the significance of $\hat{D}$ on the

interfacial properties is available. The $\wedge$ over terms indicates that the

term is complex. The primed and unprimed terms refer to the phases

above and below the interface, respectively.

From this point one may proceed by using the potential and

stream functions to express the above equations (38) or by forming the

generalized stress and strain tensors (35). The function approach yields

four simultaneous equations which are incorporated into a determinant.

$$\begin{vmatrix} 1 & i & 1 & -i \\ ik & -m' & -ik & -m \end{vmatrix}$$

$$\begin{vmatrix} -i\hat{\omega}\rho' + 2\mu'k^2 & 2i\mu'm'k & i\hat{\omega}\rho - 2\mu k^2 - \dfrac{i\gamma k^3}{\hat{\omega}} & 2i\mu mk - \dfrac{\gamma k^3}{\hat{\omega}} \\ -2i\mu'k^2 & \mu'(m'^2 + k^2) & \dfrac{k^3\hat{E}}{\hat{\omega}} - 2i\mu k^2 & -\mu(m^2 + k^2) - \dfrac{imk^2}{\hat{\omega}}\hat{E} \end{vmatrix} = 0 \qquad (5)$$

where $m^2 = k^2 - i\rho\hat{\omega}/\mu$ and $m'^2 = k^2 - i\rho'\hat{\omega}/\mu'$. This determinant is reduced to the working ripple dispersion equation (Eq. 6) which expresses the surface properties of interfacial tension, the elastic modulus, and the viscosity in terms of the observable ripple wave number k and frequency $\hat{\omega}$.

$$-\gamma G\hat{E}k^5 + i\hat{\omega}\,[\,(\mu + \mu')k + (m\mu + m'\mu')\,]\,(\gamma G + \hat{E})k^3$$

$$+ \hat{\omega}^2 \left\{ 4\mu\mu'k^3 + [\,4(\mu^2 m + \mu'^2 m') + \hat{E}(\rho + \rho')\,]k^2 + 4\mu\mu'mm'k \right\}$$

$$-i\hat{\omega}^3\,(\rho + \rho')\,[\,\mu m + \mu'm' + (\mu + \mu')k\,] = 0 \ , \qquad (6)$$

where G is the correction for the gravity field (40) given by

$$G = 1 + \frac{g(\rho - \rho')}{\gamma k^2} \ .$$

Eq. 6 is called the working equation since it is by solving for the roots of this equation for given surface parameters that the theory is compared with experiment.

It should be noted that the coefficients for the powers of $\hat{\omega}$ have a dependence on $\hat{\omega}$ and thus one is not working with a true polynomial. It is possible to remove the dependence on $\hat{\omega}$ in m' and m by the following algebraic manipulation:

1) Rearrange Eq. 6 into terms dependent on m', m, and mm';

2) Since $\mu'm' \rightarrow 0$ for the air-fluid interface, the terms in $\mu'm'$ and

$\mu\, m\mu'm'$ can be dropped and both sides of the remaining equation are squared.

Working this out and collecting powers of $\hat{\omega}$ gives one a seventh degree polynomial:

$$\sum_{i=0}^{7} B_i\, \hat{\omega}^i = 0 \ , \tag{7}$$

where

$$B_0 = G^2\, \gamma^2\, \hat{k}_e^{\,2}\, k^{10} \ ;$$

$$B_1 = 2i\, G\, \gamma\, \hat{k}_e\, \hat{k}_v\, k^{10} + 2i\, \mu\gamma\, G\, k^9\, \hat{k}_e\, (\hat{k}_e + \gamma G) \ ;$$

$$B_2 = \hat{k}_v\, k^{10} + 2\mu k^9\, \hat{k}_v\, (G\gamma + \hat{k}_e - G\gamma\hat{k}_e) + 2G\gamma\rho\, k^7\, \hat{k}_e^{\,2} \ ;$$

$$B_3 = -2i\mu k^9\, \hat{k}_v^{\,2} + 2i\mu^2\, k^8\, (G\gamma + \hat{k}_e)\, (1 - \hat{k}_v)$$
$$\qquad - 2i\rho\, k^7\, \hat{k}_e\, \hat{k}_v\, (1 + G\gamma) + 8i\mu^3\, k^7\, (\hat{k}_e + G\gamma) \ ;$$

$$B_4 = 2k^7\, \hat{k}_v\, (4\mu^3 - \rho\hat{k}_v) + 2k^6\, [\ 8\mu^4 + \rho\,\mu\, G\gamma\, \hat{k}_v\, (1 - G\gamma) - \rho\mu^2\, \hat{k}_v$$
$$\qquad - \rho\mu\hat{k}_e\, \hat{k}_v\ ] + 6\rho\,\mu^2\, k^5\, (G\gamma + \hat{k}_e) - k^4\rho^2\, \hat{k}_e^{\,2}$$
$$\qquad + 2\rho k^3\, (G\gamma + \hat{k}_e) \ ;$$

$$B_5 = i\rho\,\mu k^6\, \hat{k}_v^{\,2} - 6i\rho\mu^2\, k^5\, \hat{k}_v - 2i\rho\mu k^5\, \hat{k}_v + 2i\rho^2\, k^4\, \hat{k}_e\, \hat{k}_v$$
$$\qquad -24i\rho^2\, \mu^2\, k^4 - 2i\rho^2\, \mu k^3\, \gamma\, G \ ;$$

$$B_6 = \rho^2\, k^2\, (k^2\, \hat{k}_v^{\,2} - 8\mu^2) \ ;$$

$$B_7 = -i\mu\rho^3 \ ;$$

with $\hat{k}_e = k_e / \hat{D}$ and $\hat{k}_v = \hat{k}_v / \hat{D}$.

It is to be remembered that additional roots will be introduced in this process and that only the roots of Eq. 6 may have physical signifi-cance. The numerical analysis techniques of Mann and Du (41) were used to solve Eq. 7 for the roots $\hat{\omega}$ as functions of bulk and surface properties

and k.

B. Scattering Theory

The essence of what occurs in the scattering of photons by ripplons can be thought of in terms of the electric field of the incident radiation, $\underline{E}_o(\underline{r}, t)$, which induces a dipole moment, $\underline{P}(\underline{r}, t)$, in the ripplons on the interface of the system. The induced dipoles reradiate light with a different electric field. Since the ripplons are not static, the frequency of this scattered light will be broadened in a way reflecting the movement of the ripplons. Exactly how this movement is related to the broadening can be deduced from the solutions to the Maxwell equations for scattered radiation.

Since the system under consideration is non-magnetic with no free charges, the Maxwell equations applicable are (42) :

$$\nabla \times \underline{E}_o = -\frac{1}{c}\frac{\partial \underline{H}}{\partial t} \quad ; \tag{8}$$

$$\nabla \cdot \underline{E}_o = 0 \quad ; \tag{9}$$

$$\nabla \times \underline{H} = \frac{1}{c}\frac{\partial (\bar{\epsilon}\, \underline{E}_o)}{\partial t} + \underline{j} \quad ; \tag{10}$$

$$\nabla \cdot \underline{H} = 0 \quad ; \tag{11}$$

where $\bar{\epsilon}$ is the dielectric constant of the fluid.

The induced dipole moment is proportional to the electric field through the dielectric constant tensor, $\underline{\underline{\epsilon}}$ (43).

$$\underline{P}(\underline{r}, t) = \frac{1}{4\pi}\underline{\underline{\epsilon}}(\underline{r}, t) \cdot \underline{E}_o(\underline{r}, t) . \tag{12}$$

The components of the dielectric constant tensor are given by (44) :

$$\epsilon_{ij} = \bar{\epsilon} + \Delta \epsilon_{ij} \tag{13}$$

$$\Delta \epsilon_{ij} = \Delta \epsilon \, \delta_{ij} + \Delta \epsilon'_{ij} \tag{14}$$

where $\bar{\epsilon}$ is the average dielectric constant, the averaging being performed with respect to space, time, and all directions; $\Delta \epsilon$ represents the fluctuations in the dielectric constant which do not alter the isotropy of the medium; $\Delta \epsilon'$ represents the fluctuations which do alter the isotropy; and δ_{ij} is the Kronecker delta symbol.

The current $\underline{j}$ in the dipole scattering approximation is (45)

$$\underline{j} = \frac{1}{c} \frac{\partial \underline{P}}{\partial t} = \frac{1}{4\pi c} \frac{\partial}{\partial t} [\underline{\underline{\epsilon}} \cdot \underline{E}_0 (\underline{r}, t)] . \tag{15}$$

This current is the source term that is put into the Maxwell equations to calculate the scattered radiation. By eliminating $\underline{H}$ from these equations, one obtains the wave equation:

$$\nabla^2 \underline{E}' - \frac{\bar{\epsilon}}{c^2} \frac{\partial^2 \underline{E}'}{\partial t^2} = \frac{1}{c^2} \frac{\partial^2 \underline{P}}{\partial t^2} , \tag{16}$$

where $\underline{E}'$ is the electric field of the scattered radiation.

Since one is working with a plane monochromatic light wave (46),

$$\underline{E}_0(\underline{r}, t) = \underline{E}_0 \exp(i\underline{k}_0 \cdot \underline{r} - i\omega_0 t) \tag{17}$$

and considering one particular frequency component, ω, of the scattered field,

$$\underline{E}'(\underline{r}, t) = \underline{E}' \cdot \exp i(\underline{k}_s \cdot \underline{r} - \omega t) \tag{18}$$

where the wave vector $\underline{k}_s$ of this component is related to the frequency by $|\underline{k}_s| = n\omega / c$, where n is the average index of refraction at the interface.

The wave equation can now be written as:

$$\left(\nabla^2 + \frac{\omega^2 \epsilon}{c^2}\right) \left\{ \underline{E}' \exp\left(i\left[(\underline{k}_o - \underline{k}_r)\cdot \underline{r} - (\omega_o - \omega_r)t\right]\right)\right\} = \frac{1}{4\pi c^2} \frac{\partial^2}{\partial t^2} \underline{\underline{\epsilon}} \cdot \underline{E}_o \quad , \quad (19)$$

where $\underline{k}_r$ ($= \underline{k}_o - \underline{k}_s$) is the change in the wave vector of the scattered radiation. When one recalls that the characteristic frequencies for the fluctuations in the dielectric polarizability are quite small compared with the optical frequency (46). this equation can be closely approximated by:

$$\left(\nabla^2 + \frac{\omega^2 \epsilon}{c^2}\right) \left\{ \underline{E}' \exp\left(i\left[(\underline{k}_o - \underline{k}_r)\cdot \underline{r} - (\omega_o - \omega_r)t\right]\right)\right\} = -\left(\frac{\omega_o}{c}\right)^2 \frac{1}{4\pi} \underline{\underline{\epsilon}} \cdot \underline{E}_o \quad . \quad (20)$$

Thus the far field solution to the wave equation is

$$\underline{E}'(\underline{R}, t) = -\left(\frac{\omega_o}{c}\right)^2 \frac{1}{4\pi R} \exp(i[\underline{k}_s \cdot \underline{R} - (\omega_o - \omega)t]) \int_A \underline{\underline{\epsilon}} \cdot \underline{E}_o \exp(i\underline{k}_r \cdot \underline{r}) dA' \quad , \quad (21)$$

where R is the distance from the scattering surface to the detector.

If the dielectric constant tensor is written out in component form in Eq. 21, the quantity $\underline{\underline{\epsilon}} \cdot E_o$ would be a constant independent of position r and one would have to integrate the quantity $\int_A \exp(i\underline{k}_r \cdot \underline{r}) dA'$ over the illuminated region. This integral is zero if $A \gg \lambda^2$ except for $\underline{k}_o = \underline{k}_s$. Thus the time-space average term makes no contribution to the scattering.

The $\Delta \underline{\underline{\epsilon}}$ is a thermodynamic quantity which, as a first approximation, can be represented by the sum of two terms, one representing pressure fluctuations and one representing entropy fluctuations. Since these fluctuations are uncorrelated, this term can be neglected.

The only remaining portion of the dielectric constant tensor is

$\Delta \underline{\epsilon}'$, which is what one expects according to Andronow and Leontowicz

(47), who imply that the scattered electric field is totally modulated by

the surface fluctuations.

Thus Eq. 21 can be rewritten as follows:

$$\underline{E}'(\underline{R}, t) = - (\frac{\omega_0}{c})^2 \frac{1}{4\pi R} \exp(i[\underline{k}_S \cdot \underline{R} - (\omega_0 - \omega)]) \int_A \Delta \underline{\epsilon}' \cdot \underline{E}_0 \exp(i\underline{k}_r \cdot \underline{r}) d A' .$$
$$(22)$$

Or in terms of $\underline{k}_r$,

$$\underline{E}'(\underline{k}_r, t) = - E_0 (\frac{\omega_0}{c})^2 \frac{\exp(i[\underline{k}_S \cdot \underline{R} - (\omega_0 - \omega)t])}{2R} \sin(\frac{\pi}{2} - \theta_p) \Delta \underline{\epsilon}'(\underline{k}_r, t) , \qquad (23)$$

where θ_p is the angle between the direction of polarization of the incoming

light wave and the perpendicular to the direction of ripple propagation

and $\Delta \underline{\epsilon}'(\underline{k}_r, t)$ is the vector component of the dielectric constant due to

the non-isotropic fluctuations. This equation describes the superposition

of phases of waves scattered from each ripplon on the surface area.

Since this thesis involves quasi-elastic scattering, $|\underline{k}_s|$ is

approximately equal to $|\underline{k}_o|$ (48), and the geometry of the system gives

the length of the ripplon wave vector as $|\underline{k}_r| = 2k_0 \sin(\theta/2)\cos\phi,$ (24)

where ϕ is the angle between a tangent vector pointing along the interface

and a vector defined by $\underline{k}_0 - \underline{k}_s$ and is required for the added constraint

that the ripplons move on a surface of defined orientation to the incident

pencil. See Figure 1.

One can also arrive at this result from the scalar theory of light.

Since the experimental design lends itself to this description, a few

salient features will be pointed out. Mann (University of Hawaii, personal

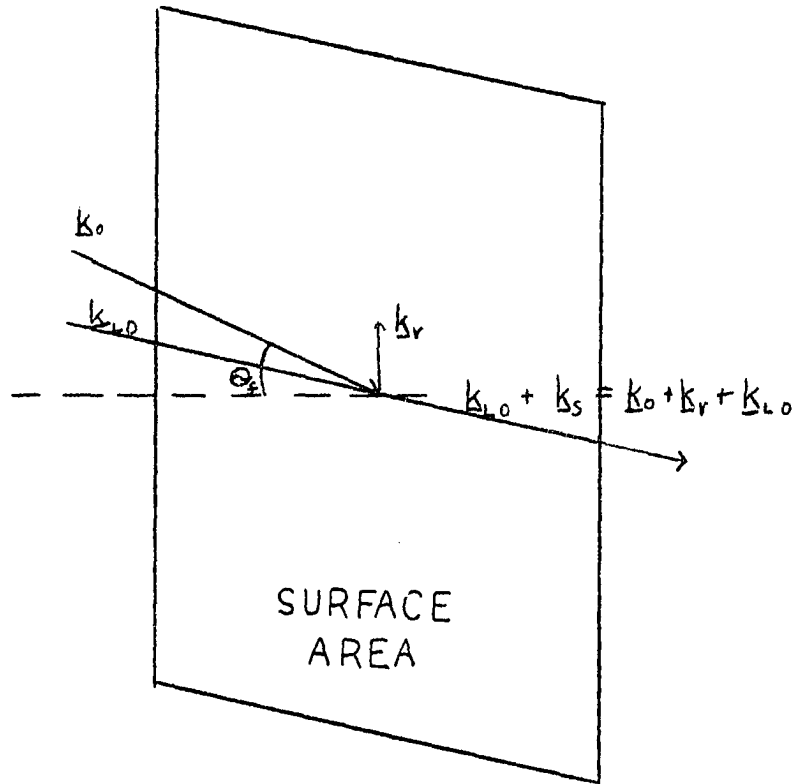Figure 1. The basic heterodyne photon-ripplon wave vector interaction diagram. $\underline{k}_{lo}$ is infinitesmally close to $\underline{k}_s$ and these two wave vectors beat together on the photodetector. For this thesis, $\theta_f = \theta/2$.

communication in 1970) made use of the approach of Rudd (49), illustrating its usefulness. The incident light upon two circular apertures will yield an interference pattern described by the superposition of two Airy circles. The interference pattern is the intensity distribution of the field with respect to the position on the image plane. The intensity can be written as

$$I(x) = \left[F\left(\frac{x}{\lambda}\right) \right]^2 \cos^2\left(\frac{kx \sin\theta}{2}\right) , \tag{25}$$

where the first term would be the Airy function and the second term would have a period

$$m\pi = \frac{2\pi x}{\lambda} \cdot \frac{x_0}{L} , \tag{26a}$$

or

$$x = \frac{L\lambda m}{2x_0} , \quad m = 0, 1, 2, \ldots \tag{26b}$$

where x is the position on the image plane; $2x_0$ is the center to center distance of the circular apertures; L is the distance from the apertures to the image plane; and λ is the wavelength of the incident radiation. Thus the reciprocal of the distance between the fringes is

$$k_f = \frac{2\pi}{\Delta x} = k_0 \frac{2x_0}{L} . \tag{27}$$

Now since $2x_0 \ll L$, $\sin\theta$ of Eq. 24 can be closely approximated by $2x_0 / L$ and $\phi = 0°$, so that

$$k_r = k_0 \frac{2x_0}{L} . \tag{28}$$

Therefore, to the extent that the fringes are sharply defined, complete correlation will occur only between the ripplons of wave number

k_r equal to the reciprocal fringe separation k_f. See Figure 2.

As stated in the introduction, beat frequency spectroscopy is the combination of a modulated signal with a carrier signal with the result that the central frequency of the carrier wave is shifted to a different frequency by their non-linear mixing on a photodetector. It is illustrative to use the photon-ripplon model to show how this frequency beating is accomplished by our experimental apparatus. The two circular apertures act as two mutually coherent sources sending two beams to a superimposed focus on the ripplon field. Each beam produces a scattering field with the scattering photon momentum balance given by:

$$\hbar \underline{k}_{s1} = \hbar \underline{k}_{o1} - \hbar \underline{k}_{r1} \quad ; \tag{29a}$$

$$\hbar \underline{k}_{s2} = \hbar \underline{k}_{o2} - \hbar \underline{k}_{r2} \quad . \tag{29b}$$

The heterodyne effect on the photodetector will result from the imposing of the $\underline{k}_{s1}$ on the $\underline{k}_{o2}$ field and the $\underline{k}_{s2}$ on the $\underline{k}_{o1}$ field. The heterodyne coupling will be greatest for those photons whose wave vectors obey $\underline{k}_{s1} \times \underline{k}_{o2} = 0$ and $\underline{k}_{s2} \times \underline{k}_{o1} = 0$ -- that is, the wave vectors are collinear. See Figure 3. Slight phase mismatching will rapidly force the coupling to zero. Scattered photons coming into the detector slightly off angle will add to the DC component of the photocurrent but not to the power spectrum (50).

DIFFRACTION   PATTERN

RIPPLING   INTERFACE
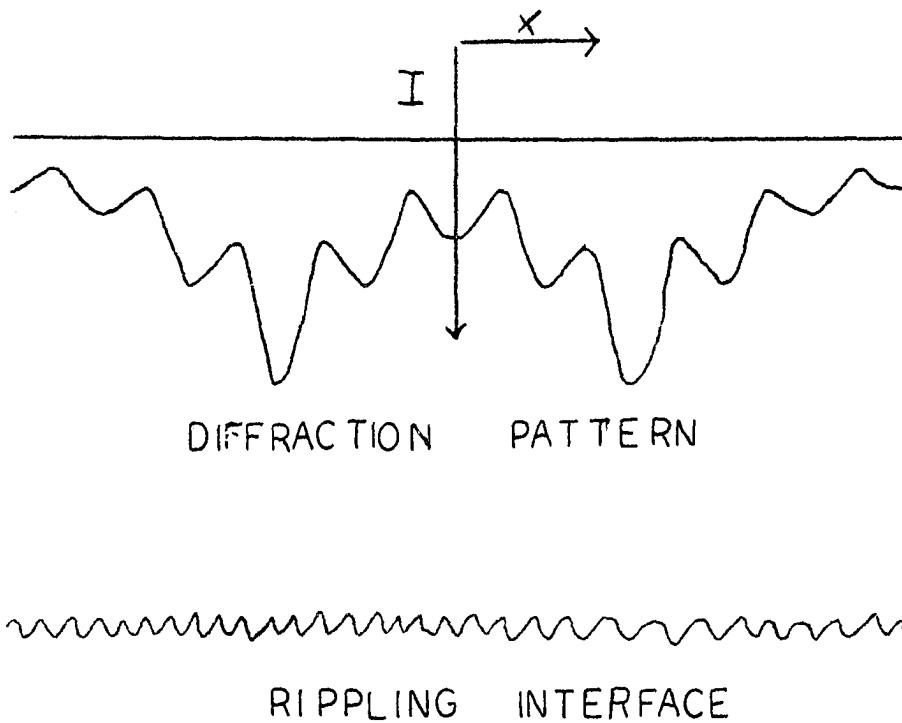
Figure 2.   The diffraction pattern will interfere constructively only with
those ripples that satisfy the selection condition Eq 27.   This
is observed as a "twinkling" of the fringes after they pass
through the interface.

A PERTURE
SCREEN

FLUCTUATING
SURFACE

$\underline{k}_{o1}$

X_o

$\frac{1}{2}\theta$

$\underline{k}_{o2}$

$\underline{k}_{r1}$

$\underline{k}_{r2}$

$\underline{k}_{s1} + \underline{k}_{o2}$

$\underline{k}_{s2} + \underline{k}_{o1}$

L

Figure 3.   The photon-ripplon wave vector balance for the experimental method of this thesis.

C. Signal Correlation Theory

Several closely related approaches have been developed to handle the output of the detector. These include spectrum analysis, direct signal correlation measurement, and photon counting. In spectrum analysis, two schemes have been used: the heterodyne detection and the homodyne detection. Since most sources go through the homodyne considerations and since this thesis work was done only with the heterodyne system, only the heterodyne system will be discussed here.

According to the Wiener-Khintchine theorem (51), the power spectrum $G_i(\omega)$ of the photocurrent and the current correlation function $R_i(\tau)$ are related through the equation:

$$G_i(\omega) = \frac{1}{2\pi} \int_{-\infty}^{\infty} e^{i\omega\tau} R_i(\tau) d\tau \qquad (30)$$

where

$$R_i(\tau) = \langle i(t)i(t+\tau)\rangle = \lim_{T\to\infty} \frac{1}{2T} \int_{-T}^{T} i(t+\tau)i(t)dt \qquad (31)$$

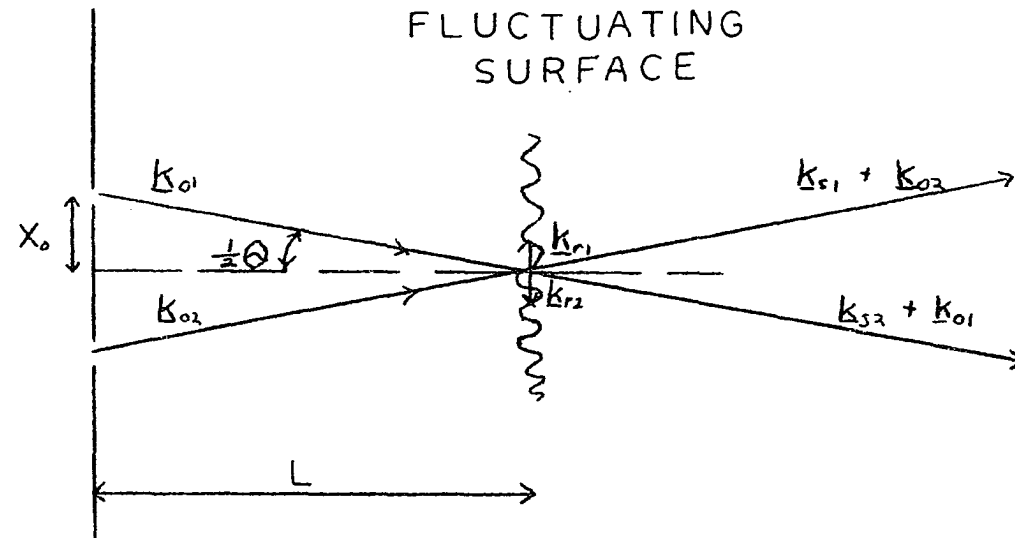and $i(t)$ is the photoelectric current. The instantaneous intensity $I(t) = E^*(t)E(t)$ is responsible for the photoelectric current $i(t)$ (43):

$$i(t) = eW^{(1)}(t) = e\alpha E^*(t)E(t) \qquad (32)$$

where α is a suitably defined quantum efficiency, e is the electronic charge, and $W^{(1)}$ is the probability per unit time of photoelectron emission from the photocathode. α is made up of the gain G and the quantum efficiency η of the photomultiplier. $R_i(\tau)$ has two distinct contributions

(52):

1. If the electrons at t and t + τ are distinct, the average of the joint probability $W^{(2)}(t, t + \tau)$ has the form

$$\langle W^{(2)}(t, t + \tau) \rangle = \alpha^2 \langle E^*(t) E(t) E^*(t + \tau) E(t + \tau) \rangle \quad (33a)$$

$$= \alpha^2 \langle I \rangle^2 g^{(2)}(\tau) \quad (33b)$$

where $g^2(\tau)[= \langle E^*(t)E(t)E^*(t + \tau)E(t + \tau) \rangle / \langle E^*(t)E(t) \rangle^2]$ is the normalized correlation function and $\langle I(t) \rangle [= \langle E^*(t)E(t) \rangle]$ is the average intensity.

2. If the _same_ electron occurs at t and t + τ,

$$\langle W^{(1)}(t) W^{(1)}(t + \tau) \rangle = \langle W^{(1)}(t) \rangle \delta(\tau) = \alpha \langle I \rangle \delta(\tau) \quad . \quad (34)$$

Thus,

$$R_i(\tau) = e \langle i \rangle \delta(\tau) + \langle i \rangle^2 g^{(2)}(\tau) \quad . \quad (35)$$

Similarly the spectrum of a light wave is related to the time-dependence of its electric field through a statistical average quantity-- the autocorrelation function $R_E(\tau)$ defined by:

$$R_E(\tau) = \langle E^*(t)E(t + \tau) \rangle = \langle I \rangle g^{(1)}(\tau) \quad . \quad (36)$$

One now needs a relationship between $g^{(2)}(\tau)$ and $g^{(1)}(\tau)$. When the electric field is Gaussian, the relationship is

$$g^{(2)}(\tau) = 1 + \left| g^{(1)}(\tau) \right|^2 \quad ,$$

which is what one assumes in working with the homodyne method. But, as will soon be obvious, the heterodyne method does not require Gaussian statistics for the signal field. Also one retains the phase information in heterodyne spectroscopy which one loses in the homodyne method (44).

In heterodyne detection, the photomultiplier tube is illuminated simultaneously by the field under study: $E'(t) = \delta E(t)\exp(i\omega_s t)$ and by a coherent local oscillator signal: $E_{lo}(t) = E_{lo}^o \exp(-i\omega_{lo} t)$. Since E_{lo}^2 is constant,

$$\langle i_{lo}(t) \rangle = e\alpha \langle E_{lo}^*(t) E(t) \rangle = e\alpha |E_{lo}|^2 . \tag{37}$$

One recalls:

$$R_i(\tau) = e^2\alpha\,\delta(\tau) \langle E^*(t)E(t) \rangle + e^2\alpha^2 \langle E^*(t)E(t)E^*(t+\tau)E(t+\tau) \rangle . \tag{38}$$

Now $E(t) = E'(t) + E_{lo}(t)$, so that Eq. 38 has a very complex form. Edwards et al. (53) have analyzed the real part of the last term in Eq. 38 very carefully by writing the local oscillator term as:

$$E_{lo}(t) = A(t)\cos[\omega_{lo}t + \alpha(t)] , \tag{39}$$

where ω_{lo} is the angular frequency of the laser and α is the phase angle, and the scattered field as:

$$E'(t) = B(t)\cos\left\{[\omega_{lo} + \omega_r(t)]t + \alpha(t + \frac{\Delta s}{c}) + \Delta\alpha(t)\right\} , \tag{40}$$

where $\omega_r(t)$ is the Doppler shift introduced during the scattering process by the motion of the ripplons, $\Delta\alpha(t)$ is the random phase shift caused by the random positions of the ripplons, and Δs is the difference in path length between the scattered and reference beams. For the heterodyne method used for this thesis, $\Delta s = 0$.

When Eq. 39 and Eq. 40 are used in Eq. 38, the last term results in sixteen terms. Of these sixteen, ten only contain terms of the form $\langle \cos[\Delta\alpha(t)] \rangle$, $\langle \cos[\Delta\alpha(t+\tau)] \rangle$, or $\langle \cos[\Delta\alpha(t) + \Delta\alpha(t+\tau)] \rangle$ which are all zero because $\Delta\alpha(t)$ is a random variable.

Three of the non-zero terms are time independent terms and will contribute only to the DC component of the output of the photomultiplier. Their sum is:

$$\langle E_{lo}^2(t)E_{lo}^2(t+\tau)\rangle + \langle E_{lo}^2(t)E'^2(t+\tau)\rangle + \langle E_{lo}^2(t+\tau)E'^2(t)\rangle =$$

$$\langle \frac{1}{4}A^2(t)A^2(t+\tau)\rangle + \langle \frac{1}{4}A^2(t+\tau)B^2(t)\rangle + \langle \frac{1}{4}A^2(t)B^2(t+\tau)\rangle \quad , \quad (41)$$

where the components at $2\omega_{lo}$ have been excluded since the photodetector will not respond at those frequencies.

One of the non-zero terms is the result of the scattered radiation beating against itself.

$$\langle E'^2(t)E'^2(t+\tau)\rangle = \langle \frac{1}{4}B^2(t)B^2(t+\tau)\rangle \quad . \quad (42)$$

This is the term examined when one is dealing with homodyne spectroscopy.

The two remaining non-zero terms arise from the beating of the scattered field and the local oscillator field on the photodetector. These are the terms which contain the information one seeks.

$$\langle E_{lo}(t)E_{lo}(t+\tau)E'(t)E'(t+\tau)\rangle = \langle A(t)B(t)A(t+\tau)B(t+\tau)$$

$$\cdot \cos[\omega_r(t+\tau) + \Delta\alpha(t+\tau) + \alpha(t) - \Delta\alpha(t)]\rangle$$

$$+ \langle A(t)B(t)A(t+\tau)B(t+\tau)\cos[\omega_r(t+\tau) - \Delta\alpha(t+\tau) + \alpha(t) + \Delta\alpha(t)]\rangle \quad . \quad (43)$$

At this point one reintroduces the imaginary part of the terms and notes that since $I_{lo} >> \langle I_s\rangle$, the current correlation function is

$$R_i(\tau) = ei_{lo}\delta(\tau) + i_{lo}^2 + i_{lo}\langle i_s\rangle [e^{i\omega_{lo}\tau}g^{(1)}(\tau) + e^{-i\omega_{lo}\tau}g^{(1)}(\tau)] \quad , \quad (44)$$

which does <u>not</u> involve $g^{(2)}(\tau)$. Thus the photocurrent spectrum for

heterodyne detection system has the form:

$$G_i(\omega) = \frac{ei_{lo}}{2\pi} + i_{lo}^2 \delta(\omega) + \frac{i_{lo}\langle i_s \rangle}{2\pi} \int_{-\infty}^{\infty} e^{i\omega\tau} [\, e^{i\omega_{lo}\tau} g^{(1)}(\tau) + e^{-i\omega_{lo}\tau} g^{(1)*}(\tau) \,]$$

$$\cdot\, d\tau \quad , \tag{45}$$

which consists of a shot noise term, a DC term, and the heterodyne light

beating spectrum (53).

Since the light source is coherent, the scattered light falling on the

photodetector will have the same normalized autocorrelation function as

the dielectric fluctuation--that is, $\exp[\,-\omega_r'' t\,]$ (46). One can now write

$$g^{(1)}(\tau) = e^{-i\omega_s \tau} e^{-\omega_r'' |\tau|} \quad , \tag{46}$$

where the $\exp(i\omega_s\tau)$ term represents the fact that the light is centered

around the optical frequency. Therefore,

$$G_i(\omega) = \frac{ei_{lo}}{2\pi} + i_{lo}^2 \delta(\omega) + \frac{2\omega_r'' i_{lo} \langle i_s \rangle}{\pi(\omega - |\omega_s - \omega_{lo}|)^2 + \pi\omega_r''^2} \quad . \tag{47}$$

The heterodyne light beating spectrum is a Lorentzian of half-width at

half-height $\Delta \omega_{\frac{1}{2}} = \omega_r''$, centered at $\omega = (\omega_s - \omega_{lo})$, with an intensity

proportioned to i_{lo} and $\langle i_s \rangle$. See Figure 4.

There are two considerations that must be made if one is to have a

realistic idea of the applicability of the heterodyne spectroscopic method.

These are the coherence area, ΔA, which is the region on the scattered

wave front over which there is spatial coherence, and the heterodyne

mixing efficiency, ϵ, which is the degree to which the scattered wave

and the local oscillator wave have matched wave fronts. Once one knows
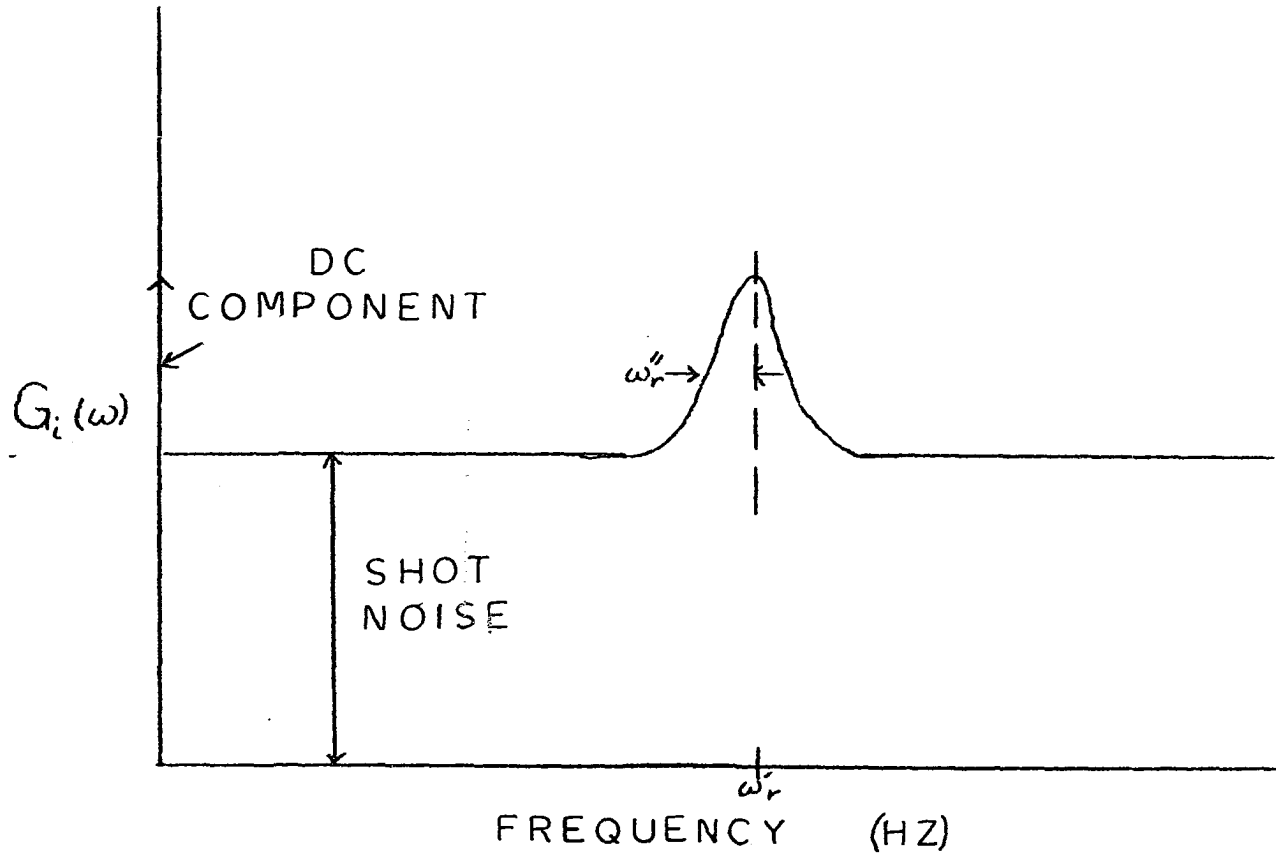
Figure 4. The theoretical power density spectrum for the heterodyne spectroscopy detection system.

these, one will have an idea of the signal-to-noise ratio that one can expect.

If $\omega = |\omega_s - \omega_{lo}|$, this ratio at the photodetector is given by (35)

$$\frac{S}{N}\bigg)_{PD} = 4\epsilon^2\eta\left(\frac{dn}{dt}\right)_{\Delta A}\frac{1}{\omega''_r} \tag{48}$$

where $\left(\frac{dn}{dt}\right)_{\Delta A}$ is the number of scattered photons per second crossing each coherence area. After detection the signal-to-noise ratio is (50)

$$\frac{S}{N}\bigg)_{POST} = \frac{S/N\big)_{PD}}{S/N\big)_{PD}+1}\sqrt{\omega''_r\tau} \quad , \tag{49}$$

where τ is the time constant for the entire detector system. The two limiting situations are:

1. $S/N\big)_{PD} \ll 1$ so that $S/N\big)_{POST} = 4\epsilon^2\eta\left(\frac{dn}{dt}\right)_{\Delta A}\sqrt{\frac{\tau}{\omega''_r}}$ (50)

2. $S/N\big)_{PD} \gg 1$ so that $S/N\big)_{POST} = \sqrt{\omega''_r\tau}$. (51)

It is to be noted that for the optimal signal-to-noise ratio, one wants to make the size of the scattering region small so that the coherence areas in the scattered field will be as large as possible since the coherence area is proportional to $(dn/dt)_{\Delta A}$ (51). $\epsilon = 1$ for the experimental apparatus of this thesis.

For a discussion of the scattered signal handling of other techniques, one is referred to Arrechi (54) for the photon counting method, and to Seigel and Wilcox (55) for the direct correlation measurement method.

EXPERIMENTAL SECTION

A schematic of the experimental set-up is shown in Figure 5. The light pencil from a laser passes through an aperture screen onto the interface which has ripples of random frequency imposed on it. The light scattered by the fluctuations and the non-scattered light pass through a collecting lens and an interference filter which focuses the selected light to a point on the photodetector. The photocurrent from this photodetector is fed into a wave analyzer which is driven repeatedly through a pre-set frequency range by a multichannel analyzer. After a given number of scans at that frequency range, the signal intensity versus frequency is read out on an x-y recorder. Each of the elements of this set-up will now be described in more detail.

A. Laser System

An Orlando Research Model 400 Argon-ion laser was used as the light source for the experiments. This laser is of the anodic-bore ion laser type which consists of three primary elements: a DC power supply, a plasma tube, and optics. Unlike conventional discharge tube designs, the anodic-bore tube has three electrically active elements. These elements are the cathode, anode and secondary anode. See Figure 6. These elements and the magnetic solenoid interact with the plasma through electrostatic means which prevent direct interaction with plasma ions. Thus, these elements can be considered as electronic elements which
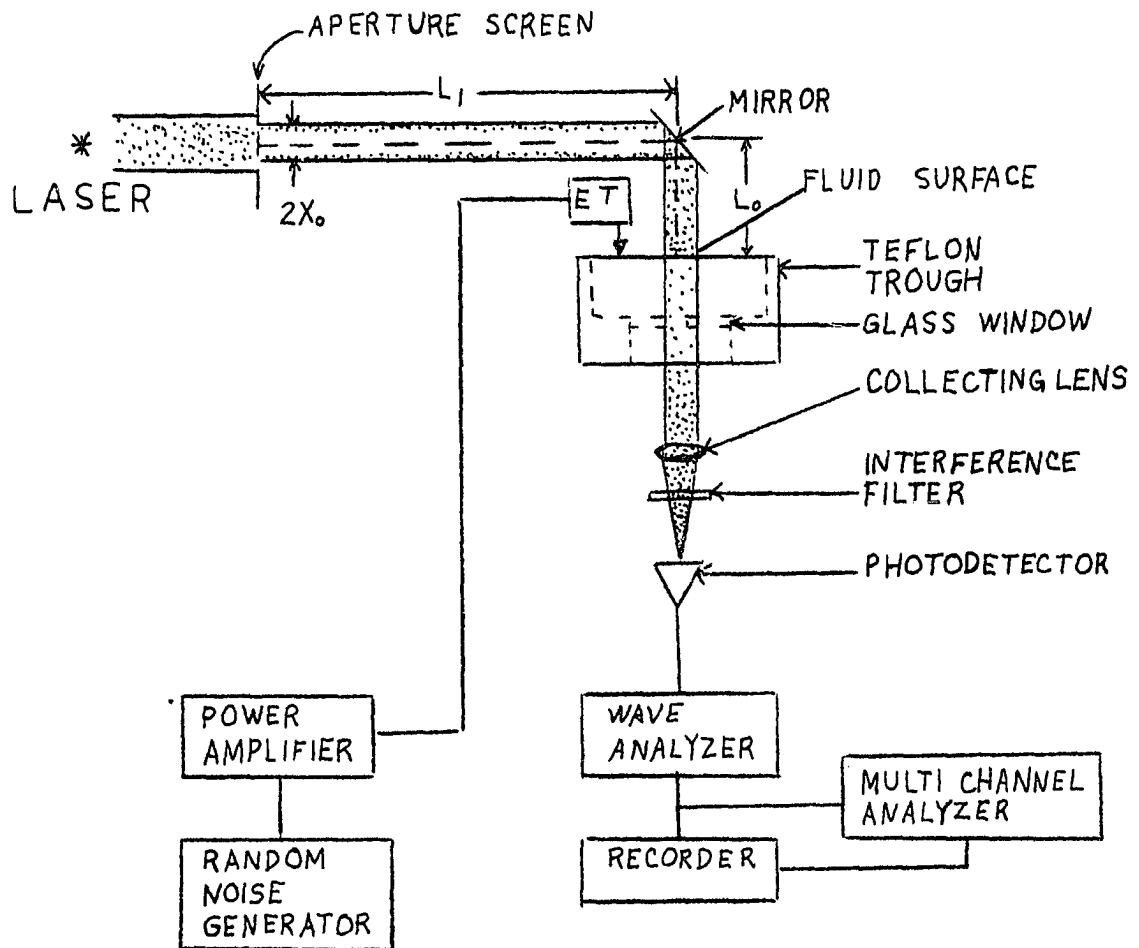
Figure 5. Block diagram of the experimental arrangement for liquid-gas interfaces. The electromechanical transducer is identified by ET and drives an L shaped probe represented by an arrow in the diagram.
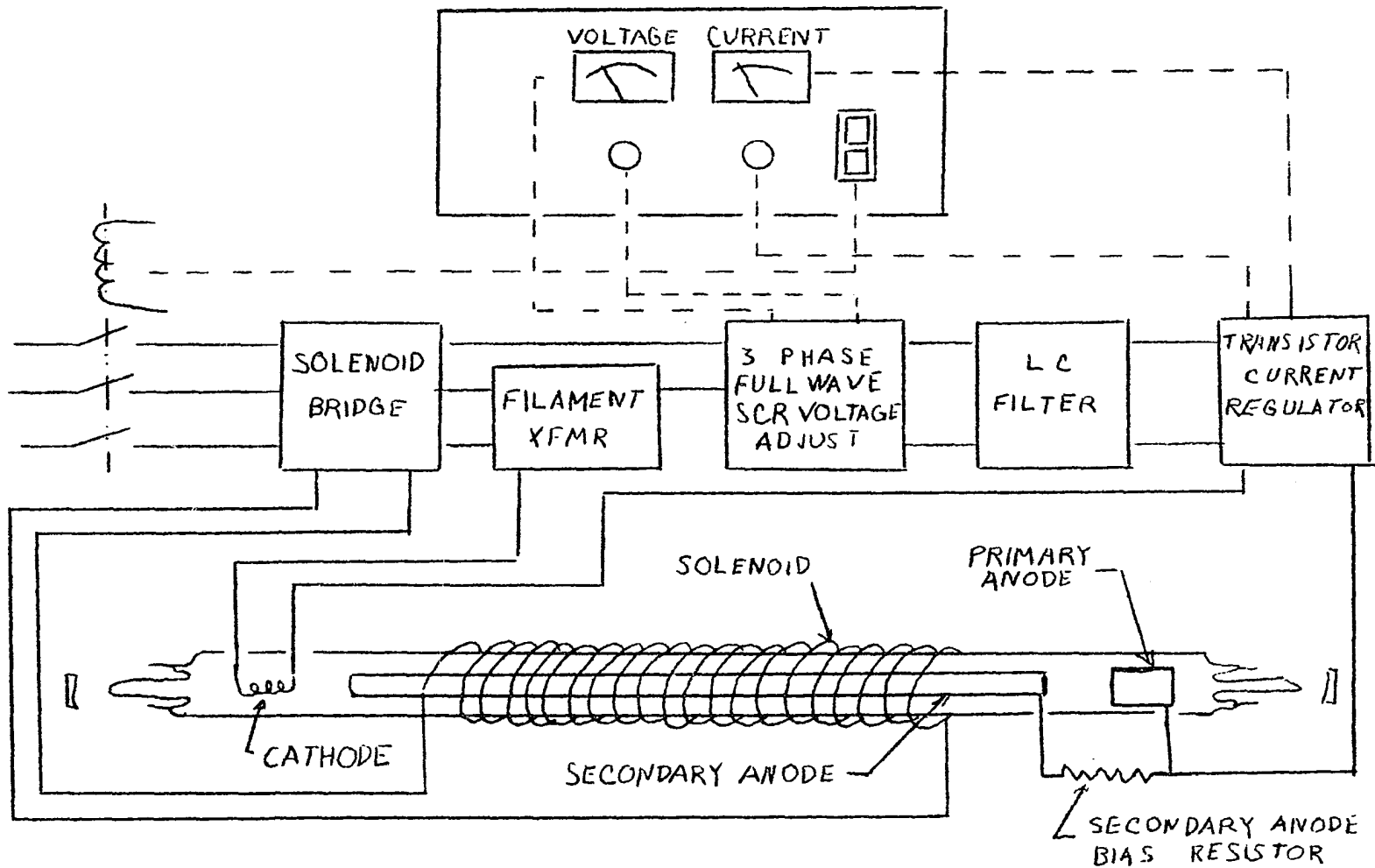
Figure 6. Anodic bore laser system..

utilize the plasma as a power coupling medium. The subsequent removal

of direct ion interaction eliminates deteriorating sputtering or other ion

impact effects from occurring in the anodic-bore plasma tube and thus

permits its construction as a sealed tube.

The laser head, depicted in Figure 7 contains the laser optics, the

plasma tube and magnetic solenoid. The power supply contains a DC

anode power supply for plasma tube power, a DC solenoid power supply

and filament heater power. Along with coolant lines, the umbilical cord

connecting the laser head to the power supply contains one wire (no. 1)

for the anode, two wires (no. 2 and no. 3) for the filament, and two wires

(no. 4 and no. 5) for the solenoid power. The sequence for activating

the plasma tube is to supply filament heat until the filament has reached

its proper temperature (about one minute), to activate the solenoid and

then to activate the main DC power supply. That power supply delivers

operating voltage and current to the plasma tube electrodes. A resistor

in the laser head supplies the proper bias voltage and current to the

secondary anode from the primary anode power source, and the tube

self-ignites.

The DC power supply is a transistor regulated supply. The voltage

is monitored and controlled on the front panel of the power supply. The

current regulator uses silicon power transistors to achieve an amplifier

capable of 2500 watts dissipation at up to 100 volts potential. This

amplifier is driven by a control circuit which senses the potential across
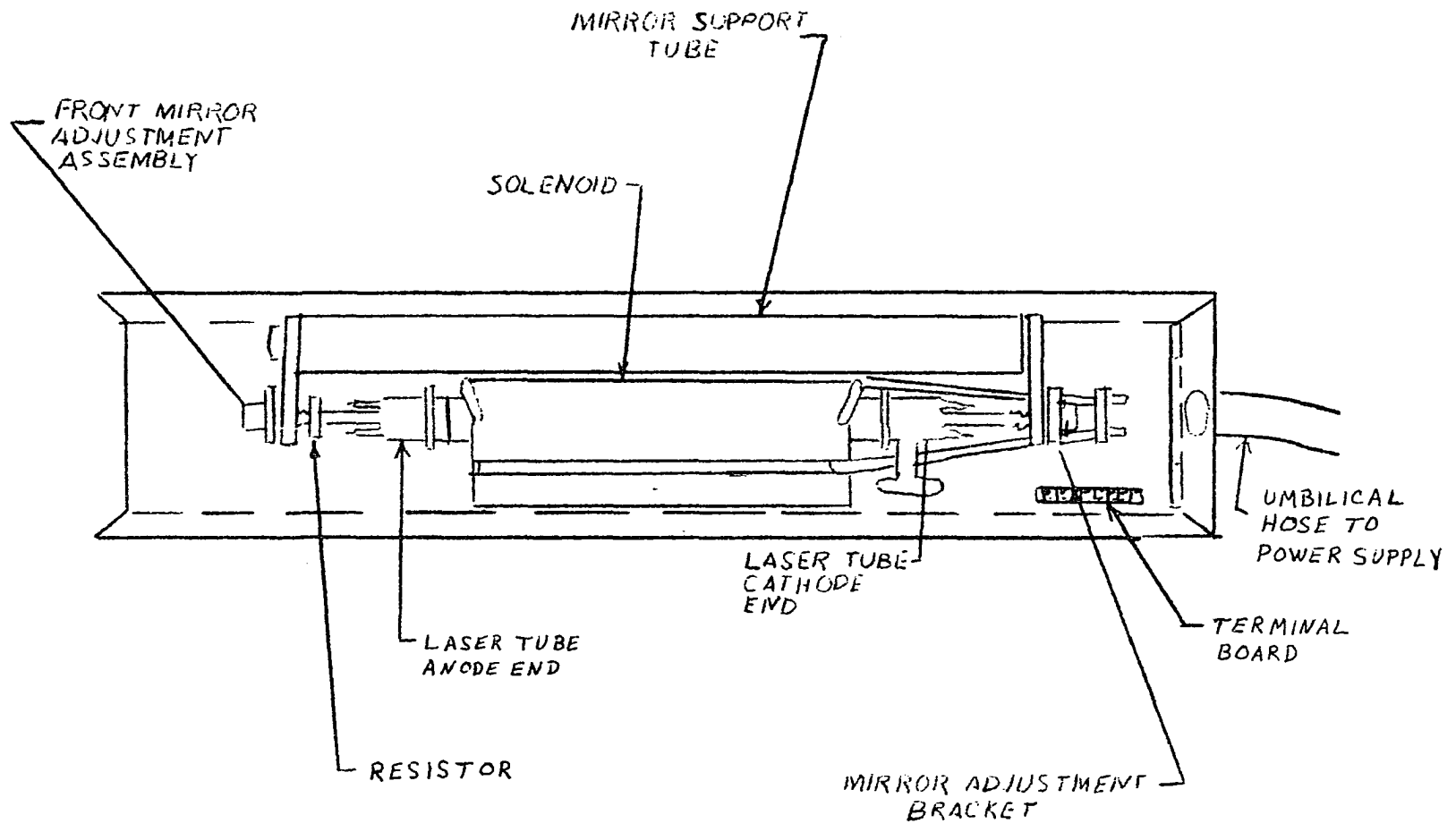
Figure 7. Orlando Research Model 400 laser head diagram.

a reference resistor in series with the tube. The current regulation bandwidth is a minimum of one Megahertz. The regulator responds to current variations originating either in the power supply or in the plasma tube.

Laser action in the anodic-bore ion laser is generated within the secondary anode by a plasma discharge sustained by the cathode and secondary anode. Optical gain is generated in this plasma at certain · wavelengths (4579 Å, 4657 Å, 4765 Å, 4727 Å, 4880 Å, 4965 Å, 5079 Å and 5145 Å) corresponding to transitions between specific energy levels of the ion. Laser action is obtained by creating a regenerative optical path through the secondary anode for which the optical gain exceeds optical losses. This is achieved by terminating the plasma tube with highly transparent windows and aligning mirrors on each end of the plasma tube to create the regenerative optical path through the tube. The rear mirror has a maximum reflectance and the front transmits about ten per cent of the laser power incident upon it. Laser action is achieved on the several wavelengths specified, and single wavelength operation at 4880 Å is achieved by introducing a dispersive Littrow prism in place of the rear reflector. Normal operation of the laser generates laser action in only one transverse resonant mode but in several longitudinal resonant modes, each propagating in the same direction but having different frequencies and wavelengths. Each longitudinal mode is separated from an adjacent mode by about 15 Gigahertz. Since the detection apparatus

employed only detects signals up to 120 KHz, there is no danger of inter-
fering mode hopping.

There is a background noise problem in the low frequency region
of the power spectrum of the laser. The anticipated peaks at multiples
of the power line are observed in the power spectrum. See Figure 8.
This base line spectrum also has a broad but low intensity band between
5000 Hz and the frequency range in which the electrical circuit roll-off
seems to become important (100 KHz). The background spectrum must
be well characterized for accurate line shape determination. It is easy
to select a k_r range for study that gives Brillouin shifts that are above
the noisy region between 10 Hz and 50 Hz. So although the argon
ion laser is somewhat noisy in the low frequency region below 500 Hz, it
appears satisfactory for accurate line shape work at frequencies above
500 Hz.

The stability of the laser is indicated in Figure 9, where the output
of the laser is plotted versus time. Because of the instability and drift
of the laser when first turned on, data are not to be collected during the
first quarter hour of operation.

B. Aperture System

The aperture screen serves to divide the laser light wave front
into two interfering light pencils. The screen used consisted of two small
circular holes positioned close together on an otherwise opaque screen.
The aperture screen is precisely positioned on a capping end of a short
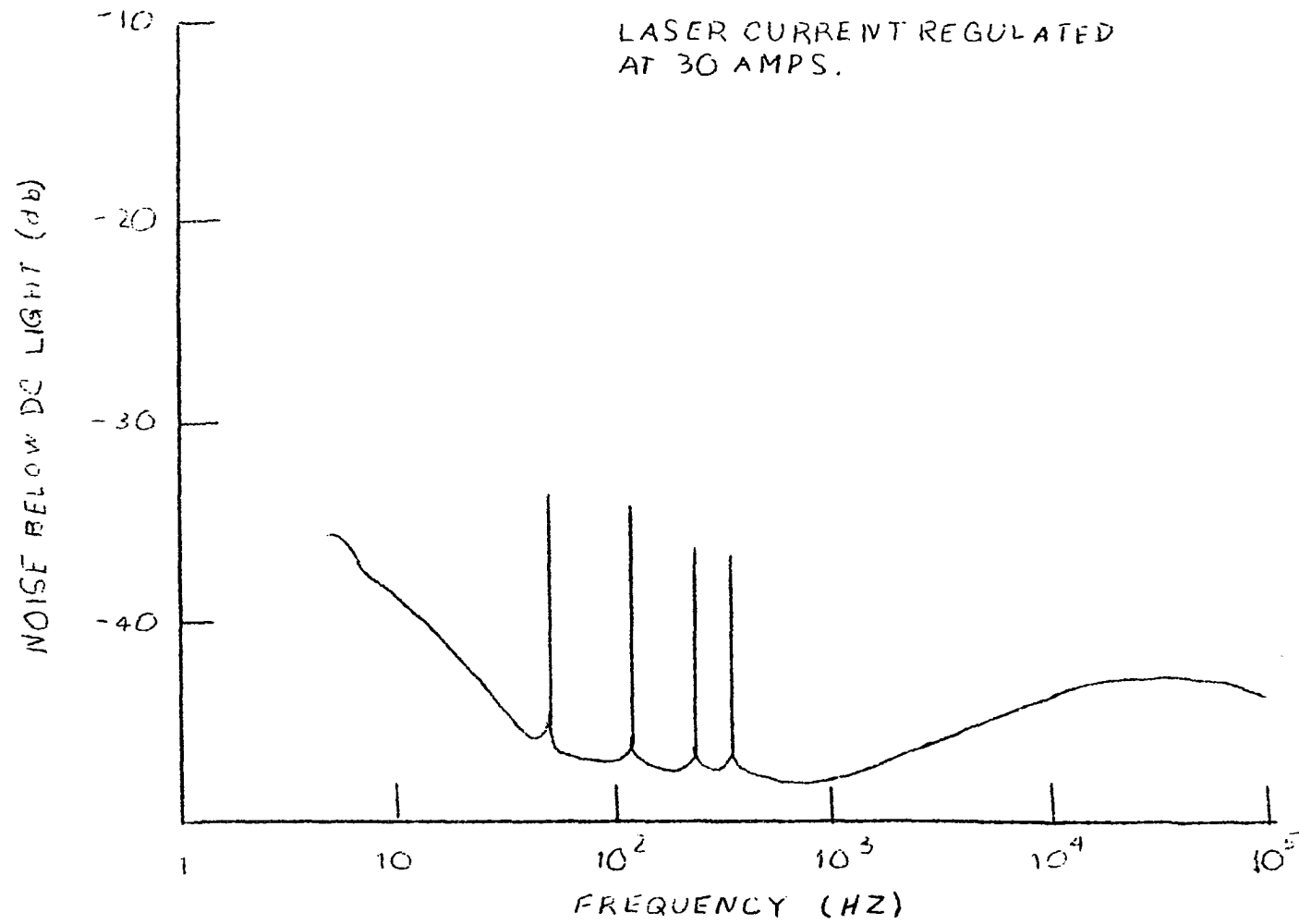
Figure 8. Low frequency noise spectrum of laser for Coherent Radiation Argon ion laser.
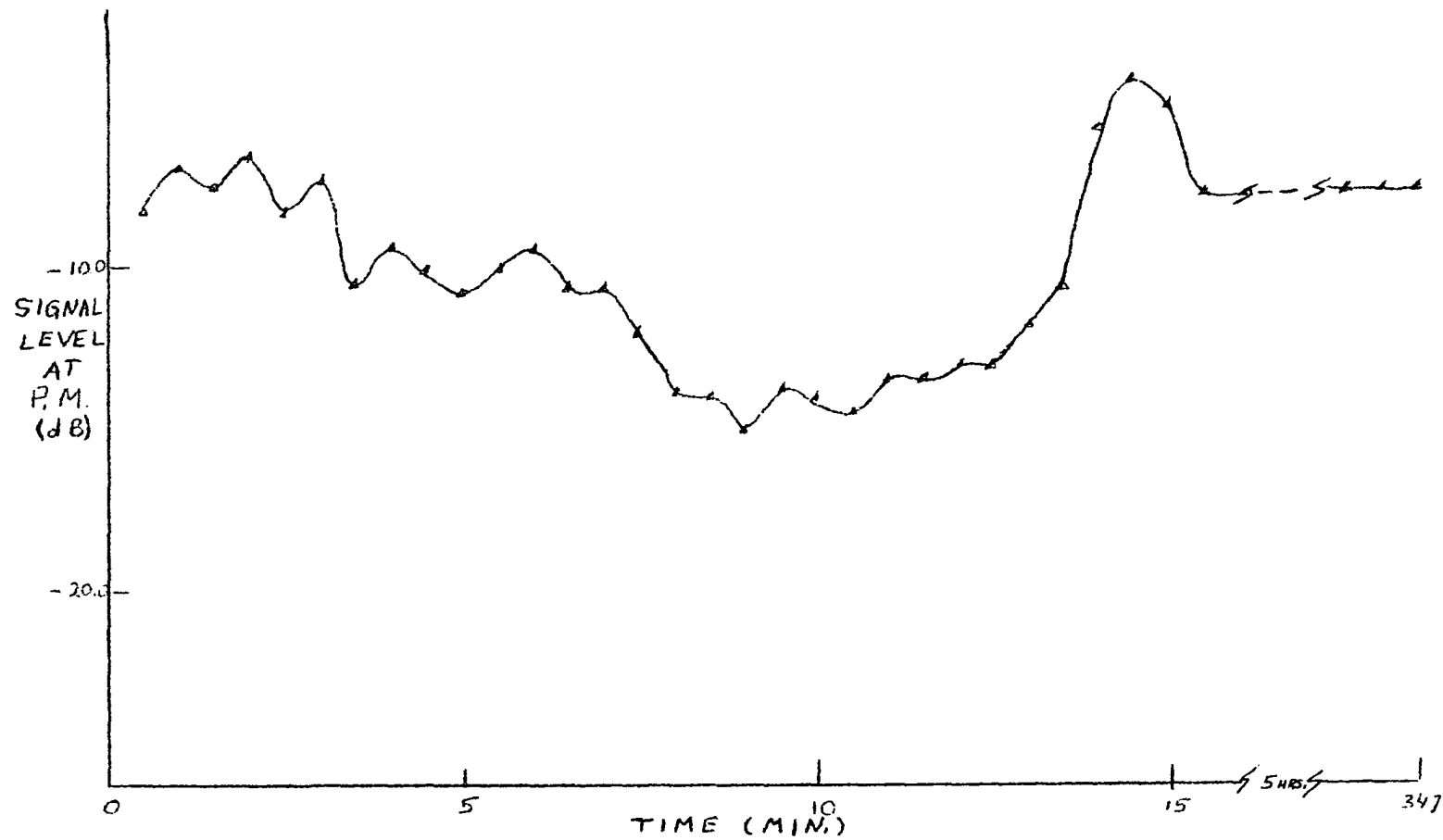
Figure 9. The stability of the laser power output at 25 amps and 38 volts DC.

metal tube. This tube is inserted into a Tropel Model 7600 mirror mount and aligned so that the apertures are positioned symmetrically with respect to the optical axis. The optical bench is of sufficient quality that the alignment could be retained while the position of the aperture screen was varied between 26.0 cm and 78.0 cm from the rippling interface. See Figure 10. The end piece holding the aperture screen could be rotated without destroying the alignment.

The determination of k_r for any position of the aperture screen on the optical bench was made by photographing the fringe pattern with a lens-less stationary Polaroid camera. The wave number of the fringes is proportional to the reciprocal of the distance between adjacent fringes. (See Equation 24.) The values of k_r for various positions are shown in Figure 11 with the numbers recorded in Table I.

C. Random Rippling System

The electromechanical transducer is driven by a General Radio Type 1390-B Random Noise Generator whose output is boosted by a Fanon solid state amplifier. The noise source of the random noise generator is a gas-discharge tube with a transverse magnetic field applied. For any particular frequency that is observed on the wave analyzer, the random noise generator provides a Gaussian distribution, so long as the band-width used on the wave analyzer is narrow compared to the band selected on the random noise generator. The bands available are 20 KHz, 500 KHz and 5 MHz.
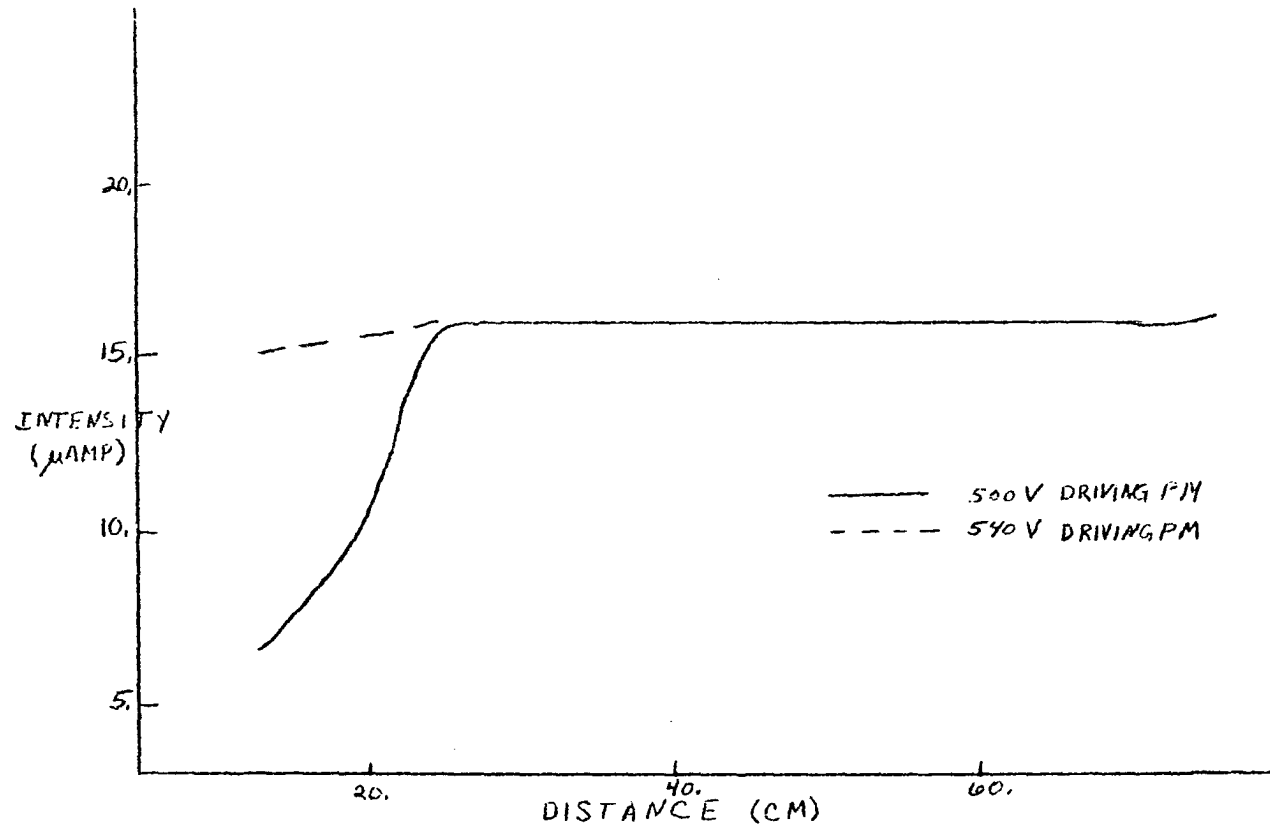
Figure 10.   Output of photomultiplier (PM) (intensity of light striking photosurface) as a function of position of the aperture screen.
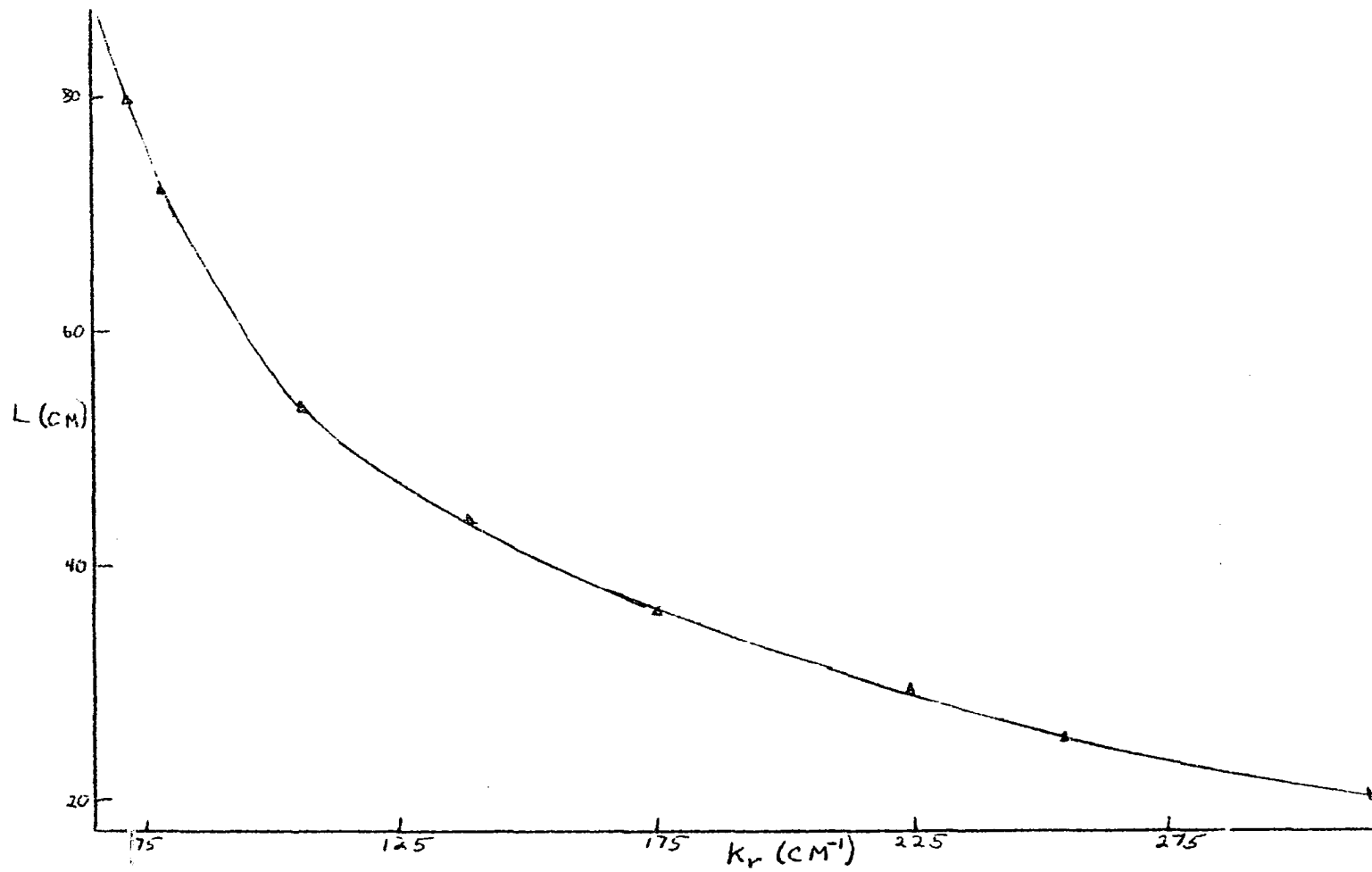
Figure 11. Wave number (k_r) versus position of aperture screen from interface (L).

Table I. The change in k_r and $\omega_r'/2\pi$ with L.

L (cm)	Δx (cm)	k_r (cm^{-1})	$\omega_r'/2\pi$ (Hz) [a]
20.0	.020	314.1	6868.
23.0	.024	261.8	5222.
24.0	.025	251.3	4912.
26.0	.026	241.6	4631.
28.0	.028	224.4	4144.
30.0	.030	209.4	3736.
32.0	.031	202.6	3557.
34.0	.035	179.5	2965.
36.0	.037	169.8	2728.
38.0	.039	161.1	2521.
40.0	.040	157.0	2427.
42.0	.042	149.6	2255.
44.0	.045	139.6	2034.
48.0	.050	125.6	1736.
50.0	.053	118.5	1591.
52.0	.055	114.2	1505.
54.0	.056	112.2	1465.
56.0	.060	104.7	1321.
58.0	.061	103.0	1288.
60.0	.065	96.6	1171.
62.0	.066	95.2	1145.
64.0	.069	91.0	1071.
66.0	.070	89.7	1048.
68.0	.071	88.5	1026.
72.0	.076	82.6	926.

(a) $\omega_r'/2\pi$ is calculated from the Kelvin equation using $\rho = 1.0$ gm/cc and $\gamma = 60.0$ dynes/cm.

The uniformity of the output throughout the region of interest can be seen in Figure 12. The variation in the signal level of the photo-current as a function of the output of the random noise generator for different voltages from the high voltage source is shown in Table II.

An L-shaped probe attached to a Utah SP25A microgap speaker is used as the electromechanical transducer which generates the ripples on the interface.

The response of this transducer as a function of frequency was characterized with the type of experimental set-up shown in Figure 13. If one defines L to be the length from the pivot to the mirror support and θ to be the angle between this plate and the mirror, one can algebraically find the relation between the displacement, x_4, of the light beam on the ceiling and the angle of rotation, β, of the mirror support, and thus the relation between x_4 and the displacement, x_D, of the probe on the transducer.

From Figure 14, with L and θ fixed,

$$x_2 = - L \cos\beta$$

$$y_2 = y_1 - L \sin\beta .$$

Then the equation of the mirror is:

$$(y - y_2) = (x - x_2) \tan(\pi - \theta + \beta)$$

$$= (x - x_2)[- \tan(\theta - \beta)].$$

At the photon impact point $y_3 = 0$, so x_3 is given by:

$$x_3 - x_2 = y_2 / \tan(\theta - \beta) \quad ;$$
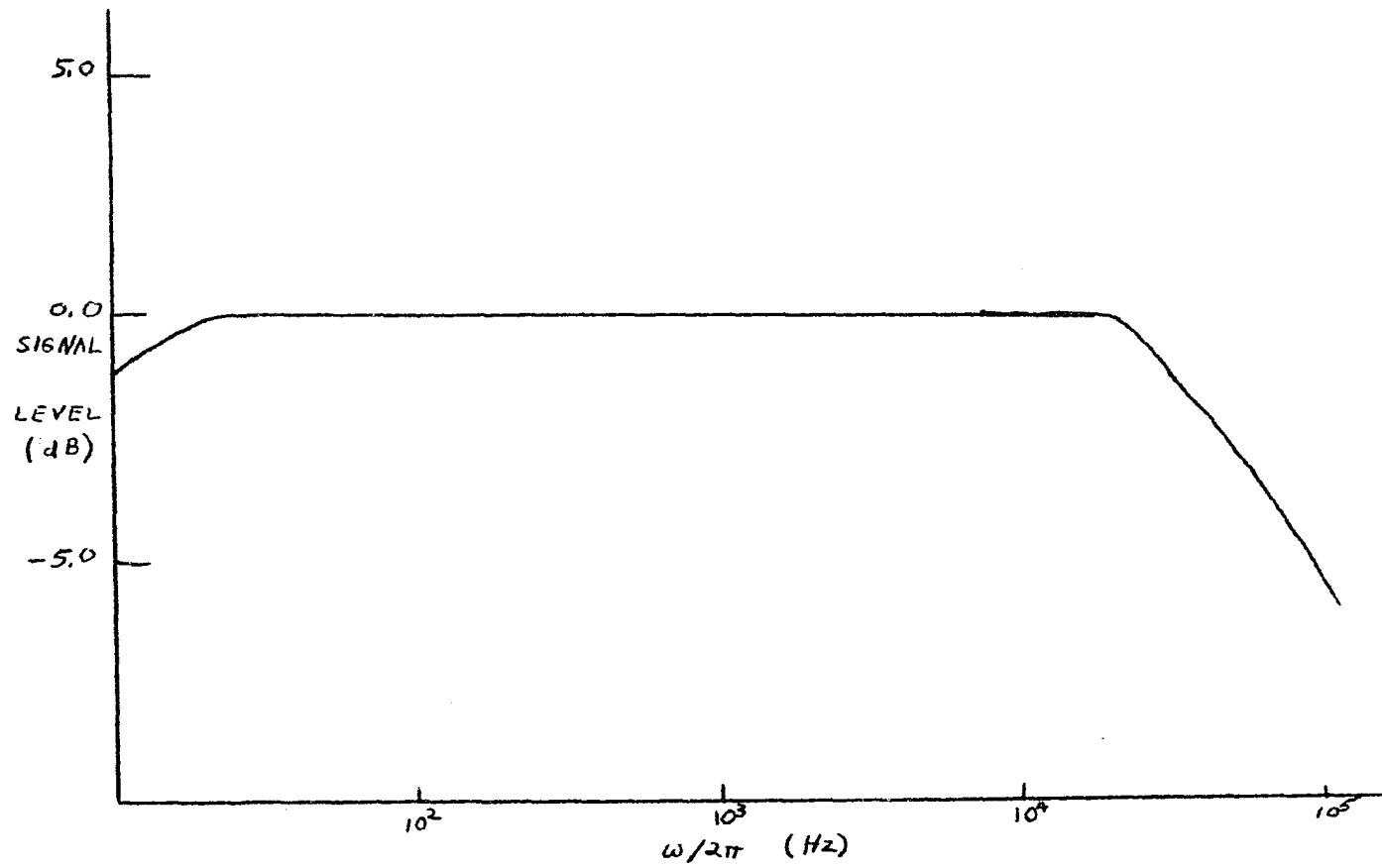
Figure 12. Signal level output of random noise generator as a function of frequency.

Table II. Response of photomultiplier for different input voltages.

Output of RNG

		.6 V	.8 V	1.0 V	1.2 V	1.5 V	
V o l t a g e	300 V	.2	.19	.18	.16	.15	Signal(S) $\mu\alpha$
		8.	8.	8.	8.	8.	Noise(N) $\mu\mu\alpha$
a t	350 V	.58	.58	.53	.50	.43	S
g e		24.	24.	24.	24.	24.	N
a t	400 V	1.3	1.5	1.4	1.3	1.2	S
		92.	92.	92.	92.	92.	N
H i g h	450 V	3.2	3.6	3.4	3.0	2.6	S
		172.	172.	172.	172.	172.	N
V o l t	500 V	7.8	8.2	7.6	7.0	6.0	S
		240.	240.	240.	240.	240.	N
a g e	550 V	17.0	19.0	18.0	16.0	15.0	S
		420.	420.	420.	420.	420.	N
S o u r c e	600 V	38.0	38.0	35.0	33.0	28.0	S
		1600.	1600.	1600.	1600.	1600.	N
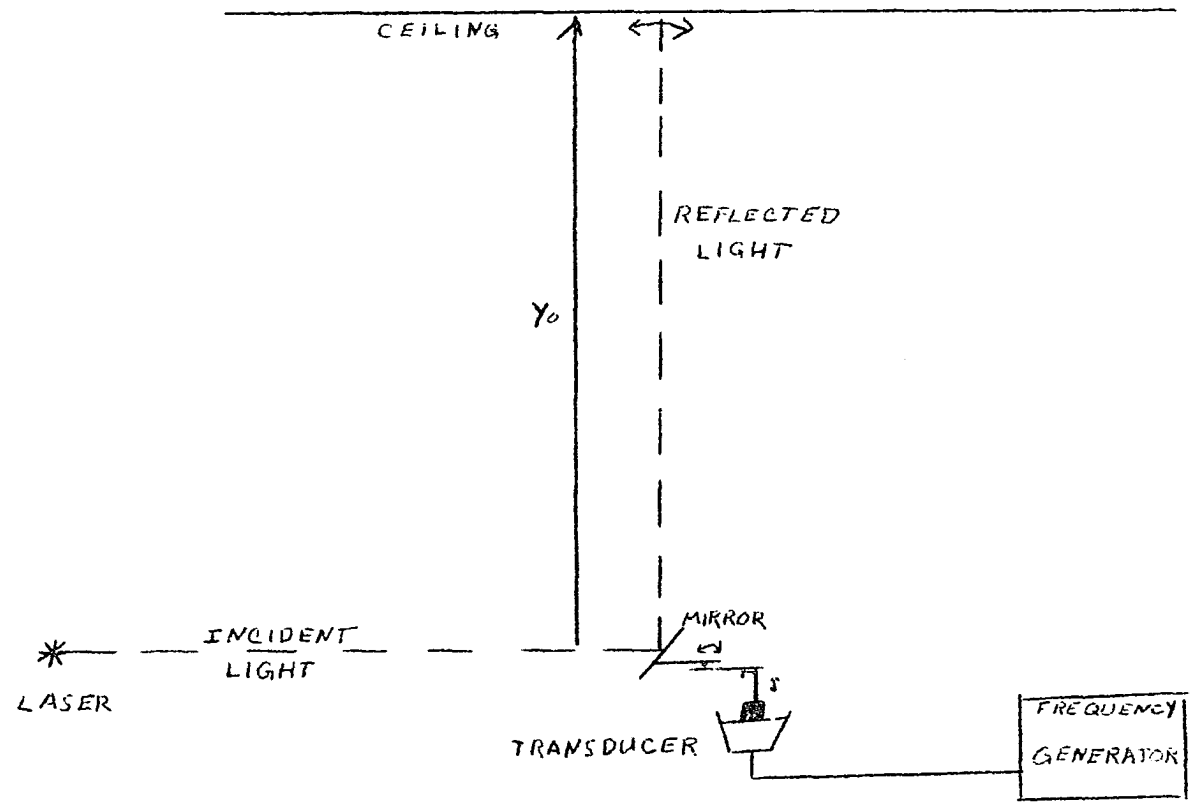
Figure 13.   Experimental set-up for determination of frequency dependence of transducer.
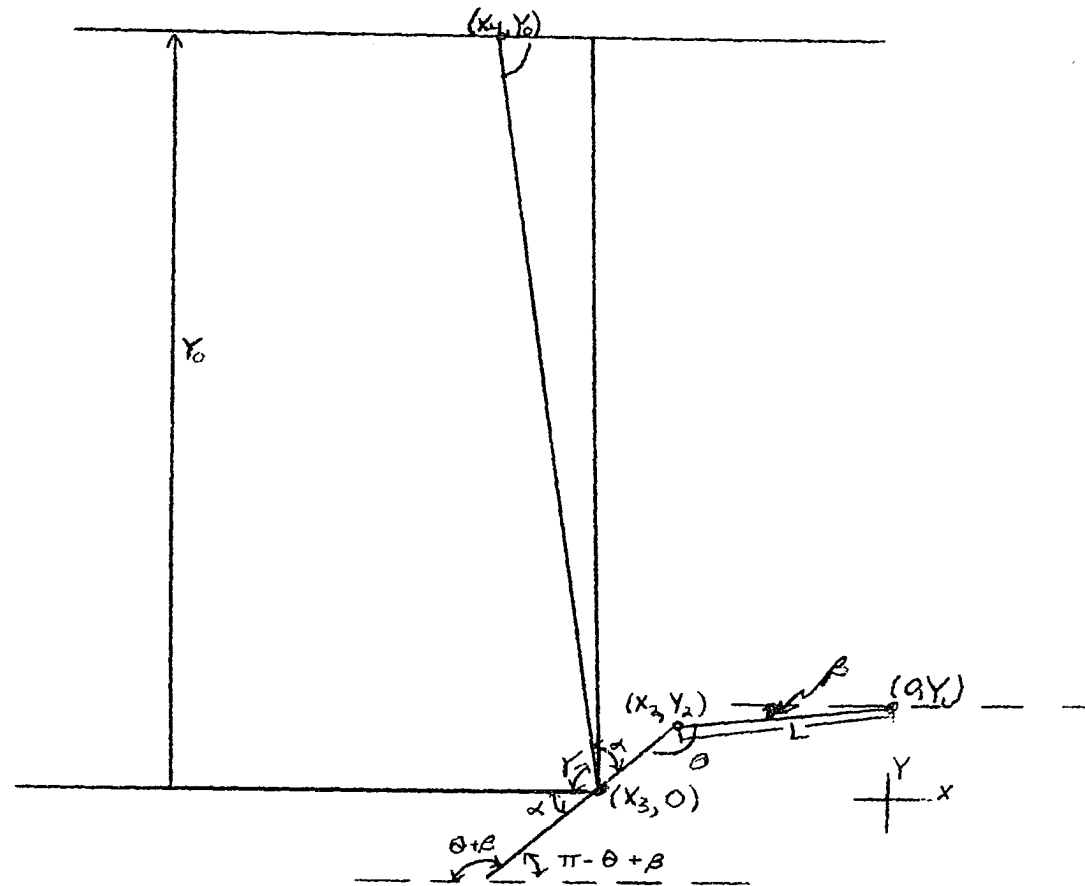
Figure 14. Mathematical assignation of experimental system in Figure 13.

so that $x_3 = -L\cos\beta - (y_1 - L\sin\beta)/\tan(\theta - \beta)$.

Now $\alpha = \pi - \theta + \beta$, $\gamma = \pi - 2\alpha = 2(\theta - \beta) - \pi$;

$$x_4 = x_3 - y_o\cot\gamma = x_3 - y_o\cot[2(\theta - \beta) - \pi]$$

$$= x_3 + y_o\cot[\pi - 2(\theta - \beta)]$$

$$= x_3 - y_o\cot 2(\theta - \beta)$$.

Therefore,

$$x_4 = -L\cos\beta - (y_1 - L\sin\beta)/\tan(\theta - \beta) - y_o\cot 2(\theta - \beta)$$.

where x_4 = the maximum displacement of reflected point on the ceiling;

y_o = the distance from the incident laser beam to the ceiling; and

y_1 = the distance from the incident laser beam to the plane of the

axis of rotation of the mirror support.

This equation is solved on the computer for β.

The displacement of the probe, x_D, can be expressed as $x_D = 2L\sin\beta$. The variation of x_D with frequency is shown in Table III.

The transducer assembly is positioned over a teflon trough so that the probe rests on the surface of the fluid filling the trough. The line of contact between the probe and interface is parallel to the ends of the trough. A random field of standing waves is generated by the probe arranged in this configuration. The fringe pattern from the aperture screen is rotated until it is parallel to the standing ripple field. The intensity of the power spectrum peaks are observed to depend strongly on this alignment, as one expects.

The variation of the photocurrent output of the photomultiplier with

Table III. Displacement of probe as a function of frequency.

a. Frequency generator at 0.5 Volts

Frequency (Hz)	X_4 (cm)	X_D (μ)
100.	9.50	.0539
200.	9.00	.0535
300.	7.00	.0517
400.	5.50	.0506
500.	2.00	.0493
600.	1.40	.0487
1000.	1.00	.0484
1500.	.70	.0481
20000.	.70	.0481

b. Frequency generator at 1.0 Volts

100.	18.00	.0565
200.	15.50	.0553
400.	10.00	.0547
500.	4.50	.0511
600.	3.50	.0499
1000.	1.60	.0489
1500.	1.60	.0489
20000.	1.60	.0489

changes in the vertical positioning of the probe with respect to the plane

of the interface is shown in Figure 15. One can see that no signal is

observed when the probe is more than 0.5 mm above or below the

interface.

The ripple amplitudes are kept below 0.1 micrometers throughout

the range from 400 Hz to 6000 Hz. This amplitude limit is required in

order to insure the validity of the linearity assumptions built into the

hydrodynamic theory.

D. The Photomultiplier

An RCA-1P21 high-vacuum photomultiplier is used to detect the

low level of light transmitted and scattered by the fluctuating interface.

This tube has a spectral response of the S-4 type which covers the range

from about 3000Å to 6200Å as shown in Figure 16. Maximum response

occurs at approximately 4000Å. Since the photocurrent produced at the

cathode is multiplied many times by secondary emission occurring in

each of the nine successive dynode stages, the 1P21 is capable of multi-

plying weak currents produced under weak illumination by an average

value of 2×10^6 times when operated at 100 volts per stage. The output

current of the 1P21 is a linear function of the exciting illumination under

normal operating conditions. A graph of the current to the laser versus

the output of the photomultiplier is shown in Figure 17.

Since secondary emission occurs almost instantaneously, frequency

response of the 1P21 is flat up to frequencies at which transit time and
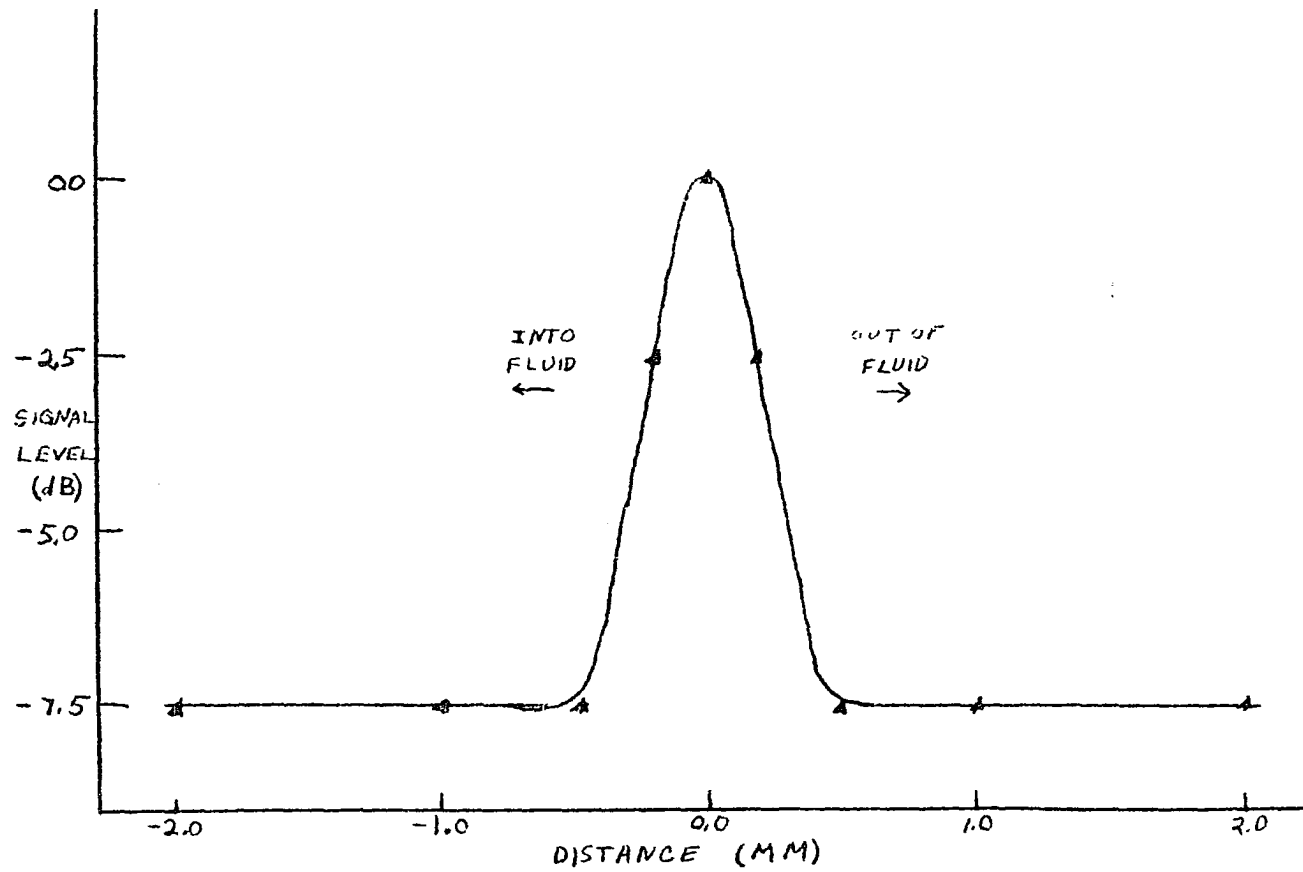
Figure 15. Strength of Brillouin peak intensity as a function of the probe's distance from the interface.
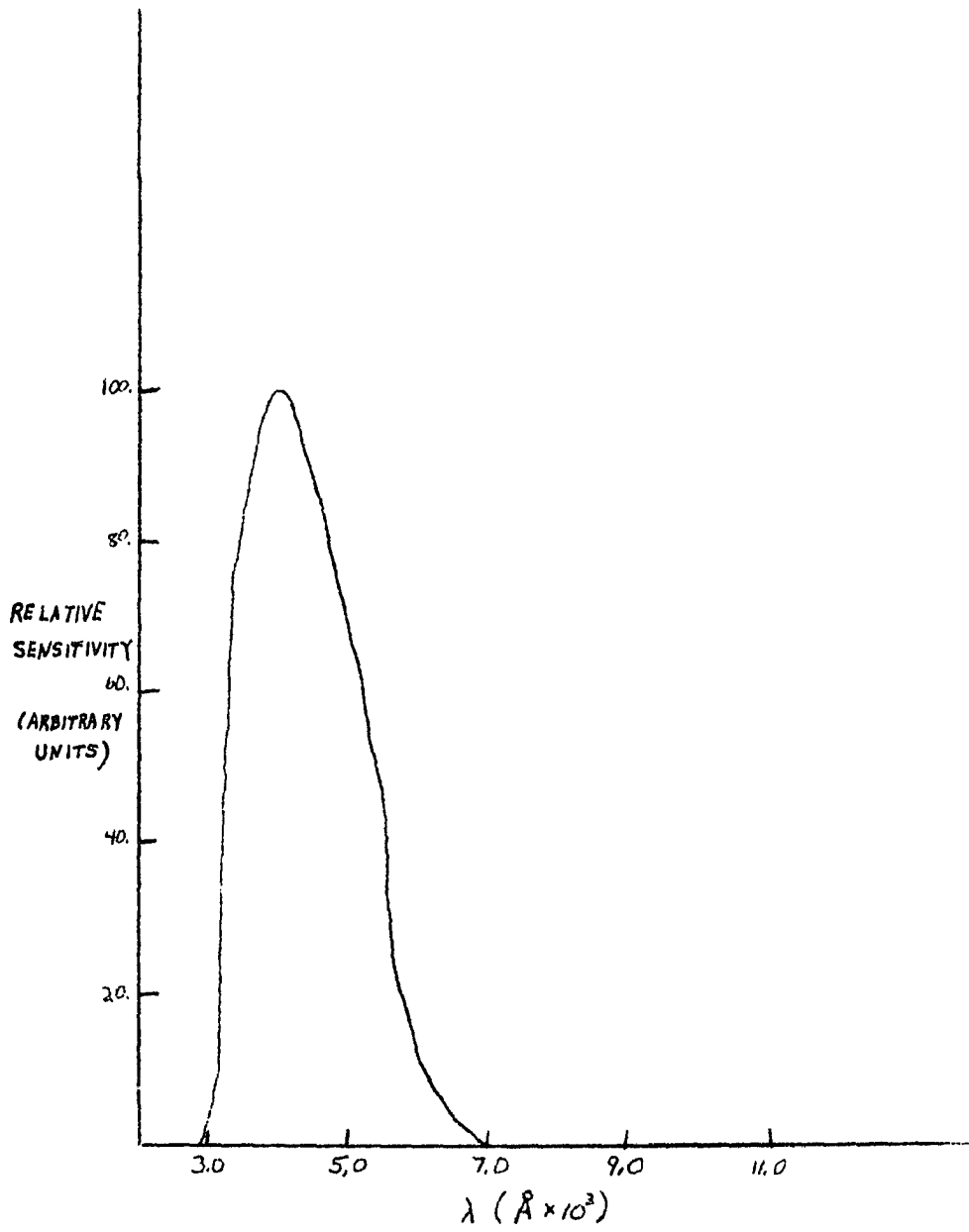
Figure 16. Spectral sensitivity characteristic of 1P21 type photomultiplier which has an S-4 response.
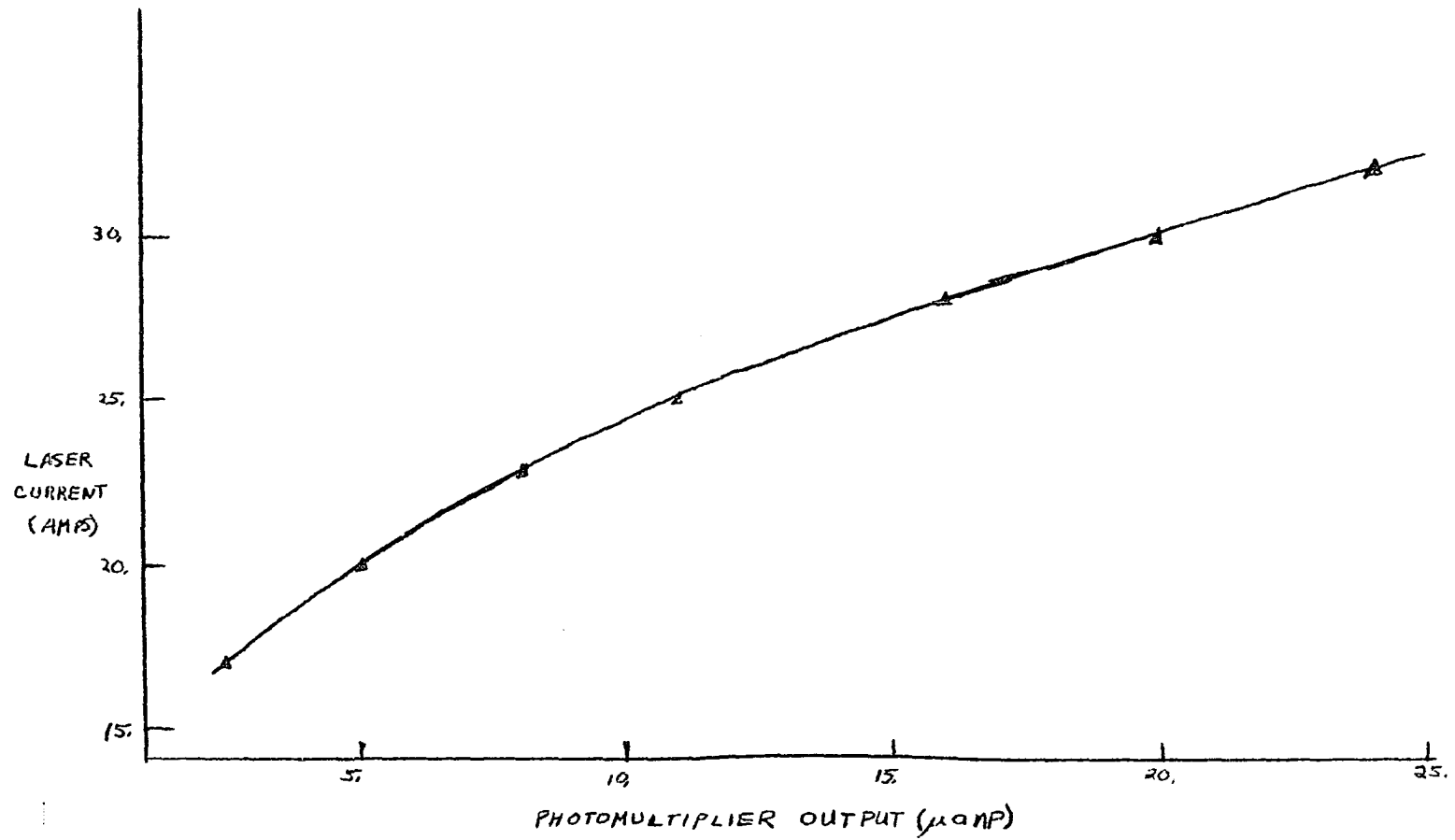
Figure 17. Current to laser versus output of photomultiplier.

capacitance effects become the limiting factor. This limiting frequency
is 1.15 MHz.

A Fluke Model 405B High Voltage Power Supply serves as a high
voltage source for the photomultiplier. The output of the photomultiplier
for different input voltages from the high voltage source is plotted in
Figure 18, for the cases of no laser light incident on the photomultiplier
and of laser light incident on the photomultiplier as during data collection.
From this graph one can see that the dark current is sufficiently low not
to interfere with signal detection. The data for light scattering from
interfacial fluctuations is taken with the input high voltage source at
500 volts.

E. Analyzer System

The output from the photomultiplier is handled according to the
schematic in Figure 19. It passes into a Hewlett-Packard Model 3590A
Wave Analyzer with a 3594A sweeping local oscillator which automatically
detects the signal amplitude for each frequency in the frequency range
scanned. A voltage-to-frequency converter mediates the output from the
wave analyzer to a RIDL Model 34-12 transistorized 400 channel pulse
height analyzer operating in the time mode. In this mode the RIDL
analyzer stores gross count information in one channel for a preset time.
At the end of this interval, the address will be advanced to the next
channel and the RIDL analyzer may again store gross count information
for the preset time. This operation will continue throughout the entire
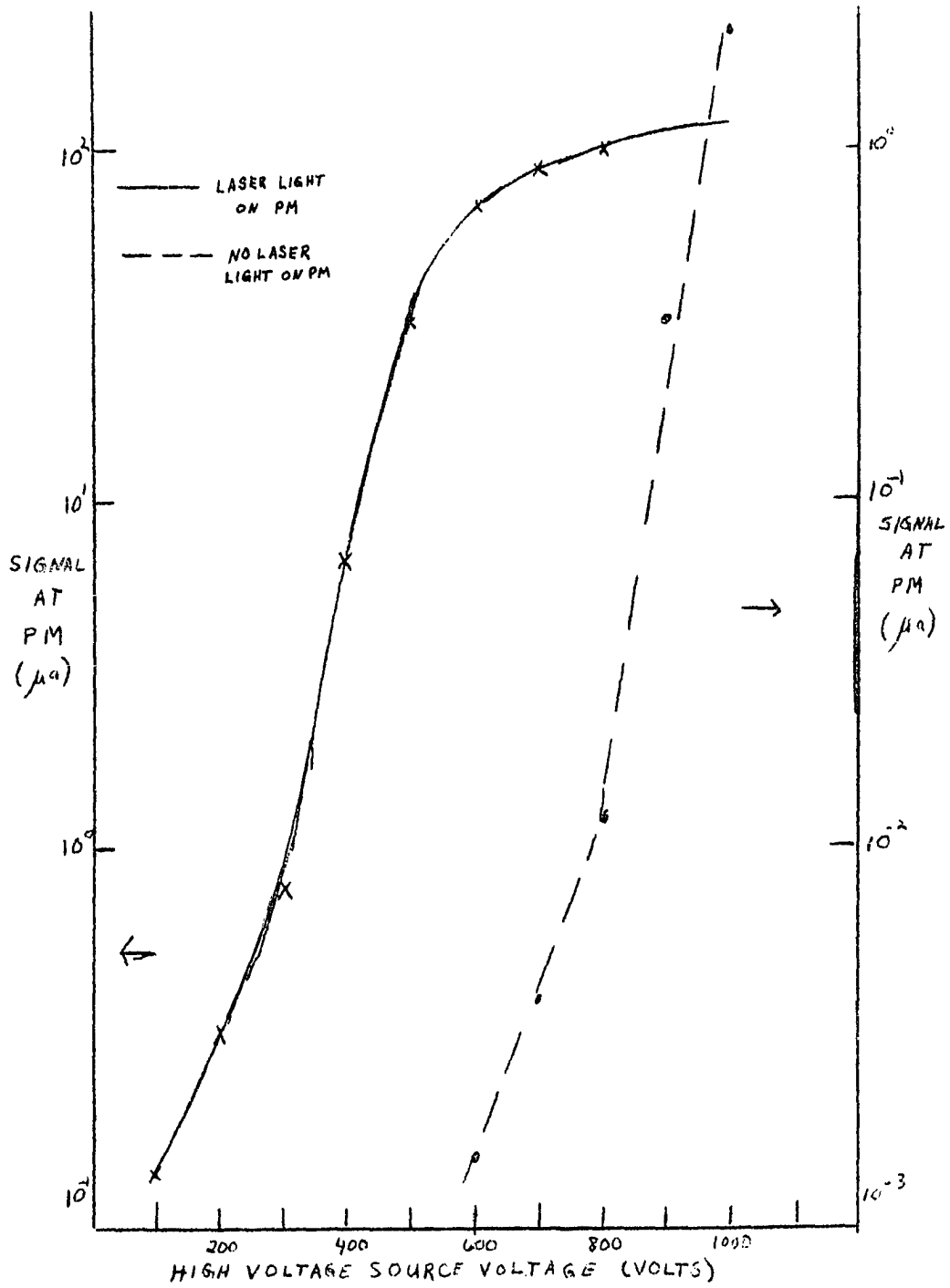
Figure 18. Output of photomultiplier as a function of voltage input from the high voltage source.
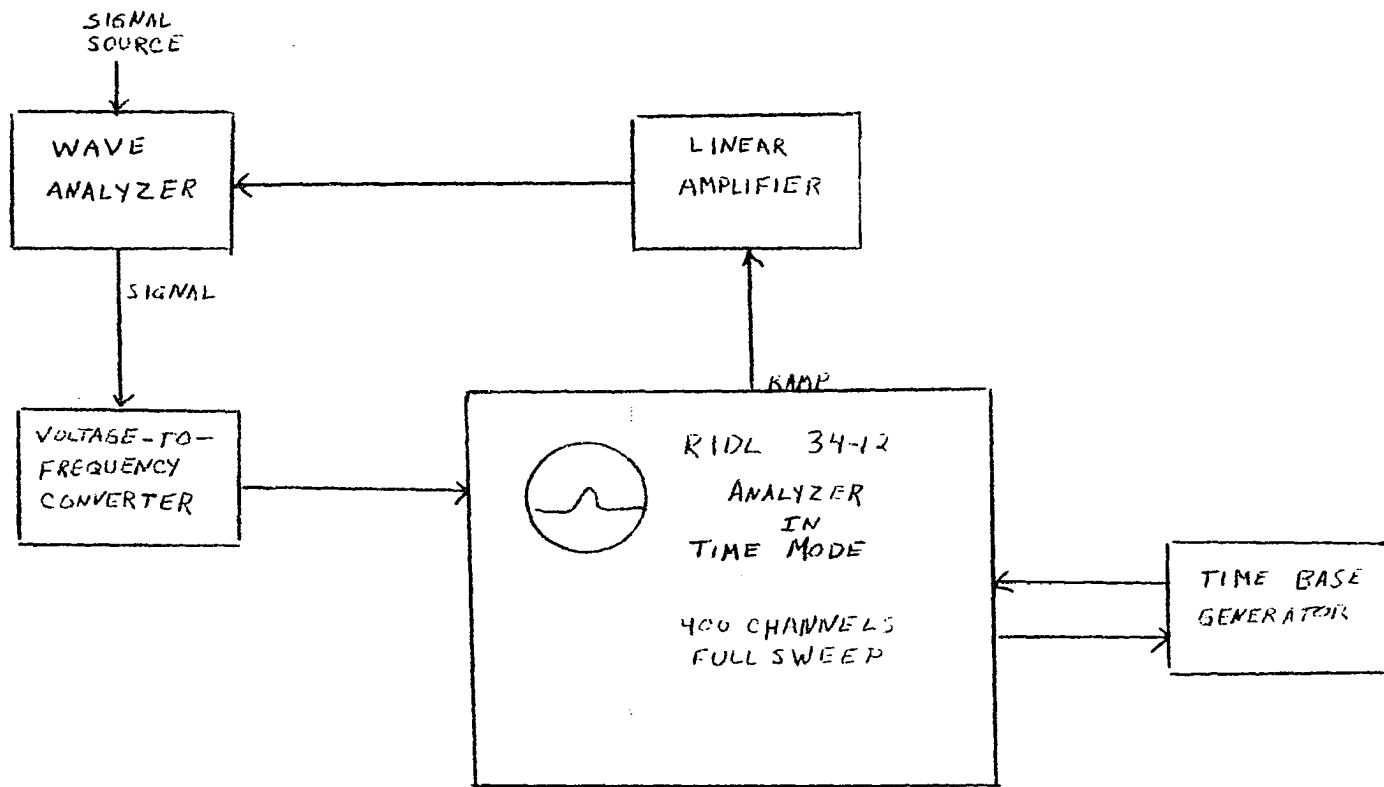
Figure 19. Schematic of data gathering analyzer system.

memory or preselected memory subgroup. The minimum cycle time

for the above operation is ten microseconds per channel. The time base

generator selects the length of time per channel and the dead time before

another scan is begun. A linear amplifier (Figure 20) is used to select

the frequency range to be scanned and to drive the local oscillator repeat

repeatedly through that range.

After enough scans are taken to establish the Brillouin peak and

its line shape, the scanning is stopped with the resultant signal counts

per channel being read out on an x-y recorder.

One should note that the signal grows as the number of scans, N,

and the noise grows as the square root of the number of scans because

of its random character. Thus the Signal/Noise grows as $N/\sqrt{N}$ or as $\sqrt{N}$.

A retardation plate could be placed in the path of the laser pencil

before the aperture screen in order to rotate the electric vector by 90°.

A laser line filter from Optics Corporation which selects out 4880Å

light waves to a precision of ±5Å (the half-width at half-height) is placed

on the photomultiplier housing in front of the photosurface. This limits

the observation range to $k_r < 10^5 cm^{-1}$, but this upper limit is well above

the range of interest in the present investigation.

The entire system is mounted on a ton-and-a-half slab of concrete

resting on Barrymount suspension springs to isolate the system from

extraneous sources of vibration.

The teflon trough was made of a single piece of milled teflon with
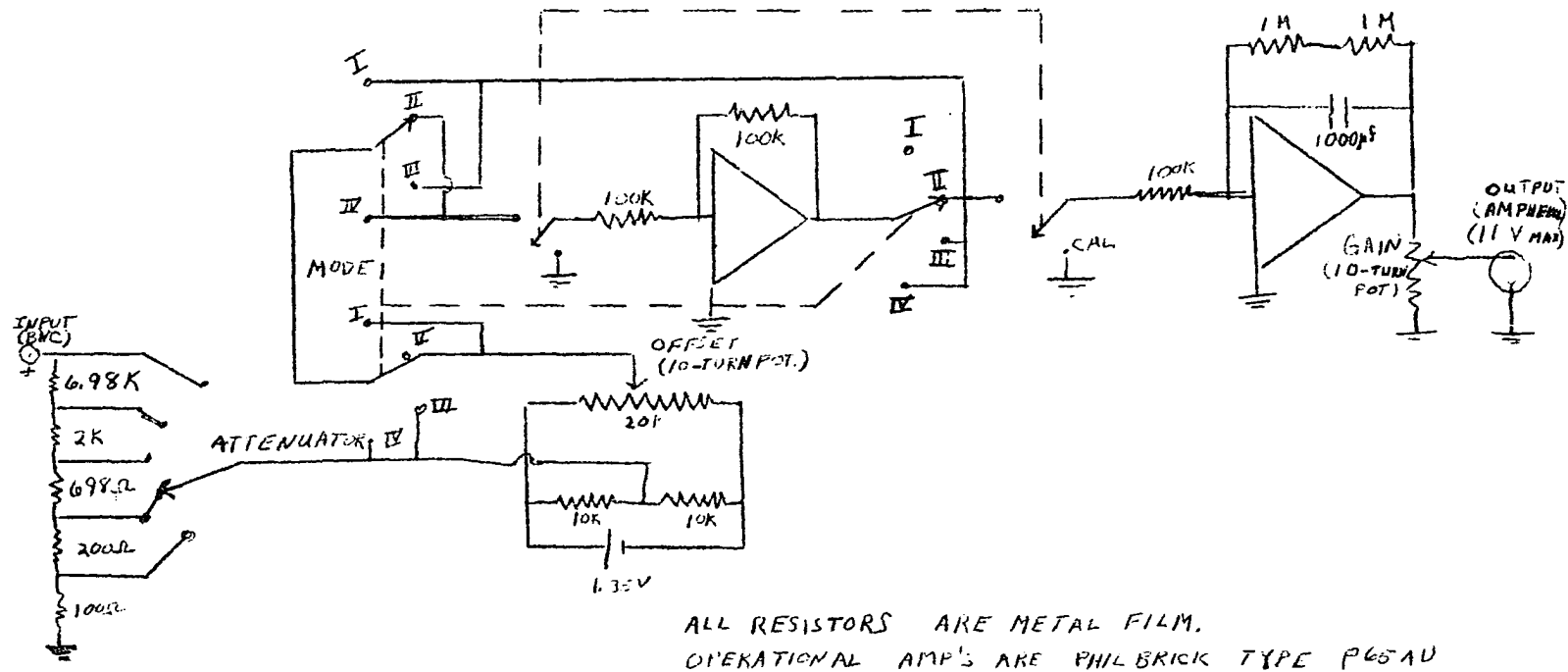
Figure 20. Circuit diagram of linear DC amplifier.

dimensions 8.0 cm x 5.0 cm x 2.0 cm and had a circular hole in the bottom in which was placed a precision fitted glass window.

F. Chemicals

The distilled water used in these experiments was obtained doubly distilled from a Barnstead distillation column and had a conductivity of 5.0×10^{-7} mho. The surface tension was 71.4 dynes/cm--that is, 0.5 dynes/cm lower than the literature value at 25°C. It was found that sufficient contamination to justify discontinuing the experiment accumulates after four hours of use.

The chloroform used as solvent for the fatty acids was distilled on a 30-plate Oldershaw distillation column.

All of the fatty acids used were obtained from Eastman Chemical and were recrystallized twice from methanol or ethanol prior to use.

The heptanoic acid was obtained from Eastman Chemical and was used as delivered.

The synthetic polymers were used as received from Dr. James Anderson of Case-Western Reserve University.

All the glassware and the teflon trough were cleaned in an alcoholic KOH solution and an acid permanganate solution to insure their freedom from contamination.

G. Experimental Procedure

The experiment is performed as follows:

1. After the electronic components have stabilized (about fifteen minutes), the teflon trough is filled with the distilled water.

2. Impurities on the surface are siphoned off by a capillary tube hooked to a vacuum filtering flask and the chloroform solution of the mono-layer material is placed on the surface with a syringe.

3. For a particular aperture position, the wave analyzer is driven through the complete 700Hz to 7KHz frequency range for sixteen to twenty-four scans.

4. The frequency range for the scan is narrowed to that portion where the Brillouin peak is located.

5. This new frequency range is now scanned for approximately sixteen times, and the resulting spectrum is recorded on the x-y recorder.

6. The aperture screen is moved to a new position.

Steps 3 through 6 are repeated until at least ten spectra are taken for that particular concentration of that monomolecular film.

RESULTS

The experimental method just described has been used to study the air-water and the air-heptanoic acid solution interfaces. Monolayers of four long chain fatty acids and of two synthetic polymers at the air-water interface were also studied. The results obtained are compared with the theoretical results generated by the program described in the theory section.

The program used the surface tension values for the fatty acids experimentally determined by J. Ahmad of this laboratory by the film balance method. Using these values and the equation of state for liquid-expanded monolayers (56),

$$(\pi - \pi_0) \ (a - a_0) = kT \ ,$$

approximate values were derived for the shear viscosity and the elastic modulus according to the equations (57):

$$\log \eta = \log \eta_0 + b\pi \ ,$$

and
$$\epsilon = (\pi - \pi_0) \ / \ (1 - a/a_0) \ ,$$

where π is the spreading pressure of the monolayer; π_0 is the spreading coefficient for the hydrocarbon part of the film molecules on water; a_0 is the area correction allowing for the finite size of polar groups; a is the area per film molecule; k is Boltzmann's constant; η is the shear viscosity of the lower phase; and b is an empirically determined constant. Values for π_0 and a_0 were obtained from the early work of Langmuir (58). Values for b were obtained from the work of Harkins (59).

The non-rationalized polynomial program usually yields three

distinct roots. Two are analogs of the pure interface pair of roots, and

the third goes to zero for low values of Γ, the surface excess. The

rationalized polynomial yields seven distinct roots, but these include

two pairs of complex conjugates and three which go to zero in the same

manner as the non-rationalized polynomial program. There is a ten per

cent difference in the corresponding roots for the two programs, with the

rationalized polynomial requiring almost twice as many iterations before

convergence.

Two dimensionless groups of parameters, Y_1 and Y_3, are routinely

calculated for both theoretical and experimental values.

$$Y_1 = \frac{\rho \omega_r'^2}{\gamma k_r^3} - \frac{\rho g}{\gamma k_r} \quad .$$

$$Y_3 = \frac{\omega_r'}{\omega_r''} \quad .$$

Plots are made of $\omega_r'^{-2/3}$ versus L which are designed to produce a

linear relationship with aperture displacement from an arbitrary point

on the optical axis. The least squares deviation of the points from the

functional line $\omega_r'^{-2/3} = a + bL$ are calculated.

The experimental and theoretical results for the air-water interface

are now in press (60). They are depicted in Figure 21, which shows the

$\omega_r'^{-2/3}$ versus L plot for two different sets of apertures. The observed

slopes are $4.93 \times 10^{-5} (\text{sec})^{2/3} \text{cm}^{-1}$ and $4.72 \times 10^{-5} (\text{sec})^{2/3} \text{cm}^{-1}$ and the
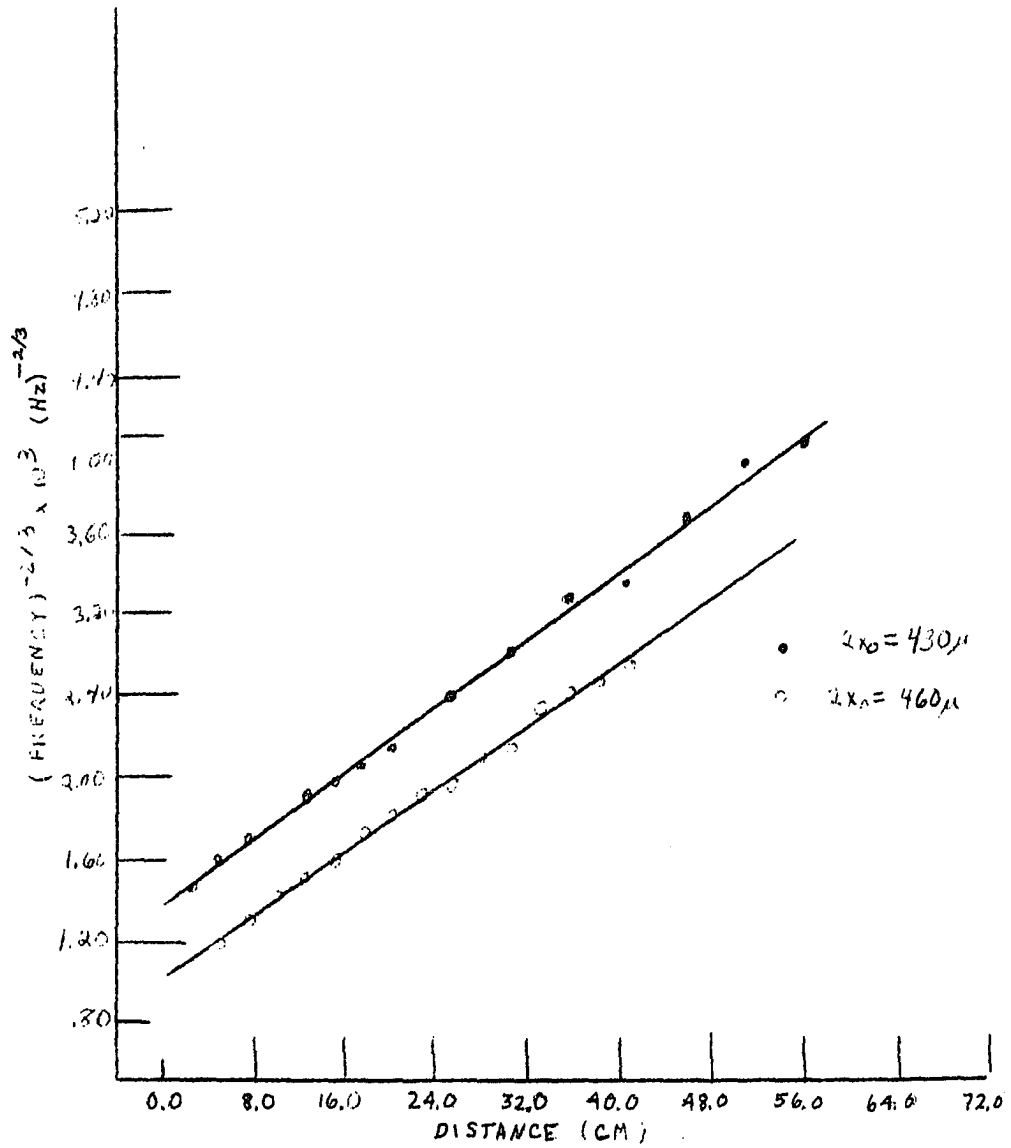
Figure 21. Plot of $\omega^{-2/3}$ versus L for the air-water system for two different values of $2x_0$.

theoretical slope turns out to be $4.20 \times 10^{-5} (\text{sec})^{2/3} \text{cm}^{-1}$. The two data

sets are displaced from each other since $2x_0$ has been changed without

changing L.

The air-heptanoic acid interface was studied at six different concen-

trations. Only values for ω_r' and not ω_r'' were obtained at the time this

series of experiments was done.

For a concentration of 7.5×10^{-3} moles/liter, $\gamma = 37.8$ dynes/cm,

and the slope of the plot is $5.23 \times 10^{-4} (\text{sec})^{2/3} \text{cm}^{-1}$ experimentally and

$5.35 \times 10^{-4} (\text{sec})^{2/3} \text{cm}^{-1}$ theoretically. The deviation of the points from

this line is 0.9%. The values obtained for ω_r' and Y_1 are recorded in

Table IV.

The values of the slopes for the other concentrations are recorded

along with the surface tensions in Table XVI. The values for ω_r' and for

Y_1 for these concentrations are listed in Table V through Table IX.

Figure 22 illustrates the linear dependence of $\omega_r^{-2/3}$ on L at three

different concentrations of heptanoic acid.

Myristic acid was used as a monolayer on the air-water interface

at six different concentrations. The concentrations, surface tensions,

and slopes for the plot of $\omega_r'^{-2/3}$ versus L are given in Table XVII. The

values for ω_r', ω_r'', Y_1, and Y_3 are listed in Table X through

Table XV.

Table IV. Air-Heptanoic Acid (7.48×10^{-3} m/l) Interface.

$k_r(cm^{-1})$	$\omega'_{r_{exp}}$ (Hz)	$\omega'_{r_{th}}$ (Hz)	$Y_{1_{exp}}$	$Y_{1_{th}}$
185.0	16110.	14327.	1.0781	.8536
172.2	14074.	12888.	1.0198	.8564
161.1	12309.	11681.	.9528	.8590
151.3	11310.	10647.	.9705	.8614
142.7	10002.	9765.	.9057	.8636
134.9	9519.	8987.	.9691	.8657
128.0	8570.	8317.	.9200	.8676
121.8	8030.	7729.	.9382	.8695
110.9	6805.	6730.	.8906	.8729
101.9	5988.	5939.	.8902	.8760
94.2	5334.	5288.	.8938	.8789
87.6	4731.	4751.	.8742	.8815
81.8	4373.	4294.	.9152	.8839
79.2	4291.	4094.	.9709	.8850
76.8	3977.	3912.	.9155	.8861

Table V.   Air- Heptanoic Acid $(3.75 \times 10^{-3} \text{ m/l})$ Interface.

k_r (cm^{-1})	$\omega'_{r_{exp}}$ (Hz)	$\omega'_{r_{th}}$ (Hz)	$Y_{1_{exp}}$	$Y_{1_{th}}$
185.0	20804.	16312.	1.4017	.8626
172.2	17492.	14672.	1.2281	.8652
161.1	15381.	13296.	1.1600	.8676
151.3	13861.	12118.	1.1365	.8699
142.7	12566.	11113.	1.1146	.8720
134.9	11090.	10227.	1.0255	.8740
128.0	9921.	9464.	.9612	.8759
121.8	9205.	8794.	.9614	.8777
110.9	7986.	7656.	.9567	.8810
101.9	7018.	6755.	.9539	.8839
94.2	6472.	6015.	1.0263	.8867
87.6	5724.	5402.	.9985	.8892
81.8	5234.	4882.	1.0230	.8915
79.2	4914.	4655.	.9930	.8926
76.8	4612.	4448.	.9606	.8937

Table VI.   Air-Heptanoic Acid (2.5×10^{-3} m/l) Interface.

k_r (cm^{-1})	$\omega'_{r_{exp}}$ (Hz)	$\omega'_{r_{th}}$ (Hz)	$Y_{1_{exp}}$	$Y_{1_{th}}$
185.0	20609.	17081.	1.2587	.8656
172.2	17624.	15363.	1.1408	.8682
161.1	16028.	13922.	1.1528	.8706
151.3	14432.	12688.	1.1276	.8728
142.7	12799.	11636.	1.0581	.8749
134.9	11655.	10708.	1.0367	.8769
128.0	9959.	9908.	.8862	.8787
121.8	8903.	9207.	.8229	.8805
110.9	7200.	8015.	.7114	.8837
101.9	6321.	7072.	.7077	.8866
94.2	6032.	6296.	.8156	.8893
87.6	5228.	5655.	.7617	.8918
81.8	4706.	5110.	.7563	.8941
79.2	4430.	4872.	.7380	.8952
76.8	4197.	4656.	.7275	.8963

Table VII. Air-Heptanoic Acid (7.988×10^{-6} m/l) Interface.

k_r (cm^{-1})	$\omega'_{r_{exp}}$ (Hz)	$\omega'_{r_{th}}$ (Hz)	$Y_{1_{exp}}$	$Y_{1_{th}}$
185.0	21111.	19320.	1.0575	.8734
172.2	17907.	17375.	.9429	.8759
161.1	16148.	15743.	.9368	.8782
151.3	14357.	14347.	.8934	.8803
142.7	12679.	13157.	.8314	.8823
134.9	11712.	12106.	.8381	.8842
128.0	10279.	11201.	.7560	.8860
121.8	9896.	10407.	.8142	.8876
116.1	8966.	9694.	.7709	.8892
110.9	8482.	9059.	.7908	.8908
106.2	7929.	8497.	.7874	.8922
101.9	7464.	7992.	.7907	.8936
97.9	6930.	7532.	.7684	.8949
94.2	6597.	7115.	.7815	.8962
90.8	6158.	6738.	.7606	.8974
87.6	5969.	6390.	.7956	.8985
84.6	5341.	6068.	.7060	.8997

Table VIII. Air-Heptanoic Acid (7.988×10^{-7} m/l) Interface.

k_r (cm^{-1})	$\omega'_{r_{exp}}$ (Hz)	$\omega'_{r_{th}}$ (Hz)	$Y_{l_{exp}}$	$Y_{l_{th}}$
185.0	22745.	19170.	1.1916	.8729
172.2	20609.	17240.	1.2125	.8754
161.1	17404.	15622.	1.0564	.8777
151.3	15457.	14236.	1.0052	.8798
142.7	14307.	13055.	1.0276	.8818
134.9	12830.	12013.	.9764	.8838
128.0	11498.	11115.	.9184	.8855
121.8	10763.	10327.	.9350	.8872
116.1	10172.	9620.	.9636	.8888
110.9	9110.	8989.	.8858	.8903
106.2	8501.	8431.	.8787	.8917
101.9	7892.	7930.	.8580	.8931
97.9	7320.	7475.	.8322	.8945
94.2	6981.	7060.	.8494	.8957
90.8	6503.	6687.	.8237	.8969
87.6	6308.	6341.	.8628	.8981
84.6	6057.	6022.	.8821	.8992
81.8	5793.	5729.	.8917	.9003
79.2	5536.	5462.	.8969	.9014
76.8	5278.	5219.	.8954	.9024
74.5	4869.	4989.	.8344	.9034
72.3	4467.	4773.	.7667	.9044
70.3	4335.	4579.	.7867	.9053
68.4	4260.	4397.	.8256	.9062
66.5	4071.	4218.	.8177	.9071
64.8	3914.	4059.	.8178	.9080

Table IX. Air-Heptanoic Acid (7.988×10^{-8} m/l) Interface.

k_r (cm^{-1})	$\omega'_{r_{exp}}$ (Hz)	$\omega'_{r_{th}}$ (Hz)	$Y_{1_{exp}}$	$Y_{1_{th}}$
185.0	18755.	19512.	.8065	.8741
172.2	16129.	17548.	.7392	.8765
161.1	14250.	15900.	.7049	.8788
151.3	12604.	14490.	.6653	.8809
142.7	11643.	13287.	.6773	.8829
134.9	10399.	12227.	.6383	.8848
128.0	9519.	11312.	.6264	.8865
121.8	8482.	10511.	.5778	.8882
116.1	8218.	9791.	.6258	.8898
110.9	7420.	9149.	.5846	.8913
106.2	7025.	8581.	.5969.	.8927
101.9	6736.	8072.	.6219	.8941
97.9	6421.	7607.	.6373	.8954
94.2	5938.	7186.	.6114	.8966
90.8	5422.	6805.	.5697	.8978
87.6	5190.	6453.	.5808	.8991
84.6	4800.	6129.	.5509	.9002
81.8	4712.	5831.	.5868	.9013
79.2	4398.	5559.	.5629	.9023
76.8	4310.	5312.	.5938	.9034
74.5	3782.	5078.	.5465	.9044
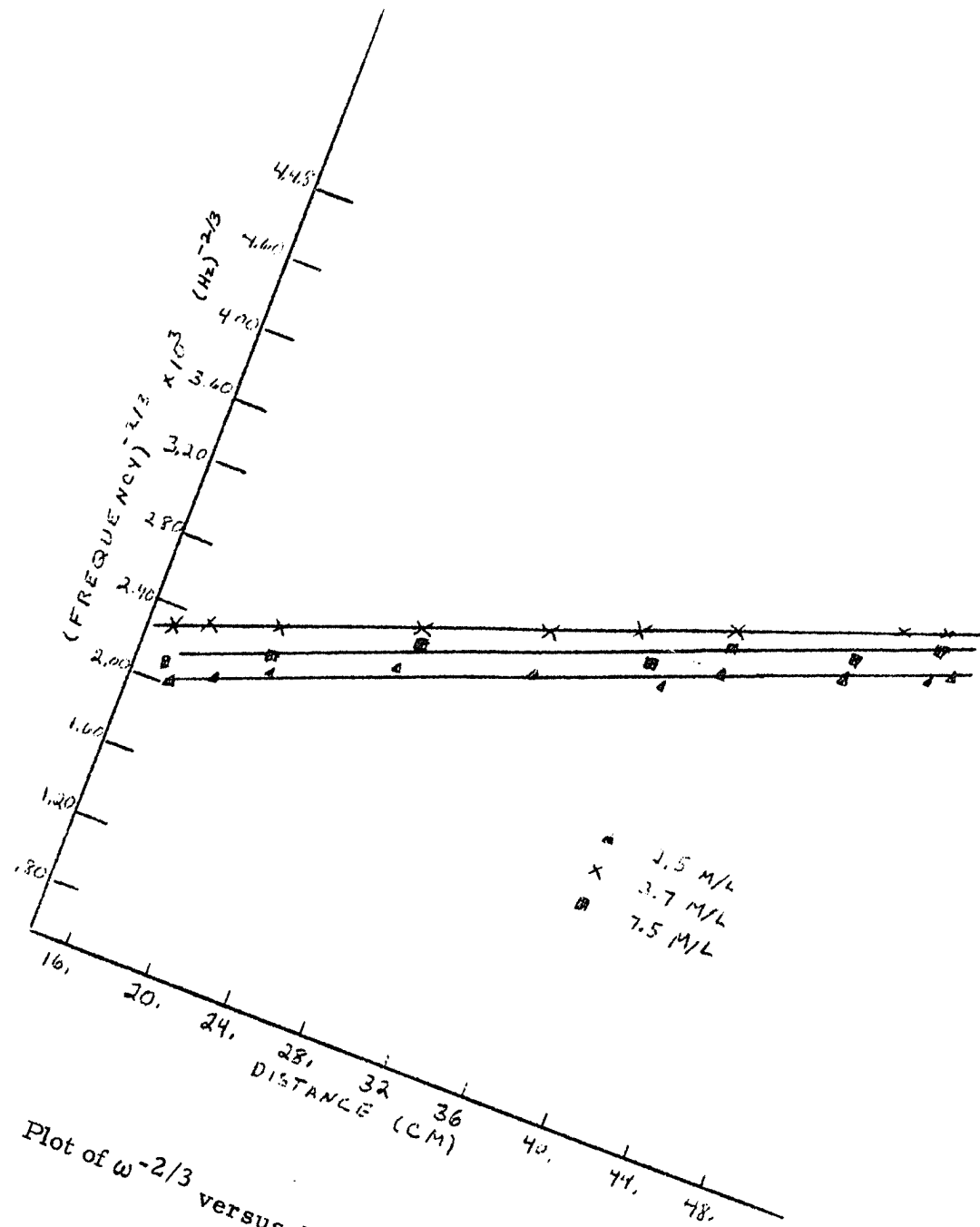
Figure 22. Plot of $\omega^{-2/3}$ versus L' for the air-heptanoic acid interface.

Table X.   Myristic Acid (4.72μl) at Air-Water Interface.

k_r (cm^{-1})	$\omega'_{r_{exp}}$ (Hz)	$\omega'_{r_{th}}$ (Hz)	$Y_{1_{exp}}$	$Y_{1_{th}}$
87.1	5073.	6441.	.5727	.9279
90.9	5523.	6863.	.5984	.9271
95.0	5944.	7329.	.6076	.9262
99.4	6114.	7839.	.5599	.9253
104.4	6496.	8433.	.5304	.9243
109.8	7219.	9090.	.5806	.9233
115.8	7779.	9839.	.5744	.9222
122.5	8656.	10698.	.6007	.9210
130.1	9285.	11700.	.5777	.9198

k_r (cm^{-1})	$\omega''_{r_{exp}}$ (Hz)	$\omega''_{r_{th}}$ (Hz)	$Y_{3_{exp}}$	$Y_{3_{th}}$
87.1	363.2	307.1	13.97	20.98
90.9	706.9	331.5	7.81	20.70
95.0	829.4	358.8	7.16	20.42
99.4	884.7	389.2	6.91	20.14
104.4	821.8	425.1	7.78	19.84
109.8	995.2	465.4	7.25	19.53
115.8	1231.5	512.2	6.32	19.21
122.5	1339.6	566.7	6.46	18.88
130.1	1190.7	631.5	7.80	18.53

Table XI. Myristic Acid (6.14μl) at Air-Water Interface.

k_r (cm^{-1})	$\omega'_{r_{exp}}$ (Hz)	$\omega'_{r_{th}}$ (Hz)	$Y_{1_{exp}}$	$Y_{1_{th}}$
83.6	4863.	5708.	.6695	.9269
87.1	4930.	6067.	.6095	.9261
90.9	5388.	6465.	.6417	.9253
95.0	5894.	6903.	.6731	.9245
99.4	6151.	7385.	.6388	.9237
104.4	6365.	7944.	.5918	.9227
109.8	7511.	8563.	.7083	.9217
115.8	7710.	9269.	.6358	.9207
130.1	8295.	10078.	.5195	.9196

k_r (cm^{-1})	$\omega''_{r_{exp}}$ (Hz)	$\omega''_{r_{th}}$ (Hz)	$Y_{3_{exp}}$	$Y_{3_{th}}$
83.6	589.4	254.2	8.25	22.45
87.1	547.3	273.4	9.01	22.19
90.9	613.9	295.0	8.78	21.91
95.0	814.9	319.1	7.23	21.63
99.4	1036.7	345.9	5.93	21.35
104.4	841.9	377.5	7.56	21.04
109.8	1149.8	413.0	6.53	20.73
115.8	1310.7	454.1	5.88	20.41
130.1	1493.5	502.0	5.55	20.08

71

Table XII. Myristic Acid (6.99μl) at Air-Water Interface.

k_r (cm^{-1})	$\omega'_{r_{exp}}$ (Hz)	$\omega'_{r_{th}}$ (Hz)	$Y_{1_{exp}}$	$Y_{1_{th}}$
83.6	4675.	5470.	.6735	.9267
87.1	5096.	5814.	.7094	.9260
90.9	5524.	6195.	.7348	.9252
95.0	5902.	6615.	.7352	.9244
99.4	6032.	7076.	.6689	.9236
104.4	6631.	7612.	.6996	.9226
109.8	7204.	8206.	.7096	.9217
115.8	7812.	8882.	.7111	.9206
122.5	8319.	9657.	.6808	.9196

k_r (cm^{-1})	$\omega''_{r_{exp}}$ (Hz)	$\omega''_{r_{th}}$ (Hz)	$Y_{3_{exp}}$	$Y_{3_{th}}$
83.6	555.4	228.1	8.42	23.98
87.1	696.2	245.2	7.32	23.71
90.9	863.3	264.4	6.40	23.43
95.0	1067.5	285.9	5.52	23.14
99.4	1178.1	309.7	5.12	22.85
104.4	1354.0	337.7	4.90	22.54
109.8	1076.3	369.2	6.69	22.22
115.8	1076.3	405.6	7.26	21.90
122.5	1438.8	448.1	5.78	21.55

Table XIII. Myristic Acid (8.00μl) at Air-Water Interface.

k_r (cm^{-1})	$\omega'_{r_{exp}}$ (Hz)	$\omega'_{r_{th}}$ (Hz)	$Y_{1_{exp}}$	$Y_{1_{th}}$
83.6	4549.	5093.	.7337	.9241
87.1	4970.	5413.	.7761	.9234
90.9	5463.	5768.	.8268	.9226
95.0	5916.	6159.	.8501	.9217
99.4	6116.	6588.	.7913	.9209
104.4	6440.	7087.	.7592	.9199
109.8	7091.	7639.	.7908	.9189
115.8	7970.	8268.	.8516	.9179
122.5	8727.	8990.	.8623	.9167
130.1	9035.	9832.	.7725	.9155

k_r (cm^{-1})	$\omega''_{r_{exp}}$ (Hz)	$\omega''_{r_{th}}$ (Hz)	$Y_{3_{exp}}$	$Y_{3_{th}}$
83.6	414.7	220.8	10.97	23.06
87.1	571.8	237.4	8.69	22.80
90.9	650.9	256.0	8.40	22.53
95.0	759.6	276.8	7.79	22.25
99.4	909.3	299.8	6.72	21.97
104.4	829.4	327.0	7.76	21.67
109.8	912.3	357.5	7.77	21.37
115.8	1102.7	392.8	7.23	21.05
122.5	1147.3	433.8	7.61	20.72
130.1	1192.5	482.6	7.58	20.37

Table XIV. Myristic Acid (8.90μl) at Air-Water Interface.

k_r (cm^{-1})	$\omega'_{r_{exp}}$ (Hz)	$\omega'_{r_{th}}$ (Hz)	$Y_{1_{exp}}$	$Y_{1_{th}}$
83.6	4842.	4950.	.8777	.9231
87.1	5205.	5261.	.8985	.9223
90.9	5182.	5606.	.7848	.9215
95.0	5762.	5986.	.8506	.9206
99.4	6189.	6403.	.8551	.9198
104.4	6597.	6888.	.8409	.9188
109.8	7420.	7424.	.9141	.9178
115.8	7868.	8036.	.8756	.9167
122.5	8397.	8737.	.8422	.9156
130.1	9282.	9555.	.8604	.9143

k_r (cm^{-1})	$\omega''_{r_{exp}}$ (Hz)	$\omega''_{r_{th}}$ (Hz)	$Y_{3_{exp}}$	$Y_{3_{th}}$
83.6	536.0	218.0	9.03	22.71
87.1	627.0	234.4	8.30	22.45
90.9	671.0	252.7	7.72	22.18
95.0	912.3	273.2	6.32	21.91
99.4	1026.0	296.0	6.03	21.63
104.4	1067.5	322.8	6.18	21.33
109.8	1317.0	352.9	5.63	21.03
115.8	1012.8	387.8	7.77	20.72
122.5	1685.8	428.3	4.98	20.40
130.1	1831.5	476.5	5.07	20.05

Table XV. Myristic Acid (9.8μl) at Air-Water Interface.

k_r (cm^{-1})	$\omega'_{r_{exp}}$ (Hz)	$\omega'_{r_{th}}$ (Hz)	$Y_{1_{exp}}$	$Y_{1_{th}}$
83.6	4627.	4728.	.8786	.9213
87.1	5040.	5025.	.9237	.9205
90.9	5511.	5354.	.9738	.9197
95.0	5931.	5717.	.9888	.9188
99.4	6044.	6115.	.8945	.9180
104.4	6682.	6578.	.9461	.9170
109.8	7271.	7090.	.9626	.9159
115.8	8080.	7674.	1.0130	.9148
122.5	8696.	8343.	.9909	.9137

k_r (cm^{-1})	$\omega''_{r_{exp}}$ (Hz)	$\omega''_{r_{th}}$ (Hz)	$Y_{3_{exp}}$	$Y_{3_{th}}$
83.6	454.3	213.5	10.18	22.15
87.1	639.0	229.5	7.89	21.89
90.9	720.0	247.5	7.65	21.63
95.0	776.6	267.6	7.64	21.37
99.4	1102.7	289.9	5.48	21.10
104.4	970.7	316.2	6.88	20.81
109.8	1053.7	345.7	6.90	20.51
115.8	1153.6	379.8	7.00	20.21
122.5	1237.8	419.5	7.02	19.89
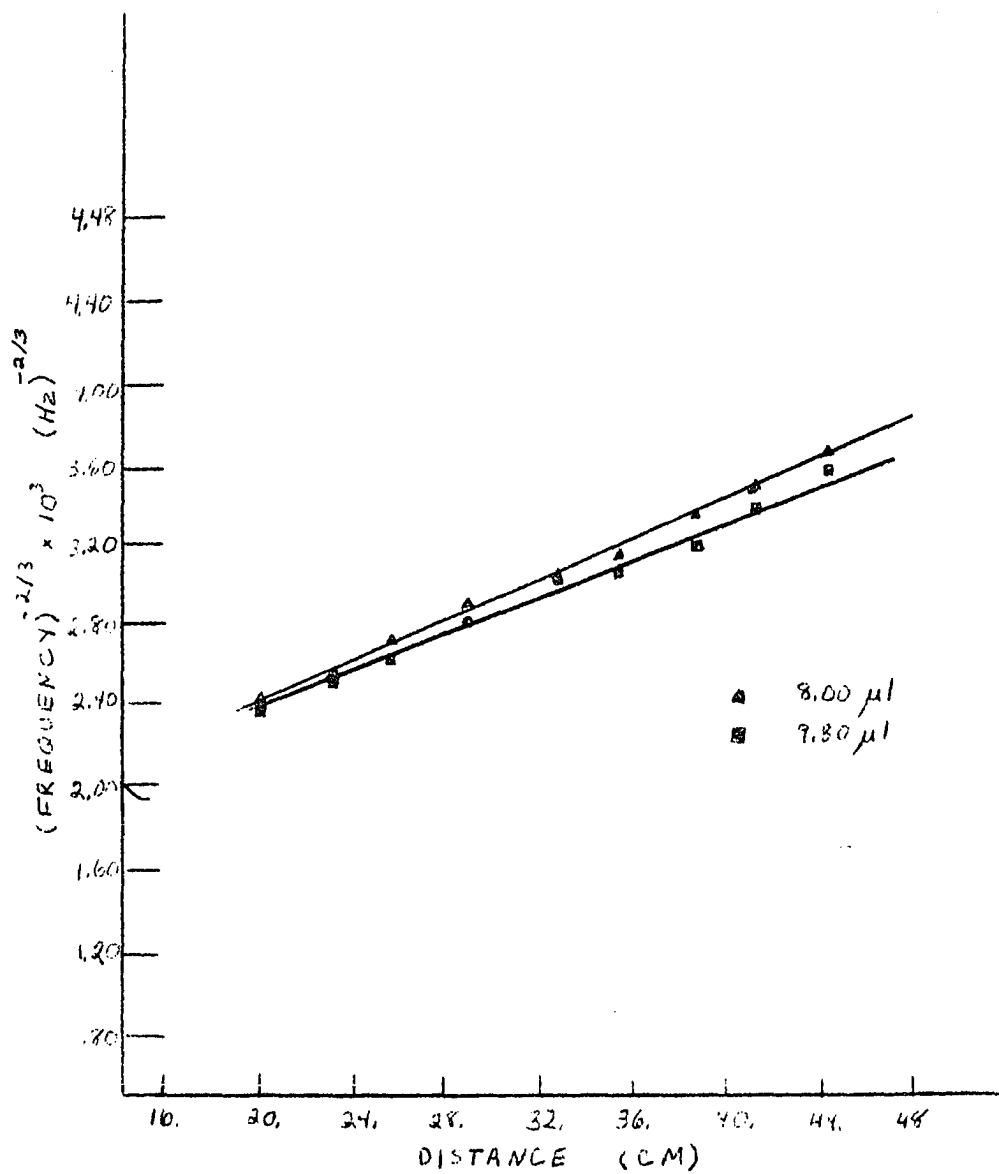
Figure 23.   Plot of $\omega^{-2/3}$ versus L' for monolayers of myristic acid on the air-water interface.

Table XVI. Air-Heptanoic Acid Interface.

conc. (moles/liter)	γ(dynes/cm)	$\dfrac{\omega r_{exp}^{-2/3}}{L}$ (sec$^{2/3}$cm^{-1})	$\dfrac{\omega r_{th}^{-2/3}}{L}$ (sec$^{2/3}$cm^{-1})
7.48×10^{-3}	37.8	5.23×10^{-5}	5.35×10^{-5}
3.75×10^{-3}	48.5	4.93×10^{-5}	4.96×10^{-5}
2.50×10^{-3}	53.0	4.57×10^{-5}	4.81×10^{-5}
7.99×10^{-6}	67.2	4.60×10^{-5}	4.44×10^{-5}
7.99×10^{-7}	68.2	4.37×10^{-5}	4.42×10^{-5}
7.99×10^{-8}	68.5	4.39×10^{-5}	4.41×10^{-5}

Table XVII. Myristic Acid Monolayer at Air-Water Interface.

conc. (μl)	$\dfrac{\overset{\circ}{A}{}^2}{molecule}$	γ(dynes/cm)	$\dfrac{\omega r_{exp}^{-2/3}}{L}$ (sec$^{2/3}$cm^{-1})	$\dfrac{\omega r_{exp}^{-2/3}}{L}$ (sec$^{2/3}$cm^{-1})
4.72	39.35	67.5	4.61×10^{-5}	4.45×10^{-5}
6.14	30.25	59.9	4.27×10^{-5}	4.61×10^{-5}
6.99	26.57	55.0	4.63×10^{-5}	4.75×10^{-5}
8.00	23.16	47.7	4.91×10^{-5}	4.98×10^{-5}
8.90	20.94	45.3	4.66×10^{-5}	5.07×10^{-5}
9.80	19.01	41.3	5.01×10^{-5}	5.23×10^{-5}

Similarly the corresponding values for pentadecanoic, palmitic, and heptadecanoic monolayers are listed in Table XVIII through Table XXXII.

Table XVIII. Pentadecanoic Acid ($4.53\mu l$) at Air-Water Interface.

k_r (cm^{-1})	$\omega'_{r_{exp}}$ (Hz)	$\omega'_{r_{th}}$ (Hz)	$Y_{1_{exp}}$	$Y_{1_{th}}$
83.6	5749.	6014.	.8462	.9283
87.1	5987.	6392.	.8128	.9275
90.9	6365.	6811.	.8098	.9267
95.0	7265.	7273.	.9249	.9258
99.4	7728.	7780.	.9118	.9250
109.8	8928.	9021.	.9048	.9229
115.8	10242.	9764.	1.0145	.9218
130.1	12463.	11610.	1.0606	.9194
138.6	14685.	12756.	1.2169	.9180
148.3	16882.	14107.	1.3121	.9165

k_r (cm^{-1})	$\omega''_{r_{exp}}$ (Hz)	$\omega''_{r_{th}}$ (Hz)	$Y_{3_{exp}}$	$Y_{3_{th}}$
83.6	434.2	280.0	13.24	21.48
87.1	573.0	301.3	10.45	21.21
90.9	622.0	325.3	10.23	20.94
95.0	520.2	352.1	13.96	20.66
99.4	615.8	381.8	12.55	20.38
109.8	556.7	426.4	16.04	19.76
115.8	408.4	502.2	25.08	19.44
130.1	696.8	618.9	17.89	18.76
138.6	567.7	693.4	25.87	18.40
148.3	613.9	783.0	27.50	18.02

Table XIX. Pentadecanoic Acid (7.93μl) at Air-Water Interface.

k_r (cm^{-1})	$\omega'_{r_{exp}}$ (Hz)	$\omega'_{r_{th}}$ (Hz)	$Y_{1_{exp}}$	$Y_{1_{th}}$
83.6	5542.	5804.	.8433	.9288
87.1	5938.	6169.	.8577	.9281
90.9	6453.	6574.	.8930	.9273
95.0	7113.	7020.	.9510	.9265
99.4	7804.	7509.	.9975	.9257
104.3	8331.	8678.	.9839	.9248
109.8	9324.	8708.	1.0587	.9239
115.8	10323.	9426.	1.1059	.9229
122.5	11498.	10249.	1.1585	.9218

k_r (cm^{-1})	$\omega''_{r_{exp}}$ (Hz)	$\omega''_{r_{th}}$ (Hz)	$Y_{3_{exp}}$	$Y_{3_{th}}$
83.6	333.0	234.4	45.76	24.76
87.1	421.0	252.0	34.47	24.48
90.9	527.8	271.7	36.52	24.20
95.0	421.0	293.7	22.15	23.90
99.4	622.0	318.2	26.52	23.60
104.3	314.2	347.0	12.55	23.28
109.8	421.0	379.3	16.89	22.96
115.8	282.7	416.7	12.23	22.62
122.5	251.3	460.3	16.64	22.26

Table XX.   Pentadecanoic Acid (10.67μ1) at Air-Water Interface

k_r (cm^{-1})	$\omega'_{r_{exp}}$ (Hz)	$\omega'_{r_{th}}$ (Hz)	$Y_{1_{exp}}$	$Y_{1_{th}}$
87.1	4933.	5208.	.8249	.9219
90.9	5265.	5549.	.8285	.9211
95.0	5838.	5925.	.8931	.9202
99.4	5897.	6338.	.7937	.9194
104.4	6032.	6818.	.7185	.9184
109.8	6792.	7349.	.7828	.9174
115.8	7358.	7954.	.7828	.9163
122.5	7898.	8648.	.7618	.9151
130.1	9060.	9457.	.8382	.9139
138.6	10342.	10391.	.9027	.9126

k_r (cm^{-1})	$\omega''_{r_{exp}}$ (Hz)	$\omega''_{r_{th}}$	$Y_{3_{exp}}$	$Y_{3_{th}}$
87.1	631.5	233.3	7.81	22.33
90.9	663.5	251.5	7.94	22.06
95.0	771.6	271.9	7.57	21.79
99.4	815.6	294.6	7.23	21.51
104.4	642.8	321.3	9.38	21.22
109.8	1026.0	351.3	6.62	20.92
115.8	1105.8	385.9	6.65	20.61
122.5	1218.9	426.3	6.48	20.28
130.1	1438.9	474.3	6.30	19.94
138.6	1399.3	530.5	7.39	19.59
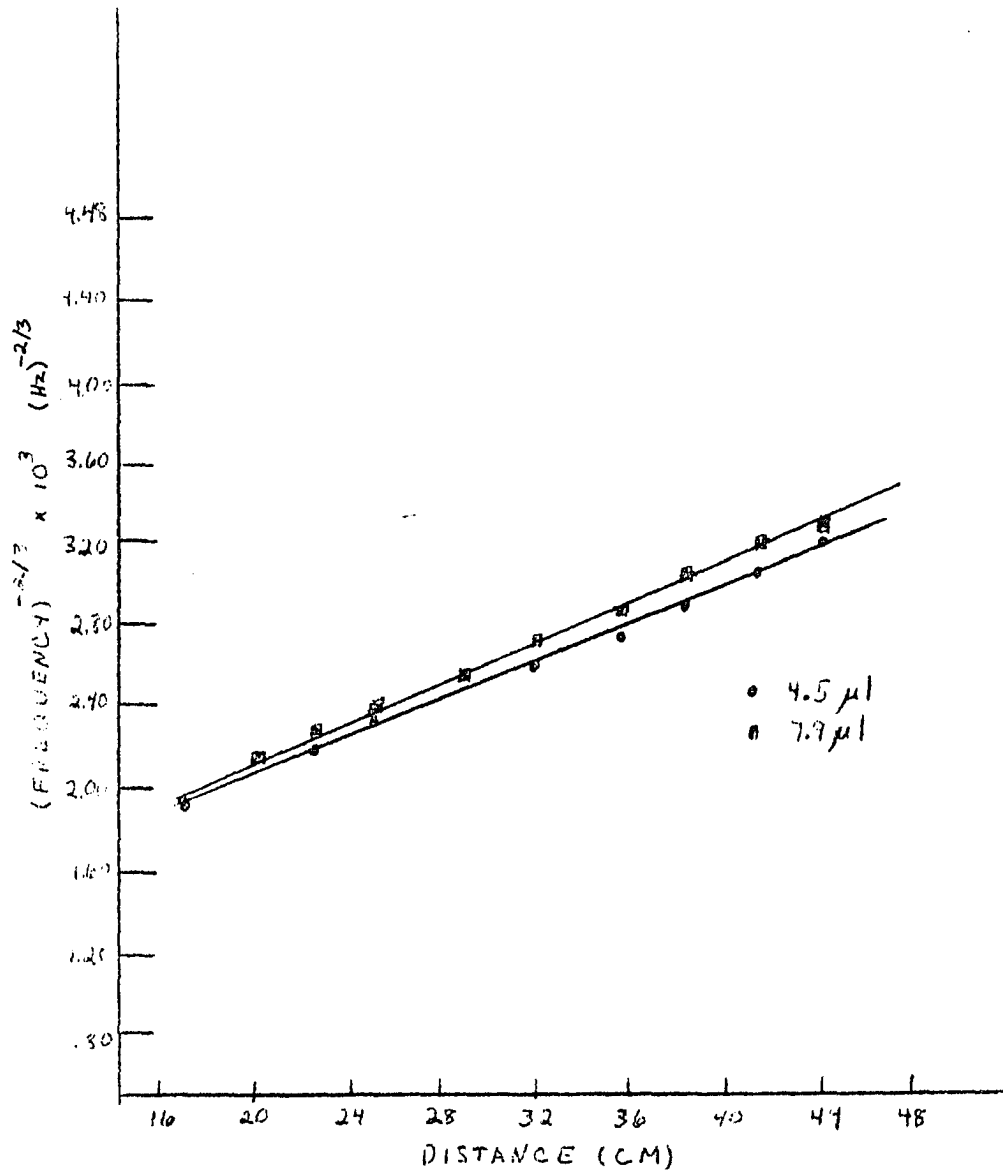
Figure 24. Plot of $\omega^{-2/3}$ versus L' for monolayers of pentadecanoic
acid on the air-water interface.

Table XXI. Palmitic Acid $(4.15\mu\text{l})$ at Air-Water Interface.

k_r (cm^{-1})	$\omega'_{r_{exp}}$ (Hz)	$\omega'_{r_{th}}$ (Hz)	$Y_{1_{exp}}$	$Y_{1_{th}}$
83.6	4989.	5622.	.7328	.9352
87.1	5236.	5976.	.7151	.9343
90.9	5716.	6368.	.7515	.9334
95.0	5991.	6799.	.7234	.9325
99.4	6363.	7273.	.7109	.9315
104.4	6855.	7823.	.7141	.9305
109.8	7532.	8432.	.7408	.9294
115.8	8044.	9127.	.7200	.9283
122.5	8805.	9923.	.7284	.9272

k_r (cm^{-1})	$\omega''_{r_{exp}}$ (Hz)	$\omega''_{r_{th}}$ (Hz)	$Y_{3_{exp}}$	$Y_{3_{th}}$
83.6	597.5	346.1	8.35	16.25
87.1	656.0	373.6	7.98	16.00
90.9	791.7	404.5	7.22	15.74
95.0	742.7	439.2	8.07	15.48
99.4	972.6	477.9	6.54	15.22
104.4	981.4	523.7	6.98	14.94
109.8	1093.3	575.4	6.89	14.65
115.8	1252.2	635.5	6.42	14.36
122.5	1430.0	705.9	6.16	14.06

Table XXII. Palmitic Acid (5.66μl) at Air-Water Interface.

$k_r (cm^{-1})$	$\omega'_{r_{exp}}$ (Hz)	$\omega'_{r_{th}}$ (Hz)	$Y_{1_{exp}}$	$Y_{1_{th}}$
83.6	4925.	5333.	.7881	.9282
87.1	5282.	5668.	.8030	.9272
90.9	5726.	6039.	.8321	.9262
95.0	6112.	·6448.	.8308	.9252
99.4	6286.	6896.	.7656	.9242
104.4	6786.	7418.	.7721	.9230
109.8	7472.	7995.	.8044	.9218
115.8	8163.	8653.	.8181	.9206
122.5	9054.	9407.	.8500	.9192
130.1	9736.	10287.	.8216	.9178
138.6	10807.	11301.	.8367	.9163

$k_r (cm^{-1})$	$\omega''_{r_{exp}}$ (Hz)	$\omega''_{r_{th}}$ (Hz)	$Y_{3_{exp}}$	$Y_{3_{th}}$
83.6	495.1	311.8	9.95	17.10
87.1	588.7	336.2	8.97	16.86
90.9	700.6	363.5	8.17	16.61
95.0	787.3	394.1	7.76	16.36
99.4	837.5	428.2	7.51	16.10
104.4	900.3	468.6	7.54	15.83
109.8	1057.5	514.0	7.07	15.56
115.8	1161.8	566.7	7.03	15.27
122.5	1222.1	628.4	7.41	14.97

Table XXIII.   Palmitic Acid (7.55μl) at Air-Water Interface.

$k_r(cm^{-1})$	$\omega'_{r_{exp}}$ (Hz)	$\omega'_{r_{th}}$ (Hz)	$Y_{1_{exp}}$	$Y_{1_{th}}$
83.6	3965.	5172.	.5397	.9242
87.1	4863.	5497.	.7204	.9233
90.9	50.86	5857.	.6944	.9223
95.0	5454.	6253.	.7000	.9213
99.4	5650.	6688.	.6546	.9202
104.4	6100.	7194.	.6604	.9191
109.8	6604.	7754.	.6648	.9179
115.8	7414.	8391.	.7143	.9166
122.5	7939.	9122.	.6916	.9153
130.1	8991.	9976.	.7417	.9138

$k_r(cm^{-1})$	$\omega''_{r_{exp}}$ (Hz)	$\omega''_{r_{th}}$ (Hz)	$Y_{3_{exp}}$	$Y_{3_{th}}$
83.6	628.3	285.3	6.31	18.13
87.1	830.0	307.2	5.86	17.89
90.9	1008.4	331.9	5.04	17.65
95.0	1080.0	359.5	5.05	17.40
99.4	1171.8	390.2	4.82	17.14
104.4	1146.7	426.4	5.32	16.87
109.8	1489.7	467.2	4.43	16.60
115.8	1382.9	514.5	5.36	16.31
122.5	1313.8	569.8	6.04	16.01
130.1	1240.3	635.5	7.25	15.70

Table XXIV. Palmitic Acid (8.78μl) at Air-Water Interface.

k_r (cm^{-1})	$\omega'_{r\,exp}$ (Hz)	$\omega'_{r\,th}$ (Hz)	$Y_{1\,exp}$	$Y_{1\,th}$
83.6	4800.	4986.	.8512	.9219
87.1	5202.	5298.	.8859	.9209
90.9	5624.	5645.	.9125	.9200
95.0	5824.	6028.	.8579	.9190
99.4	6310.	6447.	.8774	.9179
104.4	6898.	6934.	.9075	.9168
109.8	7357.	7474.	.8868	.9156
115.8	7963.	8088.	.8853	.9143
122.5	8345.	8793.	.8210	.9130

k_r (cm^{-1})	$\omega''_{r\,exp}$ (Hz)	$\omega''_{r\,th}$ (Hz)	$Y_{3\,exp}$	$Y_{3\,th}$
83.6	664.8	267.1	7.22	18.66
87.1	698.1	287.5	7.45	18.43
90.9	791.7	310.4	7.10	18.18
95.0	904.1	336.0	6.44	17.94
99.4	938.1	364.6	6.73	17.68
104.4	1081.3	398.2	6.38	17.41
109.8	1175.0	436.0	6.26	17.14
115.8	1227.7	479.9	6.49	16.86

85

Table XXV. Palmitic Acid (11.8μl) at Air-Water Interface.

k_r (cm^{-1})	$\omega'_{r_{exp}}$ (Hz)	$\omega'_{r_{th}}$ (Hz)	$Y_{1_{exp}}$	$Y_{1_{th}}$
83.6	4816.	4682.	.9687	.9190
87.1	5190.	4976.	.9968	.9181
90.9	5655.	5302.	1.0432	.9172
95.0	5881.	5661.	.9889	.9162
99.4	6347.	6054.	1.0036	.9152
104.4	6855.	6512.	1.0131	.9141
109.8	7320.	7019.	.9124	.9130
115.8	8159.	7596.	1.0509	.9118
122.5	8727.	8258.	1.0151	.9104
130.1	9525.	9030.	1.0110	.9090

k_r (cm^{-1})	$\omega''_{r_{exp}}$ (Hz)	$\omega''_{r_{th}}$ (Hz)	$Y_{3_{exp}}$	$Y_{3_{th}}$
83.6	483.8	238.4	9.95	19.64
87.1	566.7	256.5	9.16	19.40
90.9	684.9	276.8	8.26	19.16
95.0	816.8	299.4	7.20	18.91
99.4	904.8	324.6	7.01	18.65
104.4	970.7	354.2	7.06	18.38
109.8	1051.2	387.6	6.96	18.11
115.8	1110.9	426.2	7.34	17.82
122.5	1185.6	471.2	7.36	17.52

Table XXVI. Palmitic Acid (13.40μl) at Air-Water Interface.

k_r (cm^{-1})	$\omega'_{r_{exp}}$ (Hz)	$\omega'_{r_{th}}$ (Hz)	$Y_{1_{exp}}$	$Y_{1_{th}}$
83.6	4656.	4232.	1.103	.9152
87.1	4926.	4498.	1.094	.9143
90.9	5019.	4792.	1.001	.9134
95.0	5371.	5116.	1.001	.9124
99.4	5703.	5472.	1.005	.9114
104.4	6181.	5885.	.987	.9103
109.8	6670.	6343.	1.004	.9092
115.8	7226.	6864.	1.004	.9079
122.5	7829.	7462.	.996	.9066
130.1	8818.	8160.	1.056	.9051

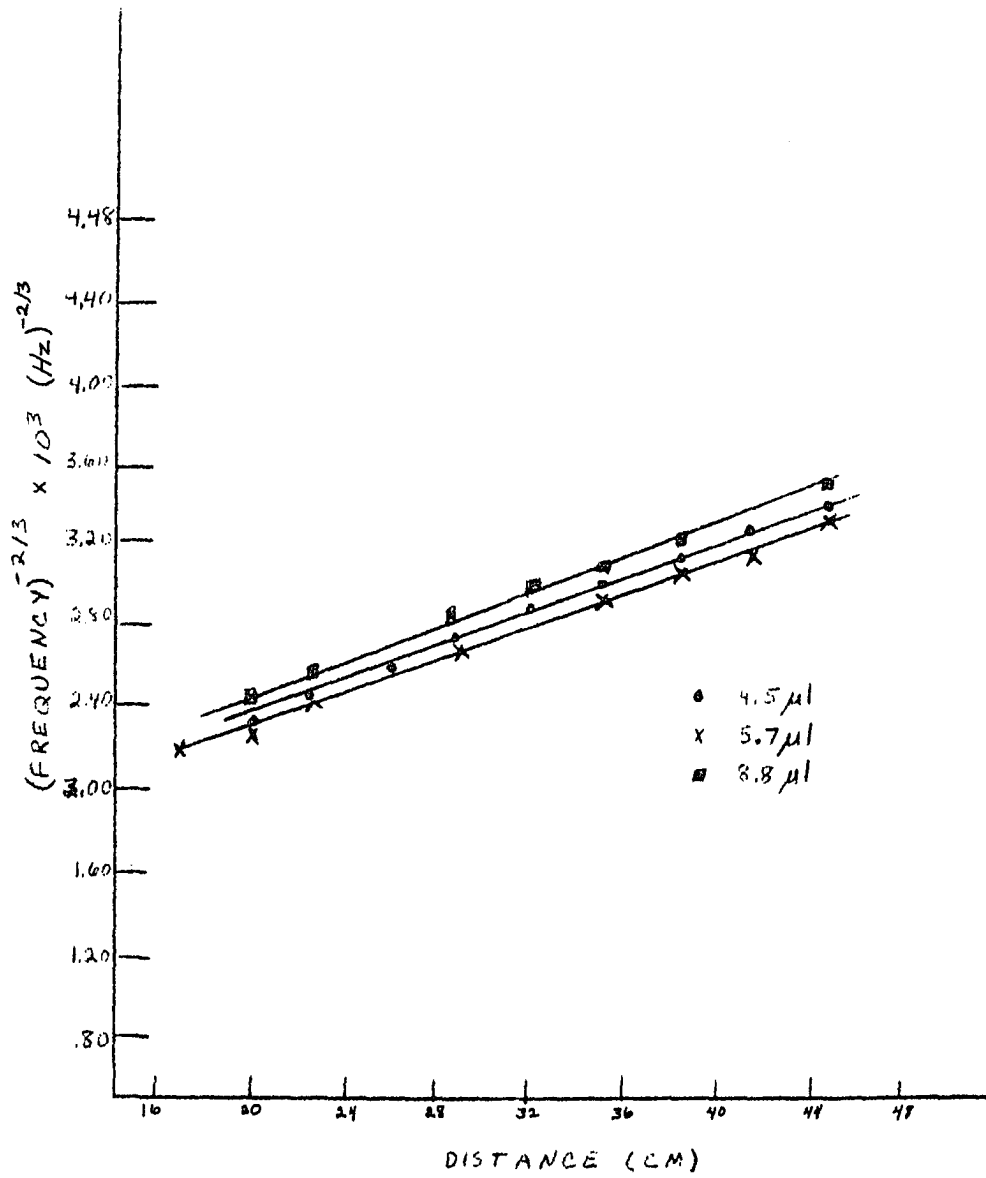| k_r (cm^{-1})	$\omega''_{r_{exp}}$ (Hz)	$\omega''_{r_{th}}$ (Hz)	$Y_{3_{exp}}$	$Y_{3_{th}}$
83.6	721.3	218.6	6.45	19.36
87.1	736.4	235.1	6.69	19.13
90.9	948.8	253.6	5.29	18.89
95.0	1032.2	274.3	5.20	18.65
99.4	1170.6	297.3	4.87	18.41
104.4	1244.1	324.4	4.97	18.14
109.8	1279.9	354.8	5.21	17.88
115.8	1140.4	390.0	6.34	17.60
122.5	1045.5	431.0	7.49	17.31
130.1	1016.0	479.8	8.68	17.01

Figure 25. Plot of $\omega^{-2/3}$ versus L' for monolayers of palmitic acid on the air-water interface.

Table XXVII. Heptadecanoic Acid (4.4μl) at Air-Water Interface.

k_r (cm^{-1})	$\omega'_{r_{exp}}$ (Hz)	$\omega'_{r_{th}}$ (Hz)	$Y_{1_{exp}}$	$Y_{1_{th}}$
83.6	4907.	5982.	.6215	.9283
87.1	5202.	6358.	.6189	.9276
90.9	5628.	6775.	.6386	.9268
95.0	5956.	7235.	.6269	.9260
99.4	6357.	7739.	.6220	.9251
104.4	6644.	8326.	.5881	.9242
109.8	7301.	8974.	.6101	.9232
115.8	8042.	9714.	.6308	.9221
122.5	7615.	10562.	.4774	.9210

k_r (cm^{-1})	$\omega''_{r_{exp}}$ (Hz)	$\omega''_{r_{th}}$ (Hz)	$Y_{3_{exp}}$	$Y_{3_{th}}$
83.6	413.4	262.0	11.87	22.83
87.1	620.2	281.8	8.39	22.56
90.9	692.4	304.1	8.13	22.28
95.0	728.2	329.0	8.18	21.99
99.4	905.4	356.6	7.02	21.70
104.4	1011.6	389.2	6.57	21.39
109.8	899.8	425.8	8.11	21.08
115.8	1076.3	468.2	7.47	20.75

Table XXVIII. Heptadecanoic Acid (8.8μl) at Air-Water Interface.

k_r (cm^{-1})	$\omega'_{r_{exp}}$ (Hz)	$\omega'_{r_{th}}$ (Hz)	$Y_{1_{exp}}$	$Y_{1_{th}}$
83.6	4665.	4848.	.8501	.9221
87.1	5129.	5153.	.9106	.9213
90.9	5605.	5491.	.9586	.9205
95.0	5812.	5863.	.9034	.9197
99.4	6234.	6271.	.9057	.9188
104.4	6575.	6746.	.8719	.9178
109.8	7317.	7272.	.9278	.9168
115.8	7920.	7870.	.9263	.9157
122.5	8656.	8557.	.9344	.9146
130.1	9677.	9358.	.9762	.9133

k_r (cm^{-1})	$\omega''_{r_{exp}}$ (Hz)	$\omega''_{r_{th}}$ (Hz)	$Y_{3_{exp}}$	$Y_{3_{th}}$
83.6	493.2	216.2	9.46	22.42
87.1	585.6	232.5	8.76	22.16
90.9	686.9	250.7	8.16	21.90
95.0	859.5	271.1	6.76	21.63
99.4	920.5	293.7	6.77	21.36
104.4	998.4	320.3	6.59	21.06
109.8	1145.4	350.2	6.39	20.76
115.8	1119.6	348.8	7.07	20.45
122.5	1278.0	425.0	6.77	20.13
130.1	1378.5	472.8	7.02	19.79

Table XXIX. Heptadecanoic Acid (12.3μl) at Air-Water Interface.

k_r (cm^{-1})	$\omega'_{r_{exp}}$ (Hz)	$\omega'_{r_{th}}$ (Hz)	$Y_{1_{exp}}$	$Y_{1_{th}}$
83.6	4587.	4293.	1.0426	.9166
87.1	4953.	4563.	1.0774	.9158
90.9	5439.	4861.	1.1456	.9149
95.0	5666.	5190.	1.0895	.9140
99.4	5968.	5552.	1.0529	.9130
104.4	6292.	5971.	1.0128	.9119
109.8	6868.	6436.	1.0367	.9108
115.8	7477.	6965.	1.0473	.9097
122.5	8488.	7572.	1.1399	.9084
130.1	9324.	8280.	1.1500	.9070

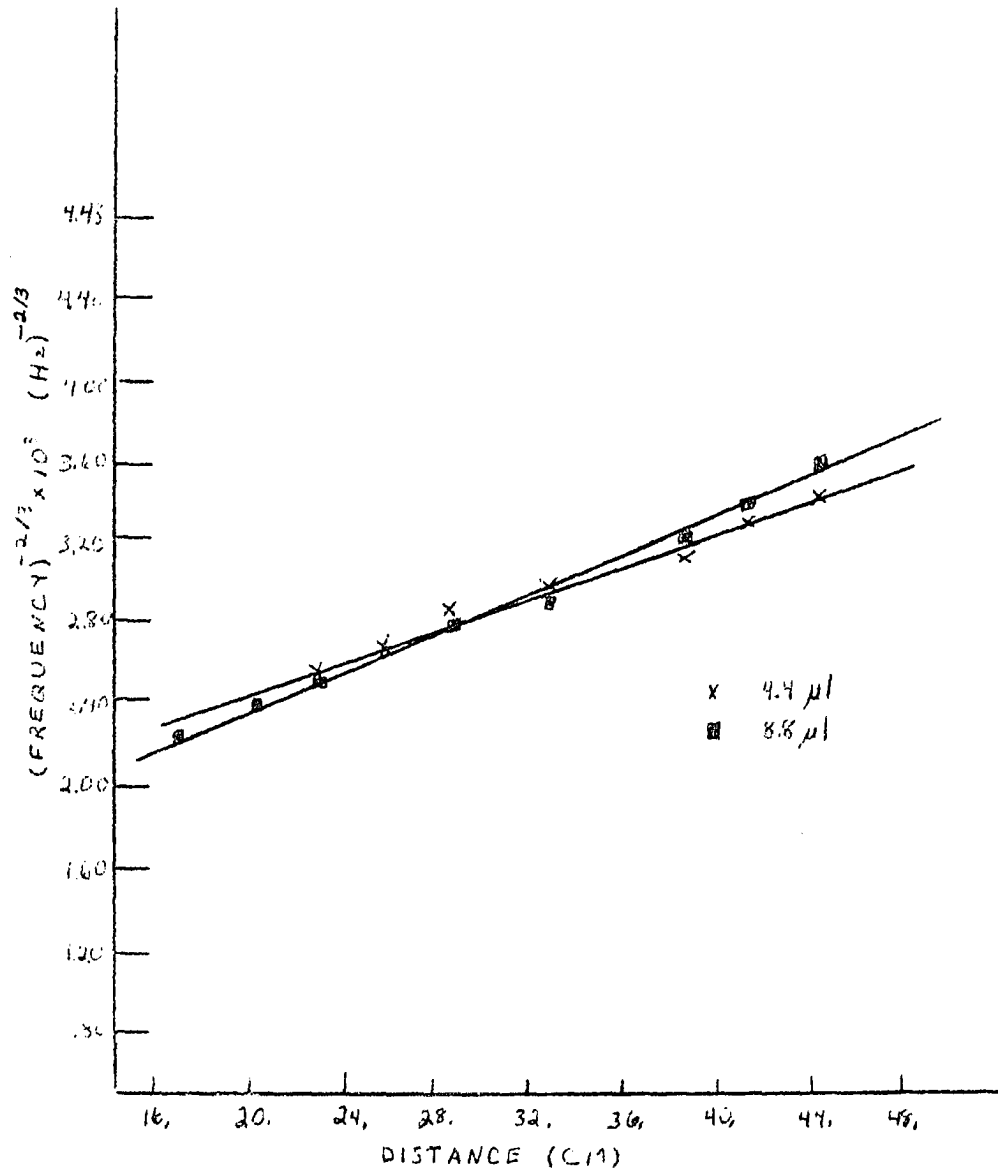| k_r (cm^{-1})	$\omega''_{r_{exp}}$ (Hz)	$\omega''_{r_{th}}$ (Hz)	$Y_{3_{exp}}$	$Y_{3_{th}}$
83.6	557.9	210.6	8.22	20.39
87.1	620.2	226.4	7.99	20.15
90.9	671.7	244.2	8.10	19.91
95.0	732.6	264.1	7.73	19.66
99.4	826.9	286.1	7.22	19.40
104.4	882.8	312.1	7.13	19.13
109.8	960.1	341.3	7.15	18.86
115.8	898.5	375.1	8.32	18.57
122.5	1196.3	414.5	7.09	18.27
130.1	1044.3	461.2	8.93	17.96

Figure 26. Plot of $\omega^{-2/3}$ versus L' for monolayers of heptadecanoic acid on the air-water interface.

Table XXX. Pentadecanoic Acid Monolayer at Air-Water Interface.

conc. (μl)	$\frac{A^2}{molecule}$	γ (dynes/cm)	$\frac{\omega_{r\,exp}^{-2/3}}{L}$ (sec$^{2/3}$cm^{-1})	$\frac{\omega_{r\,th}^{-2/3}}{L}$ (sec$^{2/3}$cm^{-1})
4.53	38.45	66.4	4.77×10^{-5}	4.46×10^{-5}
7.93	21.96	61.8	4.90×10^{-5}	4.58×10^{-5}
10.67	16.32	44.3	5.17×10^{-5}	5.11×10^{-5}

Table XXXI. Palmitic Acid Monolayer at Air-Water Interface.

conc. (μl)	$\frac{A^2}{molecule}$	γ (dynes/cm)	$\frac{\omega_{r\,exp}^{-2/3}}{L}$ (sec$^{2/3}$cm^{-1})	$\frac{\omega_{r\,th}^{-2/3}}{L}$ (sec$^{2/3}$cm^{-1})
4.15	121.80	57.6	4.50×10^{-5}	4.68×10^{-5}
5.66	89.30	52.2	4.64×10^{-5}	4.84×10^{-5}
7.55	66.95	49.3	5.40×10^{-5}	4.94×10^{-5}
8.78	57.57	45.9	4.54×10^{-5}	5.05×10^{-5}
11.80	42.84	40.6	4.68×10^{-5}	5.25×10^{-5}
13.40	37.72	33.4	4.65×10^{-5}	5.62×10^{-5}

Table XXXII. Heptadecanoic Acid Monolayer at Air-Water Interface.

conc. (μl)	$\frac{A^2}{molecule}$	γ (dynes/cm)	$\frac{\omega_{r\,exp}^{-2/3}}{L}$ (sec$^{2/3}$cm^{-1})	$\frac{\omega_{r\,th}^{-2/3}}{L}$ (sec$^{2/3}$cm^{-1})
4.4	35.28	65.7	4.03×10^{-5}	4.48×10^{-5}
8.8	17.64	43.4	4.86×10^{-5}	5.13×10^{-5}
12.3	12.62	34.2	5.15×10^{-5}	5.56×10^{-5}

The polymer films were handled differently from the fatty acids,

both theoretically and experimentally. The polymer monolayers were

studied in an enclosed chamber to prevent their oxidation. The values

for the viscosity and elasticity were not calculated from an equation of

state, but were obtained from the publication of Ikeda and Isemura (61).

The surface tension values were determined with a du Nouy tensiometer.

The values for the slopes of the plots of $\omega_r'^{-2/3}$ versus L are listed

with the surface tension values in Tables XXXIII and XXXIV. The values

for ω_r' , ω_r'' , Y_1 , and Y_3 are listed in Table XXXV through Table

XXXIX.

Table XXXIII. Poly-γ-benzyl-L-Glutamate Monolayer at Air-Water
Interface.

conc. (μl)	mg/m²	γ (dynes/cm)	$\dfrac{\omega_{r\,exp}'^{-2/3}}{L}$ (sec$^{2/3}$cm^{-1})	$\dfrac{\omega_{r\,th}'^{-2/3}}{L}$ (sec$^{2/3}$cm^{-1})
4.0	0.6	71.0	4.36×10^{-5}	4.31×10^{-5}
8.0	0.9	69.9	4.40×10^{-5}	4.43×10^{-5}
12.0	1.1	63.4	4.46×10^{-5}	4.50×10^{-5}

Table XXXIV. Poly-γ-methyl-L-glutamate Monolayer at Air-Water
Interface.

conc. (μl)	mg/m²	γ (dynes/cm)	$\dfrac{\omega_{r\,exp}'^{-2/3}}{L}$ (sec$^{2/3}$cm^{-1})	$\dfrac{\omega_{r\,th}'^{-2/3}}{L}$ (sec$^{2/3}$cm^{-1})
8.0	0.9	69.4	4.41×10^{-5}	4.45×10^{-5}
12.0	1.1	63.0	4.47×10^{-5}	4.53×10^{-5}

Table XXXV. Poly-γ-benzyl-L-glutamate (4.0μl) at Air-Water-Interface.

k_r (cm^{-1})	$\omega'_{r\,exp}$ (Hz)	$\omega'_{r\,th}$ (Hz)	$Y_{1\,exp}$	$Y_{1\,th}$
83.6	5122.	6227.	.6366	.9311
87.1	5561.	6619.	.6648	.9304
90.9	6057.	7054.	.6954	.9297
95.0	6183.	7533.	.6350	.9290
99.4	6609.	8058.	.6321	.9282
104.4	7157.	8669.	.6415	.9273
109.8	7855.	9345.	.6639	.9264
115.8	8642.	10116.	.6849	.9255
122.5	9361.	11000.	.6785	.9244

k_r (cm^{-1})	$\omega''_{r\,exp}$ (Hz)	$\omega''_{r\,th}$ (Hz)	$Y_{3\,exp}$	$Y_{3\,th}$
83.6	554.8	241.4	9.23	25.79
87.1	609.5	259.5	9.12	24.50
90.9	837.5	279.9	7.23	25.20
95.0	931.8	302.6	6.63	24.90
99.4	1021.6	327.7	6.46	24.58
104.4	1071.9	357.4	6.67	24.25
109.8	1100.2	390.7	7.14	23.92
115.8	1195.1	429.2	7.23	23.57
122.5	1355.9	474.1	6.90	23.20

Table XXXVI. Poly-γ-benzyl-L-glutamate (8.0μl) at Air-Water Interface.

k_r (cm^{-1})	$\omega'_{r_{exp}}$ (Hz)	$\omega'_{r_{th}}$ (Hz)	$Y_{1_{exp}}$	$Y_{1_{th}}$
83.6	5028.	6178.	.6762	.9309
87.1	5460.	6567.	.7067	.9302
90.9	5894.	6998.	.7259	.9294
95.0	6064.	7473.	.6734	.9287
99.4	6309.	7995.	.6349	.9279
104.4	7037.	8600.	.6838	.9270
109.8	7658.	9271.	.6957	.9261
115.8	8246.	10036.	.6874	.9252
122.5	8994.	10913.	.6905	.9241

k_r (cm^{-1})	$\omega''_{r_{exp}}$ (Hz)	$\omega''_{r_{th}}$ (Hz)	$Y_{3_{exp}}$	$Y_{3_{th}}$
83.6	597.5	240.5	8.41	25.68
87.1	648.4	258.6	8.42	25.40
90.9	698.7	278.9	8.44	25.10
95.0	767.8	301.5	7.89	24.79
99.4	790.4	326.6	7.98	24.48
104.4	1086.4	356.1	6.47	24.15
109.8	888.4	389.3	8.61	23.81
115.8	1087.6	427.7	7.58	23.46

Table XXXVII. Poly-γ-benzyl-L-glutamate(12.0μl) at Air-Water Interface.

k_r (cm^{-1})	$\omega'_{r_{exp}}$ (Hz)	$\omega'_{r_{th}}$ (Hz)	$Y_{1_{exp}}$	$Y_{1_{th}}$
83.6	4962.	5879.	.7416	.9292
87.1	5517.	6249.	.8126	.9285
90.9	5884.	6659.	.8147	.9277
95.0	6120.	7111.	.7725	.9270
99.4	6462.	7607.	.7504	.9261
104.4	7008.	8184.	.7637	.9252
109.8	7601.	8822.	.7719	.9243
115.8	8398.	9549.	.8029	.9234
122.5	9006.	10383.	.7798	.9223

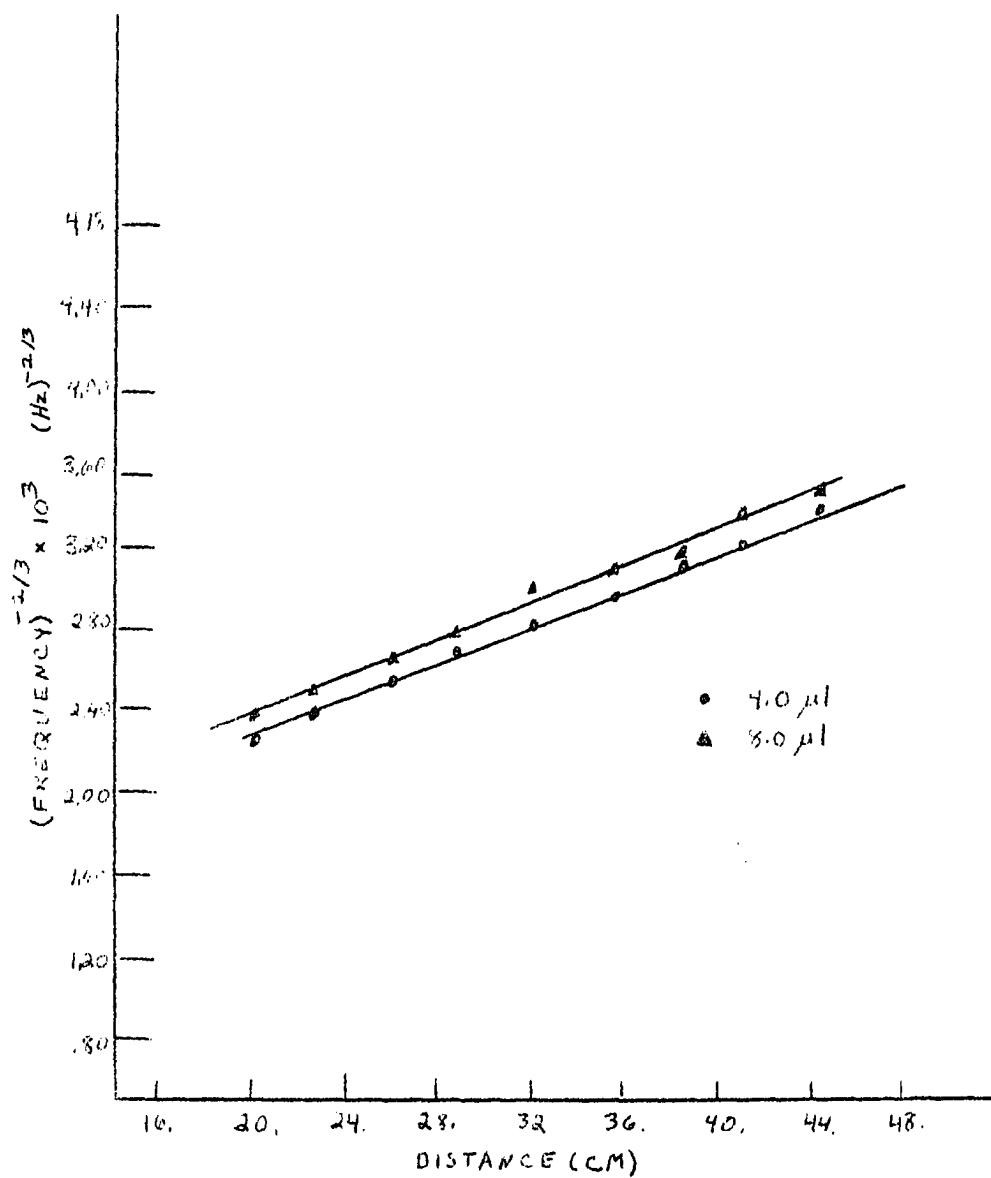| k_r (cm^{-1})	$\omega''_{r_{exp}}$ (Hz)	$\omega''_{r_{th}}$ (Hz)	$Y_{3_{exp}}$	$Y_{3_{th}}$
83.6	523.4	235.2	9.48	25.00
87.1	582.4	252.8	9.47	24.72
90.9	622.0	272.7	9.46	24.42
95.0	810.5	294.8	7.55	24.13
99.4	965.7	319.3	6.69	23.82
104.4	980.8	348.2	7.14	23.50
109.8	1029.2	380.7	7.38	23.17
115.8	1055.6	418.2	7.95	22.83

Figure 27. Plot of $\omega^{-2/3}$ versus L' for monolayers of poly-γ-benzyl-L-glutamate on the air-water interface.

Table XXXVIII. Poly-γ-methyl-L-glutamate(8.0μ1) at Air-Water Interface.

k_r (cm^{-1})	$\omega'_{r_{exp}}$ (Hz)	$\omega'_{r_{th}}$ (Hz)	$Y_{1_{exp}}$	$Y_{1_{th}}$
83.6	4989.	6147.	.6658	.9307
87.1	5385.	6534.	.6872	.9300
90.9	5698.	6962.	.6783	.9293
95.0	5928.	7435.	.6435	.9285
99.4	6141.	7954.	.6015	.9277
104.4	6905.	8557.	.6582	.9268
109.8	7672.	9224.	.6982	.9260
115.8	8036.	9984.	.6527	.9250
122.5	8766.	10857.	.6559	.9240

k_r (cm^{-1})	$\omega''_{r_{exp}}$ (Hz)	$\omega''_{r_{th}}$ (Hz)	$Y_{3_{exp}}$	$Y_{3_{th}}$
83.6	554.8	240.0	8.99	25.61
87.1	648.4	258.0	8.30	25.32
90.9	754.6	278.2	7.55	25.03
95.0	854.5	300.8	6.93	24.72
99.4	944.4	325.8	6.50	24.41
104.4	1002.2	355.3	6.89	24.08
109.8	909.2	388.4	8.44	23.75
115.8	1080.7	426.7	7.44	23.40

Table XXXIX. Poly-γ-methyl-L-glutamate(12.0μ1) at Air-Water Interface.

k_r (cm^{-1})	$\omega'_{r_{exp}}$ (Hz)	$\omega'_{r_{th}}$ (Hz)	$Y_{1_{exp}}$	$Y_{1_{th}}$
83.6	4942.	5860.	.7358	.9291
87.1	5325.	6229.	.7568	.9284
90.9	5667.	6638.	.7556	.9276
95.0	5904.	7088.	.7188	.9268
99.4	6321.	7583.	.7177	.9260
104.4	6822.	8157.	.7236	.9251
109.8	7724.	8793.	.7970	.9242
115.8	7824.	9518.	.6967	.9232
122.5	8815.	10349.	.7470	.9222

k_r (cm^{-1})	$\omega''_{r_{exp}}$ (Hz)	$\omega''_{r_{th}}$ (Hz)	$Y_{3_{exp}}$	$Y_{3_{th}}$
83.6	621.4	234.8	7.95	24.95
87.1	695.5	252.5	7.65	24.67
90.9	813.0	272.3	6.97	24.38
95.0	924.3	294.3	6.38	24.08
99.4	1024.8	318.8	6.16	23.78
104.4	1046.1	347.7	6.52	23.46
109.8	1224.0	380.1	6.31	23.13
115.8	1385.4	417.6	5.64	22.79

DISCUSSION

The nature of the roots and how they vary with k_r has been discussed in the paper mentioned previously (60). The rationalized set of roots has not yielded, as yet, any new insight into the physical meaning of any of the roots other than those which correspond to the longitude and transverse modes of space damped ripples. The difficulty with the rationalized set of roots is not only the extended length of time required to converge on a root but also that the polynomial coefficients are now so large that one is now trying to discern a very small difference from two large numbers. Thus the remainder left after convergence is still quite large and there is the strong possibility that there will be less accuracy in the roots obtained.

Accuracy might be improved by using machine language for the program to obtain a higher precision than the double precision used now. But before one attempts this solution, one must examine whether or not the attempt is warranted. Since there is approximately a six per cent deviation between experimental results and the theoretical results, the time should be spent in either improving the theory, in refining the experimental accuracy, or in working in a different frequency range. To decide which, one must analyze closely the results obtained.

As one studies the results obtained both experimentally and theoretically for ω_r', one sees that the values differ by 0.87%, at best, in the

case of heptadecanoic acid (8. 8μl) monolayer, and by 21%, at worst, in the case of myristic acid (4. 72μl) monolayer. Most of the values for the various systems differ by about six per cent. The differences between $Y_{1_{exp}}$ and $Y_{1_{th}}$ reflect the square of the deviation in the values for ω'_r .

The values obtained for ω''_r experimentally are always two to three times as large as those obtained theoretically.

What level of accuracy should one expect? The wave number k_r is a function of the aperture separation, $2x_o$, the distance from the aperture screen to the interface, L, and the wave number of the incident radiation, k_o , according to Eq 24. The aperture separation is determined by a microphotometer to within $\pm$ 1 micron--that is, to an accuracy of $\pm$.2% of the value for $2x_o$. L is determined to within $\pm$.2mm --that is, to an accuracy from 1% to .35% as L is varied from 20cm to 70cm. The wave number of the laser is constant at 1. 2875 x 10^5cm^{-1}. Thus, from a knowledge of L and $2x_o$, the ripplon wave number can be determined to within $\pm$ 1. 2%. The multichannel analyzer allows the determination of ω'_r to better than one per cent. The surface tension is determined to $\pm$ .2 dynes/cm with either the du Nauy tensiometer or the film balance method. At worst, when γ = 30 dynes/cm, this would mean an uncertainty of 1. 5% . The discrepancy between theory and experiment thus appears to be larger than expected from an analysis of experimental errors.

It was generally found that the experimental value of ω'_r was smaller

and of ω_r'' larger than predicted theoretically. This suggested that possibly the resolution of $\hat{\omega}_r = \omega_r' - i\omega_r'' = |\omega_r| \, e^{-i\theta}$ into real and imaginary components was improperly accomplished. To test this possibility the magnitudes of $\hat{\omega}_r$, i.e. $(\omega_r'^2 + \omega_r''^2)^{1/2}$, obtained theoretically and experimentally were compared. Except for the polymeric films and adsorbed films formed at four fatty acid concentrations, experimental magnitudes of ω_r agreed with theoretical magnitudes within experimental error (1.5%).

Those systems where the theoretical results and experimental results still differ are those where the difference is quite large (about 16%). In each of these systems one is dealing with a very dilute monolayer of the fatty acid or polymer. This suggests that there may be something basically wrong with the model for the surface force balance equations in the intermediate region between the zero elastic case (air-water interface) and the compressed monolayer case.

One still does not have a good estimation of the accuracy of ω_r''. To approximate the expected results, one can derive the equation

$$\omega_r'' = \frac{3}{2} \frac{\alpha_r}{k_r} \, \omega_r'$$

from the discussion of Lucassen-Reynders and Lucassen (36) on the relationship between the space damping coefficient, α_r, and the time damping coefficient. Using 0.04 for α_r / k_r, one finds that the values for ω_r'' should be from about 300 Hz to 800 Hz for ω_r' values of the experiment.

The uncertainty in ω_r'' experimentally is ± 40 Hz out of 300 Hz or 14%. The uncertainty is of this magnitude because one does not actually get the type of spectrum indicated in Figure 4 but rather one like that in Figure 28. One of the possible explanations for this shape of spectra is that one is obtaining information on the space damping of the ripples as they cross the interference pattern. If one writes the current power spectrum as a sum of the contribution from each fringe in the twenty fringe diffraction pattern,

$$G_i(\omega) = \sum_{n=1}^{20} \frac{G_n^0(0)}{1 + \left(\frac{\omega - \omega_r'}{\omega_r''}\right)^2} \quad .$$

If the amplitude of the wave is unchanged as it passes through the diffraction pattern, $G_1^0 = G_2^0 = \ldots = G_{20}^0$. This is not the case, and the amplitude of the wave is space damped by the factor $\exp(-\alpha_r x)$. The limiting values for α_r for the case of $\epsilon = 0$ and $\epsilon = \infty$ are

$\alpha(\omega) = .0016 \, k_r^{3/2}(\omega)$ and $\alpha_r(\omega) = 1008 \, k_r^{5/4}(\omega)$, respectively. Thus the current power spectrum would be written as:

$$G_i(\omega) = \sum_{n=1}^{20} \frac{b \, G_0^0 \, e^{-\alpha_r(\omega)x_n}}{1 + \left(\frac{\omega - \omega_r'}{\omega_r''}\right)^2} \quad ,$$

where b is an empirical constant that is a function of the number of scans of the multichannel analyzer. This function was programmed into the computer for the two limiting elasticity cases with experimental values for ω_r' and ω_r''. The theoretical spectra obtained from the computer looked little like Figure 28.
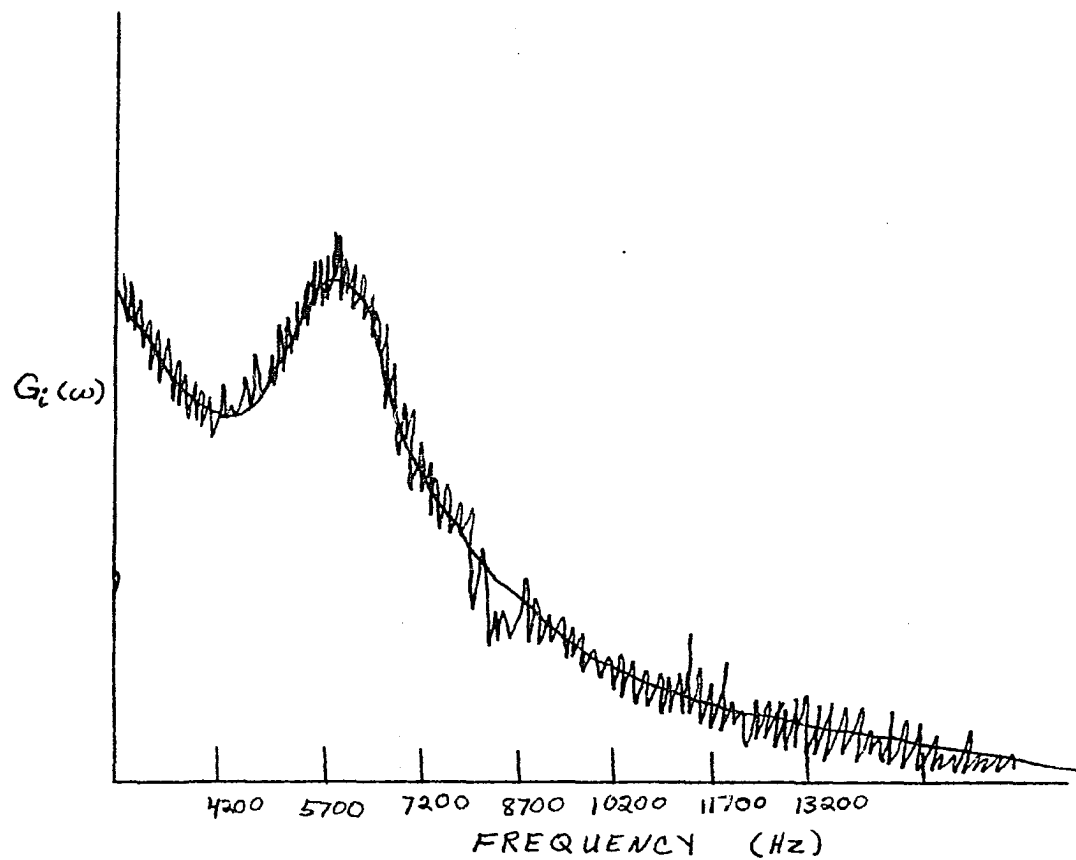
Figure 28. Spectrum for myristic acid $(8.90\mu 1)$ monolayer on the air-water interface with $L' = 35.0\,cm$. The smooth line is the spectrum predicted when the factor b/ω^2 is included.

The next consideration is whether the additional shape to the curve might be the result of the amplitude attenuation of the electromechanical transducer. This effect was studied, but the conclusion that its effect was negligible is highly unlikely since the amplitude of the transducer usually decays according to $1/\omega^2$ for $\omega > 1000$ Hz (35). The false conclusion of the experiment is quite likely the result of the displacement of the light by the optical lever being too small to be noticed. A plot with b/ω^2 as the factor times the initial current power spectrum gives the power spectrum shown in Figure 28.

Since the space damping coefficient is the important parameter in determining the selection of the ripplon wave number and the signal-to-noise ratio, the following points are to be remembered (60):

1. Ripplon wave number selection follows the rule that given a k_r, the electric field on the optical axis at the photodetector is proportional to

$$\frac{1}{\left(\dfrac{\pi\left(-\dfrac{k_r}{k_0} + \dfrac{2x_0}{L}\right)}{\dfrac{1}{2}\lambda\alpha r}\right)^2 + 1} \quad .$$

This is the space analog of the Lorentzian line shape of the frequency spectrum.

2. Sharp selection depends on $Y_2 = (\alpha_r/k_r) \ll 1$. This means that sharp selection occurs when the ripples of a given k_r span a large number of fringes in space.

3. A sufficient area of the surface must be illuminated so that light can

be collected from enough fringes to insure maximum selection.

4. Only a small region of the image plane close to the optical axis should be admitted to the photodetector for maximum k_r selection.

Each of the components of the experimental apparatus has its own limit that it sets as the upper limit of the frequency wave number which can be studied. The serious limits are set by the laser pencil size, the aperture system, and the electromechanical transducer.

The electromechanical transducer must have a flat response up to the highest frequency at which one is considering observing. Currently ω_{max} = 62000 Hz. If this is not the case, one will get the type of spectrum which is difficult, at best, to interpret. It may be possible to compensate mechanically for the non-constant background somewhat in the manner used in electron diffraction.

The laser beam has a diameter of 5mm which limits $2x_o$ to that value. Therefore if L = 30.0cm, k_r = 2.1 x 10^3cm^{-1} , and from the Kelvin equation the upper limit is ω = 2.2 x 10^5 Hz. The distance from the aperture screen to the interface must be at least 30cm since the diffraction pattern requires that $2x_o/L \ll 1$.

The use of the laser line filter before the photomultiplier places an upper limit of ω = 7.5 x 10^5 Hz on the system. The dead time of the photomultiplier sets the upper limit at ω = 7.2 x 10^6 Hz. The random noise generator places an upper limit at ω = 31 x 10^6 Hz on the system.

The goal of this thesis--to simplify the heterodyne spectroscopic

method to examine at higher frequencies the viscoelastic properties of interfaces--has been accomplished. The use of the Rudd method of wave front division gives the experimental apparatus a simplicity and flexibility that is unequaled by any other reported. Although the random pumping to generate the ripples allows one to readily observe the Brillouin peak and line shape between 3000 Hz $< \omega_r^!$ $<$ 7000 Hz, it may also be causing the discrepancy between the observed and theorized values for $\omega_r^!$ and $\omega_r^{!!}$. This can be corrected with little difficulty since electromechanical transducers are now available which are rated as flat up to ω = 62000 Hz.

At the present experimental and theoretical state one can get an idea of the deviation of an interface from the air-pure fluid case. From this basic developmental work, one can refine the technique, especially by improving the transducer, in order to get results which will be a basis for judging the adequacy of the surface balance of forces. Since there is no theory which will a priori predict viscoelastic parameters from molecular considerations, one must continue merely to compare experimental results with those of the model.

The identification of relaxation with viscous damping of hydrodynamic waves on the interface will permit the determination of the behavior of the surface viscosity. Besides studying the viscoelastic nature of interfaces in the range 10^{-3} sec to 10^{-5} sec, this method offers the possibility for probing certain macromolecular reactions in relaxation times in this same region (62). Reorientation of macromolecules (63) which

occur in this time range can also be studied with this method. The possibility of studying the viscoelastic nature of artificial membranes will be investigated.

The specific limits of times from 10^{-3} sec to 10^{-5} sec is imposed by the limits on the wave number mentioned above. The aperture system not only allows for easily attained wavefront matching, but also lets one work in this time range which cannot be realized by conventional heterodyne techniques (43). To work with relaxation times less than 10^{-5} sec, one must employ the conventional heterodyne technique.

This thesis has concerned itself with only the Brillouin type of radiation scattering. To place this work in proper perspective, Brillouin scattering will be related to the other types of radiation scattering--that is, to Rayleigh and Raman scattering. If one is considering energy transfer, the Brillouin region of energy space can be roughly ascribed to be from 10^{-5} eV to 10^{-8} eV. The Raman and Rayleigh regions are 1eV to 10^{-4} eV and 10^{-9} eV to 10^{-13} eV, respectively. The wave numbers that all of these methods can detect is in the 10^2 cm^{-1} to 10^5 cm^{-1} region (52).

Rayleigh scattering has become very popular with the advent of the optical homodyne beat spectroscopic method. Raman spectroscopy employs grating monochromatons to resolve the scattering in its energy region. Instead of the optical interferometers used previously, Brillouin scattering is now most easily studied by the optical heterodyne beat spectroscopic method. Overlapping of detection techniques should become

a logical extension of developments in the techniques of laser light scattering. A more complete understanding of the dynamical properties of systems will require the combination of the results from these methods with measurements using such techniques as magnetic resonance and dielectric relaxation in order to cover a wide range of wavenumbers and frequencies.

ADDENDUM

There are a few clarifications about this experiment that should

be noted.

1. On page 25 of this thesis, the coherence area is defined as the

region on the scattered wave front over which there is spatial coherence.

Specifically for this experiment, this is the inner Airy ring and thus its

image on the photodetector.

2. The bandwidth of the wave analyzer was about the same size as

the expected line width of the Brillouin peaks. Since one does not actu-

ally record

$$G_i(\omega) = A/(1 + (\tfrac{\omega-\omega_r'}{\omega_r''})^2)$$

where $\quad A = 2\,i_\omega \langle i_s \rangle /\pi\omega_r''$,

but rather

$$\overline{G}_i(\omega) = \tfrac{1}{\Delta\omega}\int_{\omega-\frac{\Delta\omega}{2}}^{\omega+\frac{\Delta\omega}{2}} G_i(\omega)\, d\omega ,$$

the bandwidth, $\Delta\omega$, of the detection apparatus for this experiment may

profoundly affect the observed spectrum. This can be seen by carrying

out this integration of the expansion of $G_i(\omega)$. Doing this, one gets as

the first corrected representation for $\overline{G}_i(\omega)$,

$$\overline{G}_i(\omega) = A \left\{ 1 - \frac{(\omega-\omega_r')^2 + \tfrac{1}{12}(\Delta\omega)^2}{(\omega_r'')^2} \right\}$$

Although there would be no difficulty in explicitly evaluating the effect of

the wave analyzer's bandwidth, the interpretation wouldn't be straight-

forward in terms of the half-width at half-height for $G_i(\omega)$. One can

easily see, however, that it will result in a depression of peak maximum and thus the half-width at half-height would be larger than theoretically expected. In the present experiments the bandwidth was 200 cps, i.e., $\Delta\omega = 1200$ Hz, while the theoretical values of ω_r'' were in the range $200 < \omega_r'' < 800$ Hz. Hence the finite bandwidth would account for a 20% lowering of the peak maximum even in the most favorable case.

3. It was pointed out (Dr. J. A. Mann, University of Hawaii, personal communication) after the experiments were completed that the output of the the wave analyzer is the root mean square of the current power spectrum and must be squared to obtain the desired power spectrum. The half-width at half-height for the function $G_i^{1/2}(\omega)$ is greater than that for the function $G_i(\omega)$ by a factor $\sqrt{3}$ if $G_i(\omega)$ is Lorentzian. The actual discrepancy observed was generally greater than this; so it is believed that the large wave analyzer bandwidth was the larger source of error.

BIBLIOGRAPHY

1. Plinius, Historia Naturalis, Lib. II, Cap. 106.

2. B. Franklin, Phil. Trans., 64, 445 (1774).

3. W. Thomson (Lord Kelvin), Phil. Mag., 42, 368 (1871).

4. V. Levish, Acta Physicochim. U.R.S.S., 14, 307 (1941).

5. V. Levich, Acta Physicochim. U.R.S.S., 14, 321 (1941).

6. K. Wieghardt, Phys. Z,, 44, 101 (1943).

7. R. Dorrestein, Koninkl. Ned. Akad. Wetenschap., Proc., B 54, 260 (1951).

8. F. C. Goodrich, Proc. Roy. Soc., Ser. A, 260, 490 (1961).

9. F. C. Goodrich, Proc. Roy. Soc., Ser. A, 260, 503 (1961).

10. J. A. Mann, Ph. D. Thesis, Iowa State University, Ames, Iowa (1962).

11. R. S. Hansen and J. A. Mann, J. Appl. Phys., 35, 152 (1964).

12. M. van den Tempel and R. P. van de Riet, J. Chem. Phys., 42, 2769 (1965).

13. J. A. Mann and R. S. Hansen, J. Colloid Sci., 18, 757 (1963).

14. J. A. Mann and R. S. Hansen, J. Colloid Sci., 18, 805 (1963).

15. J. Lucassen and R. S. Hansen, J. Colloid Interfac. Sci., 22, 32 (1966).

16. R. L. Bendure and R. S. Hansen, J. Phys. Chem., 71, 2889 (1967).

17. J. A. Mann and J. Ahmad, J. Colloid Interfac. Sci., 29, 158 (1969).

18. A. Einstein, Ann. Phys., 33, 1275 (1910).

19. L. Brillouin, Ann. Phys. (Paris), 17, 88 (1922).

20. L. I. Mandel'shtam, Zh. Russ. Fiz. Khim. Obshch., 58, 381 (1926).

21. E. F. Gross, Naturwissenschaften, 18, 718 (1930).

22. M. Leontovich, Z. Phys., 72, 247 (1931).

23. J. B. Lastovka, Ph. D. Thesis, Massachusetts Institute of Technology, Cambridge, Massachusetts (1967).

24. A. T. Forrester, J. Opt. Soc. Amer., 51, 253 (1961).

25. E. M. Brody and H. Z. Cummins, Phys. Rev. Lett., 21, 1263 (1968).

26. R. D. Mountain, Rev. Mod. Phys., 38, 205 (1966).

27. S. B. Dubin, J. H. Lunacek, and G. B. Benedek, Proc. Nat. Acad. Sci., U. S., 57, 1164 (1967).

28. Y. Yeh and H. Z. Cummins, Appl. Phys. Lett., 4, 176 (1964).

29. R. H. Katyl and U. Ingard, Phys. Rev. Lett., 19, 64 (1967).

30. R. H. Katyl and U. Ingard, Phys. Rev. Lett., 20, 248 (1968).

31. J. Meunier, D. Cruchon, and M. A. Bouchiat, C. R. Acad. Sci., Paris, Series B, 268, 92 (1969).

32. M. A. Bouchiat and J. Meunier, C. R. Acad. Sci., Paris, Series B, 266, 301 (1968).

33. M. A. Bouchiat and J. Meunier, Phys. Rev. Lett., 23, 752 (1969).

34. R. S. Hansen and J. Ahmad, in "Recent Progress in Surface Science" (in press).

35. J. A. Mann, in "Techniques of Surface Chemistry and Physics", R. J. Good, et al., Eds., New York, N. Y., Dekker, in press.

36. E. H. Lucassen-Reynders and J. Lucassen, Advances in Colloid and Interface Science, 2, 347 (1969).

37. V. G. Levich, "Physicochemical Hydrodynamics, " (English Translation by Scripta Technica, Inc.), Englewood Cliffs, N. J., Prentice Hall, Inc., 1962.

38. R. S. Hansen, J. Lucassen, R. L. Bendure, and G. P. Bierwagen, J. Colloid Interfac. Sci., $\underline{26}$, 198 (1968).

39. J. Lucassen and R. S. Hansen, J. Colloid Interfac. Sci., $\underline{23}$, 319 (1967).

40. R. S. Hansen, J. Appl. Phys., $\underline{35}$, 1983 (1964).

41. J. A. Mann and G. U. Du, J. Colloid Interfac. Sci., in press.

42. R. D. Mountain, Critical Reviews in Solid State Science, $\underline{1969}$, 5 (1969).

43. G. B. Benedek, in "Statistical Physics, Phase Transitions, and Superfluidity", Vol. 2, M. Chretien, E. P. Gross, and S. Deser, Editors, New York, N. Y., Gordon and Breach, 1968, p 1.

44. D. Sette, in "Physics of Simple Liquids", H. N. V. Temperley, J. S. Rowlinson, and G. S. Rushbrooke, Editors, New York, N. Y., Wiley Interscience, 1968, p 325.

45. D. McIntyre and J. V. Sengers, in "Physics of Simple Liquids", H. N. V. Temperley, J. S. Rowlinson, and G. S. Rushbrooke, Editors, New York, N. Y., Wiley Interscience, 1968, Chap. 11.

46. H. Z. Cummins, in "Proceedings of the International School of Physics 'Enrico Fermi' Course XLII - Quantum Optics", R. J. Glauber, Editor, New York, N. Y., Academic Press, 1969, p 247.

47. A. Andronow and M. Leontowicz, A. Phys., $\underline{38}$, 485 (1926).

48. W. L. Peticolas, "Multiphoton Sectroscopy", in Annual Review of Physical Chemistry, H. Eyring, Editor, Palo Alto, Cal., Annual Reviews, Inc., 1967, Vol. 18, p 233.

49. M. J. Rudd, J. Sci. Instr., $\underline{2}$, 55 (1969).

50. G. B. Benedek, "Optical Mixing Spectroscopy with Applications to Problems in Physics, Chemistry, Biology, and Engineering", in the Kastler Jubilee volume: "Polarization, Matter, and Radiation", France, Presses Universitaires de France, 1969.

51. H. J. M. Hanley, "Transport Phenomena in Fluids", New York, N. Y., Dekker, 1966.

52. B. Chu, in "Annual Review of Physical Chemistry", H. Eyring, Editor, Palo Alto, Cal., Annual Reviews, Inc., 1970, Vol. 21, p 145.

53. R. V. Edwards, J. C. Angus, M. J. French, and J. W. Dunning, Jr., J. Appl. Phys., 42, 837 (1971).

54. F. T. Arecchi, in "Proceedings of the International School of Phy Physics 'Enrico Fermi' Course XLII - Quantum Optics", R. J. Glauber, Editor, New York, N. Y., Academic Press, 1969, p 57.

55. L. Seigel and L. R. Wilcox, Bull. Amer. Phys. Soc., 12, 525 (1967 (1967).

56. G. L. Gaines, Jr., "Insoluble Monolayers at Liquid-Gas Interfaces", New York, Interscience Publishers, 1966, p 171.

57. W. D. Harkins, "The Physical Chemistry of Surface Films", New York, Reinhold Publ. Corp., 1952, p 140.

58. I. Langmuir, J. Chem. Phys., 1, 756 (1933).

59. L. Fourt and W. D. Harkins, J. Phys. Chem., 42, 897 (1938).

60. J. A. Mann, J. F. Baret, F. J. Dechow, and R. S. Hansen, J. Colloid Interfac. Sci., in press.

61. S. Ikeda and T. Isemura, Bull. Chem. Soc. Japan, 34, 416 (1961).

62. Y. Yeh and R. N. Keeler, Quart. Rev. Biophys., 2, 315 (1969).

63. S. Fujime, J. Phys. Soc. Japan, 28, 267 (1970).

ACKNOWLEDGEMENT